

Field Line Resonance in Two and a Half Dimensions

DRAFT VERSION CREATED ON APRIL 3, 2016

© Charles A. McEachern 2016



The text of this work is licensed under a Creative Commons
Attribution-ShareAlike 4.0 International license.

Acknowledgements

Acknowledgement placeholder.

Dedication

Dedication placeholder.

Abstract

Abstract placeholder.

Contents

Acknowledgements	i
Dedication	ii
Abstract	iii
List of Tables	vii
List of Figures	viii
1 Introduction	1
1.1 Structure of the Present Work	2
2 The Near-Earth Environment	4
2.1 The Outer Magnetosphere	4
2.2 The Inner Magnetosphere	6
2.3 The Ionosphere	8
2.4 Geomagnetic Storms and Substorms	9
3 Field Line Resonance	11
3.1 Harmonic Structure	14
3.2 Azimuthal Modenumber	16
3.3 Poloidal and Toroidal Polarizations	18
3.4 Giant Pulsations	21
3.5 Motivations for the Present Work	22

4 Waves in Cold Resistive Plasma	24
4.1 Guided Propagation	26
4.2 Compressional Propagation	27
4.3 High Altitude Limit	29
4.4 Implications to the Present Work	30
5 “Tuna Half” Dimensional Model	32
5.1 Coordinate System	33
5.2 Physical Parameter Profiles	37
5.3 Driving	41
5.4 Maxwell’s Equations	43
5.5 Boundary Conditions	47
6 Electron Inertial Effects	52
6.1 The Boris Factor	53
6.2 Parallel Currents and Electric Fields	55
6.3 Inertial Length Scales	61
6.4 Discussion	62
7 Numerical Results	64
7.1 Finite Poloidal Lifetimes: Dayside	65
7.2 Spatial Distribution of Energy: Dayside	70
7.3 Finite Poloidal Lifetimes: Nightside	75
7.4 Spatial Distribution of Energy: Nightside	79
7.5 Ground Signatures and Giant Pulsations	82
7.6 Discussion	86
8 Observations	88
8.1 Sampling Bias and Event Selection	89
8.2 Overall Rate of Pc4 Events	95
8.3 Pc4 Events by Mode	99
8.4 Pc4 Events Inside and Outside the Plasmapause	103
8.5 Poloidal Pc4 Events by Compressional Coupling	104

8.6	Pc4 Events by Spectral Width	108
8.7	Double-Triggering Events	114
8.8	Discussion	115
9	Conclusion	116
9.1	Summary of Results	116
9.2	Future Work	116
	References	118

List of Tables

3.1	IAGA Magnetic Pulsation Frequency Bands	12
5.1	Typical Parameters for the Tuna Density Profile	38
5.2	Integrated Atmospheric Conductivity	48

List of Figures

2.1	Outer Magnetosphere Cutaway	5
2.2	Inner Magnetosphere Cutaway	7
3.1	Alfvén Bounce Frequencies	13
3.2	First and Second Harmonic Resonances	15
3.3	Large and Small Azimuthal Modenumbers	17
3.4	Poloidal Mode Structure	19
3.5	Toroidal Mode Structure	20
4.1	Compressional Alfvén Wave Cutoff Frequencies	31
5.1	Nonorthogonal Dipole Grid	37
5.2	Alfvén Speed Profiles	39
5.3	Ionospheric Conductivity Profiles	40
5.4	Decreasing Penetration with Increasing Modenumber	42
5.5	Sym-H for June 2013 Storm	43
6.1	Plasma Frequency Profile	54
6.2	Electric Field Snapshots	56
6.3	Current and Poynting Flux at 100 km	57
6.4	Current and Poynting Flux at 1000 km	59
6.5	Power Density at the Ionosphere	60
6.6	Parallel Electric Fields by Perpendicular Grid Resolution	62
7.1	Poloidal and Toroidal Energy: Quiet Day, Typical Plasmasphere	68
7.2	Poloidal and Toroidal Energy: Quiet Day, Large Plasmasphere	69
7.3	Radial Distribution of Poloidal Energy: Quiet Day, Typical Plasmasphere	72
7.4	Radial Distribution of Poloidal Energy: Quiet Day, Large Plasmasphere	73

7.5	Radial Distribution of Toroidal Energy: Quiet Day	74
7.6	Poloidal and Toroidal Energy: Active Night, Driving at $L = 5$	77
7.7	Poloidal and Toroidal Energy: Active Night, Driving at $L = 6$	78
7.8	Radial Distribution of Poloidal Energy: Active Night, Driving at $L = 6$	80
7.9	Radial Distribution of Toroidal Energy: Active Night	81
7.10	Dayside Ground Magnetic Fields	84
7.11	Nightside Ground Magnetic Fields	85
8.1	Distribution of Usable Van Allen Probe Data: Fine Resolution	91
8.2	Distribution of Usable Van Allen Probe Data	92
8.3	Distribution of Usable Van Allen Probe Data: $Dst \geq -30 \text{ nT}$	93
8.4	Distribution of Usable Van Allen Probe Data: $Dst < -30 \text{ nT}$	94
8.5	Pc4 Rate	96
8.6	Pc4 Rate: $Dst \geq -30 \text{ nT}$	97
8.7	Pc4 Rate: $Dst < -30 \text{ nT}$	98
8.8	Pc4 Rate by Mode	100
8.9	Pc4 Rate by Mode: $Dst \geq -30 \text{ nT}$	101
8.10	Pc4 Rate by Mode: $Dst < -30 \text{ nT}$	102
8.11	Pc4 Rate Inside and Outside the Plasmapause	103
8.12	Pc4 Rate Inside and Outside the Plasmapause by Mode	104
8.13	Poloidal Pc4 Rate by Compressional Coupling	105
8.14	Poloidal Pc4 Rate by Compressional Coupling: $Dst \geq -30 \text{ nT}$	106
8.15	Poloidal Pc4 Rate by Compressional Coupling: $Dst < -30 \text{ nT}$	107
8.16	Poloidal Pc4 Rate by Spectral Width	108
8.17	Poloidal Pc4 Rate by Spectral Width: $Dst \geq -30 \text{ nT}$	109
8.18	Poloidal Pc4 Rate by Spectral Width: $Dst < -30 \text{ nT}$	110
8.19	Toroidal Pc4 Rate by Spectral Width	111
8.20	Toroidal Pc4 Rate by Spectral Width: $Dst \geq -30 \text{ nT}$	112
8.21	Toroidal Pc4 Rate by Spectral Width: $Dst < -30 \text{ nT}$	113
8.22	Dual Poloidal + Toroidal Pc4 Events	115

Chapter 1

Introduction

TODO: In 1859, humanity was working hard to get its shit together. The United States moved steadily toward the American Civil War, which would abolish slavery and consolidate the power of the federal government. A slew of conflicts in Southern Europe, such as the Austro-Sardinian War, set the stage for the unification of Italy. The Taiping Civil War — one of the bloodiest conflicts of all time — is considered by many to mark the beginning of modern Chinese history. Origin of Species was published. The first transatlantic telegraph cable was laid.

Meanwhile, ambivalent to humanity, the Sun belched an intense burst of charged particles and magnetic energy directly at Earth. The resulting geomagnetic storm¹ caused telegraph systems to fail across the Western hemisphere, electrocuting operators and starting fires[36, 98]. Displays of the northern lights were visible as far south as Cuba.

The Solar Storm of 1859 was perhaps the most powerful in recorded history, but by no means was it a one-time event. The Sun discharges hundreds of coronal mass ejections (CMEs) per year, of all sizes, in all directions. In fact, a comparably large CME narrowly missed Earth in 2012[74]. Had it not, it's estimated it would have caused widespread, long-term electrical outages, with a damage toll on the order of 10^{12} dollars[68].

¹The Solar Storm of 1859 is also called the Carrington Event, after English astronomer Richard Carrington. He drew a connection between the storm's geomagnetic activity and the sunspots he had observed the day before.

The Sun’s extreme — and temperamental — effect on Earth’s magnetic environment makes a compelling case for the ongoing study of space weather. Such research has evolved over the past century from sunspot counts and compass readings to multi-satellite missions and supercomputer simulations. Modern methods have dramatically increased humanity’s understanding of the relationship between the Sun and the Earth; however, significant uncertainty continues to surround geomagnetic storms, substorms, and the various energy transport mechanisms that make them up.

The present work focuses in particular on the phenomenon of field line resonance: Alfvén waves bouncing between the northern and southern hemispheres. Such waves play an important part in the energization of magnetospheric particles, the transport of energy from high to low altitude, and the driving of currents at the top of the atmosphere.

1.1 Structure of the Present Work

Chapter 2 surveys the near-Earth environment. Prominent features of the magnetosphere are defined. The response of the magnetosphere to transient solar wind events is summarized.

Chapter 3 introduces the field line resonance phenomenon, in terms of both the underlying physics and notable work on the topic. Jargon is introduced to clarify important elements of wave structure. Several open questions about field line resonances (FLRs) are offered as motivations for the present work.

Chapter 4 lays the groundwork for a numerical model by exploring the fundamental equations of waves in a cold, resistive plasma — such as Earth’s magnetosphere. Characteristic scales are gleaned from the resulting dispersion relations.

Chapter 5 presents Tuna, a new two and a half dimensional simulation designed specifically for the realistic modeling of FLRs. Tuna’s non-orthogonal geometry, height-resolved ionosphere, novel driving mechanism, and coupling to the atmosphere are explained.

Chapter 6 considers the addition of electron inertial effects to Tuna, touches on what can be learned from them, and shows that they incur an unreasonable computational cost. (Electron inertia is neglected in the results presented in other chapters.)

Chapter 7 describes the core numerical results of the work, unifying several of the questions posed in Chapter 3. Significant depth is added to past work on finite poloidal lifetimes[66, 80]. Interplay between poloidal-toroidal coupling, shear-compressional coupling, and Joule dissipation is considered from several angles.

Chapter 8 puts the numerical results in physical context through the analysis of data from the Van Allen Probes mission. FLR occurrence rates are considered in terms of not only location, but mode structure and polarization as well — parameters which are not considered in other recent FLR surveys[17, 72].

Chapter 9 briefly summarizes the results shown in the above chapters — the code development, analysis of numerical results, and satellite observation — and suggests further directions.

Chapter 2

The Near-Earth Environment

From Earth’s surface to a height of a hundred kilometers or so, the atmosphere is a well-behaved fluid: a collisional ensemble of neutral atoms. Higher up, its behavior changes dramatically. As altitude increases, solar ultraviolet radiation becomes more intense, which ionizes atmospheric atoms. Density also decreases, slowing collisional recombination. Whereas the neutral atmosphere is held against Earth’s surface by gravity, the motion of charged particles is dominated by Earth’s geomagnetic field, as well as the electromagnetic disturbances created as that field is hammered by the solar wind.

The present section outlines the structure of the magnetosphere; that is, the region of space governed primarily by Earth’s magnetic field. Particular emphasis is placed on structures which relate closely to field line resonance.

2.1 The Outer Magnetosphere

Plasma behavior within Earth’s magnetosphere is ultimately driven by the solar wind: a hot (~ 100 eV), fast-moving (~ 100 km/s) plasma threaded by the interplanetary magnetic field (~ 1 nT)¹. The density of the solar wind is on the order of 10^6 /cm³; in a laboratory

¹Listed values correspond to the solar wind at Earth’s orbit.

setting, this would constitute an ultra-high vacuum (atmospheric density at sea level is $\sim 10^{19} \text{ /cm}^3$), but compared to much of the magnetopause it's quite dense.



Figure 2.1: TODO: The outer magnetosphere...

The magnetosphere's outer boundary represents a balance between the solar wind dynamic pressure and the magnetic pressure of Earth's dipole field. On the dayside, the dipole is compressed, pushing this boundary to within about $10 R_E$ of Earth². The nightside magnetosphere is stretched into a long tail which may exceed $50 R_E$ in width and $100 R_E$ in length.

When the interplanetary magnetic field opposes the geomagnetic field at the nose of the magnetosphere, magnetic reconnection occurs. Closed magnetospheric field lines “break,” opening up to the interplanetary magnetic field³. They then move tailward

²Distances in the magnetosphere are typically measured in units of Earth radii: $1 R_E \equiv 6378 \text{ km}$.

³Closed field lines connect at both ends to the magnetic dynamo at Earth's core. Open field lines meet Earth at only one end; the other connects to the interplanetary magnetic field. The distinction is important because charged particle motion is guided by magnetic field lines, as discussed in Chapter 3.

across the poles, dragging their frozen-in plasma with them⁴. Reconnection in the tail allows magnetic field lines to convect back to the day side, across the flanks. This process is called the Dungey cycle[23].

Viewed from the north, the Dungey cycle involves a clockwise flow of flux and plasma on the dusk side and a counterclockwise flow on the dawn side. The motion is accompanied by a convection electric field, per Ohm's law⁵.

TODO: Jets from magnetic reconnection... release of magnetic tension!

Consistent with Ampère's law, the interplanetary magnetic field is separated from the magnetosphere by a current sheet: the magnetopause. On the dayside, the magnetopause current flows duskward; on the nightside, it flows downward around the magnetotail.

Plasma within the tail is cool ($\sim 100 \text{ eV}$) and rarefied ($\sim 10^{-2} / \text{cm}^3$). Earth's dipole is significantly deformed in the magnetotail; field lines in the northern lobe of the tail points more or less Earthward, and vice versa. The two lobes are divided by the plasma sheet, which is comparably hot ($\sim 10^3 \text{ eV}$) and dense ($\sim 1 / \text{cm}^3$). The plasma sheet carries a duskward current which connects to the magnetopause current.

2.2 The Inner Magnetosphere

Within about **TODO: $L \sim 10$** (where L is the McIlwain parameter⁶), the dipole magnetic field is not appreciably deformed by the solar wind. As a result, the structures in the inner magnetosphere follow closely from the motion of charged particles in an ideal dipole field.

⁴In the outer magnetosphere (as well as most of the inner magnetosphere), collisions are so infrequent that magnetic flux is said to be “frozen in” to the plasma. Charged particles move freely along magnetic field lines, but cannot cross from one line to another. Compression of the magnetic field is synonymous with compression of the ambient plasma.

⁵In the case of an ideal plasma, Ohm's law takes the form $\underline{E} + \underline{U} \times \underline{B} = 0$.

⁶The McIlwain parameter L is used to index field lines in Earth's dipole geometry: $L \equiv \frac{r}{\sin^2 \theta}$ for colatitude θ and radius r in Earth radii. For example, the $L = 5$ field line passes through the equatorial plane at a geocentric radius of $5 R_E$, then meets the Earth at a colatitude of $\arcsin \sqrt{\frac{1}{5}} \sim 27^\circ$ (equally, a latitude of $\arccos \sqrt{\frac{1}{5}} \sim 63^\circ$).

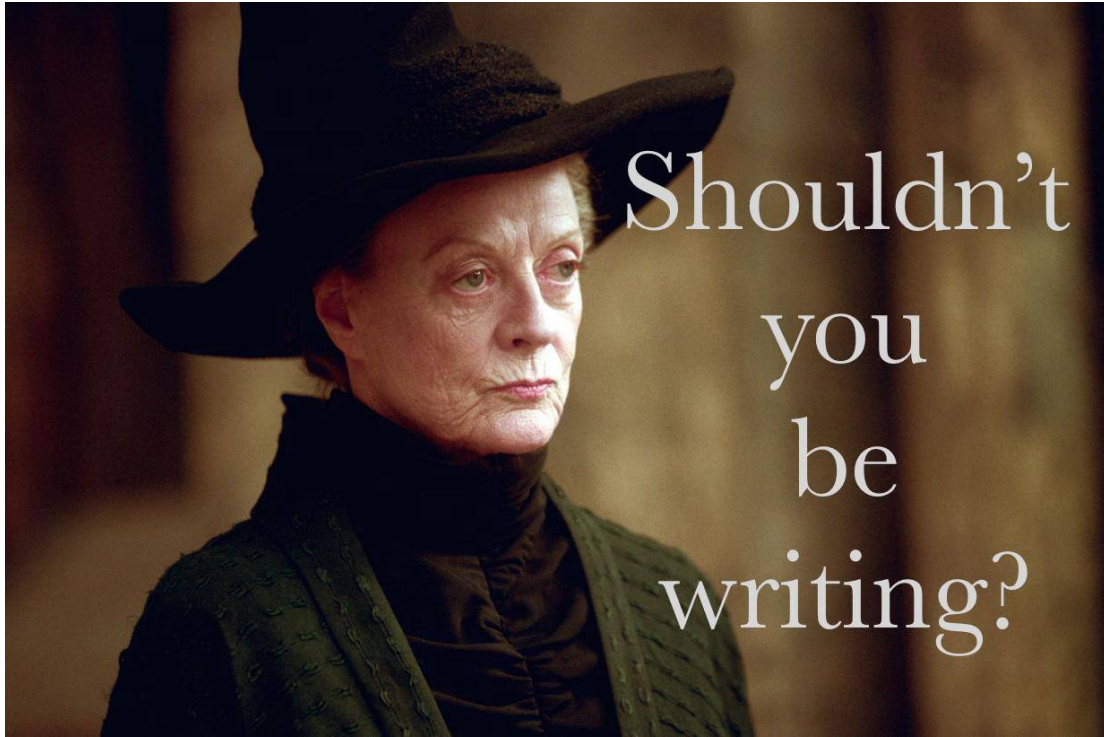


Figure 2.2: TODO: The inner magnetosphere...

The plasmasphere — a cold (~ 1 eV), dense ($10^2 / \text{cm}^3$ to $10^4 / \text{cm}^3$) torus of corotating plasma — is formed by the outward drift of atmospheric ions along magnetic closed field lines. Its outer boundary, is thought to represent a balance between the corotation electric field (per the rotation of Earth's magnetic dipole) and the convection electric field (associated with the convection of magnetic flux during the Dungey cycle). Particle density drops sharply at the edge of the plasmasphere; the boundary is called the plasmapause. The plasmapause typically falls around $L = 4$, though during prolonged quiet times it can extend to $L = 6$ or larger.

Energetic particles trapped within the inner magnetosphere are divided into two populations.

The Van Allen radiation belts are made up of particles with energy above 10^5 eV or so. The inner belt ($L \lesssim 2$) is primarily composed of protons, the decay remnants of

neutrons freed from the atmosphere by cosmic rays. The outer belt ($L \gtrsim 4$) is primarily composed of high-energy electrons.

Particles with energies of 10^3 eV to 10^5 eV make up the ring current, which extends from $L \sim 3$ to $L \sim 5$. Gradient-curvature drift carries ions and electrons in opposite directions; the net result is a westward current. During quiet times, the ring current causes magnetic a southward magnetic field on the order of 1 nT at Earth's equator⁷.

2.3 The Ionosphere

Earth's neutral atmosphere is an excellent insulator. Collisions are so frequent that charged particles quickly thermalize and recombine. The breakdown of air molecules into a conductive plasma (as happens during a lightning strike, for example) requires electric fields on the order of 10^9 mV/m.

Currents are also suppressed by the magnetosphere. In the absence of collisions, electrons and ions drift alongside one another in response to an electric field, creating no net current perpendicular to the magnetic field⁸. Magnetic field lines are (to a good approximation) equipotential contours; electric fields do not form along them to drive parallel currents.

The ionosphere is a sweet spot between the two regimes. Collisions are frequent enough to disrupt the drift of ions, but not frequent enough to immobilize the electrons. The result is nonzero Pedersen and Hall conductivity, corresponding to current along the electric field and in the $\underline{B} \times \underline{E}$ direction respectively. Collisions in the ionosphere also give rise to a finite parallel conductivity, allowing for the formation of potential structures along the magnetic field line.

TODO: Field-aligned currents depend on the level of geomagnetic activity... but do they ever completely go away?

⁷For comparison, Earth's dipole field points north at the equator with a magnitude over 10^4 nT.

⁸The so-called E -cross- B drift is associated with a velocity of $\underline{U} = \frac{1}{B^2} \underline{E} \times \underline{B}$, independent of a charged particle's mass or sign.

The convection electric field (associated with the Dungey cycle, Section 2.1) drives Pedersen currents in the ionosphere. It is these currents that give rise to the strongest magnetic fields on the ground. Pedersen currents flow downward on the flanks and duskward across the poles. The currents remain divergence-free by connecting to field-aligned currents at the edges of the polar cap. The field-aligned currents, in turn, connect to the magnetopause current, the cross-tail current, and the (partial) ring current.

When electron density is low, thermal velocities may be unable to carry enough current to satisfy $\nabla \cdot \underline{J} = 0$. This leads to the formation of potential structures along geomagnetic field lines in the ionosphere. Such structures accelerate particles along magnetic field lines, leading to the precipitation of energetic particles into the atmosphere. As the particles thermalize, they excite atmospheric atoms. The resulting spontaneous emission is often in the visible spectrum, giving rise to the aurora.

TODO: Particles can also be excited by Alfvén waves... this probably goes in Chapter 3.

2.4 Geomagnetic Storms and Substorms

The quiet geomagnetic behavior described above is periodically disturbed by transient solar phenomena such as corotating interaction regions (CIRs) and coronal mass ejections (CMEs). CMEs, as noted in Chapter 1, are bursts of unusually dense solar wind which are ejected from regions of high magnetic activity on the Sun; they are most common at the height of the eleven-year solar cycle. CIRs, on the other hand, occur when a relatively fast region of the solar wind catches up to an earlier and slower-moving pocket of solar wind, resulting in a pair of shockwaves.

During a storm, increased solar wind intensity results in enhanced magnetic reconnection on the dayside. As the newly-opened field lines are swept tailward, the convection electric field is strengthened. The plasmasphere — the outer boundary of which is set by a balance between the convection electric field and the (more or less constant) corotation electric field — sheds its outer layers. A large number of energetic particles are also injected into the ring current[70].

The strength of the storm is gauged by the size of the magnetic perturbation created by the ring current⁹. A small storm has a magnitude of 50 nT to 100 nT. Large storms may reach 250 nT to 500 nT. The Carrington Event, mentioned in Chapter 1, is thought to have exceeded 1700 nT[98].

The main phase of a storm typically lasts for several hours. Storm recovery — the gradual return of the storm index to zero — typically lasts several days. The plasmapause refilling occurs on timescales of **TODO: ???**. Geomagnetic storms occur tens of times per year at the height of the solar cycle, and just a few times per year otherwise.

Whereas storms are prompted by large solar wind events on the dayside, geomagnetic substorms are primarily a nightside occurrence. As flux accumulates in the tail, magnetic tension builds in the stretched field lines. A substorm is an impulsive release of that tension.

TODO: Phases of a substorm. Definition of a substorm comes from [1]. Revised by [71].

At substorm onset, a burst of reconnection occurs in the tail. A jet of plasma is launched Earthward from the reconnection site (and another is launched tailward, and lost to the solar wind). The Earthward plasma injection injects particles into the ring current. The outer radiation belt is depleted, then repopulated. Energetic particles precipitate into the atmosphere, giving rise to a distinctive **TODO: hour-long** sequence of auroral signatures.

Concurrent with substorm onset, impulsive Alfvén waves are observed with periods of a minute or two. The precise ordering of events — whether reconnection causes the waves, or vice versa, or if they share a common cause — remains controversial.

Each substorm lasts several hours, including the time it takes for the ring current to return to pre-substorm levels. Several substorms may occur per day during quiet times. During a storm, substorms become far more frequent; by the time one has ended, another may have already begun.

⁹The most commonly used storm index is Dst, which is computed hourly using measurements from several ground magnetometers near the equator. The Sym-H index, used in Section 5.3, is computed once per minute.

Chapter 3

Field Line Resonance

The motion of a charged particle in a dipole field can be described in terms of three fundamental motions. The first is cyclotron motion: a particle orbits around a magnetic field line in accordance with the Lorentz force. The second is bounce motion: while orbiting, the particle moves along the field line like a bead on a wire, back and forth between the northern and southern hemispheres¹. The third is drift motion: as particles orbit and bounce, they also move azimuthally around Earth per the gradient-curvature drift.

Characteristic timescales for each of the above motions depend on particle energy. Electron cyclotron motion is on the order of `TODO: ...` in the ionosphere, and closer to `TODO: ...` in the tail; ions gyrate slower by three orders of magnitude due to their larger mass. `TODO: Bounce... Drift...`

Wave-particle resonance arises when a particle's periodic motion matches with the frequency of a coincident electromagnetic wave[25, 65, 76, 87]. In the particle's rest frame, the wave then appears as a net electric field. This allows a net movement of energy

¹As a particle approaches Earth, it experiences an ever-stronger magnetic field. The particle's perpendicular kinetic energy increases in proportion with the magnetic field in order to conserve its first adiabatic invariant. When the perpendicular kinetic energy can no longer increase — that is, when the parallel kinetic energy is zero — the particle bounces back. (If the parallel kinetic energy is sufficiently large, the particle doesn't bounce; it precipitates into the atmosphere.)

between the wave and the particle. The interaction is analogous to a surfer moving along with — and being accelerated by — a wave in the ocean.

In the present work, the waves in question are field line resonances (FLRs). An FLR is a standing harmonic on a geomagnetic field line. It can also be envisioned as a superposition of traveling waves, reflecting back and forth between its northern and southern foot points at the conducting ionosphere. These waves travel at the Alfvén speed². The fundamental equations of field line resonance were presented by Dungey in 1954[22]; since then, they have remained a topic of active study.

So-called ultra low frequency waves — of which FLRs are a subset — are categorized by morphology. Continuous (long-lived) pulsations are termed Pc, while irregular pulsations are called Pi. Within each are a number of frequency bands; see Table 3.1[46].

Table 3.1: IAGA Magnetic Pulsation Frequency Bands

	Pc1	Pc2	Pc3	Pc4	Pc5	Pi1	Pi2
Period (s)	0.2–5	5–10	10–45	45–150	150–600	1–40	40–150
Frequency (mHz)	200–5000	100–200	22–100	7–22	2–7	25–1000	7–25

FLRs fall into the Pc3, Pc4, and Pc5 ranges. The present work focuses specifically on the Pc4 band: waves with periods of a minute or two. Frequencies in the Pc4 range typically coincide with Alfvén bounce times³ near the plasmapause: $L \sim 4$ to $L \sim 6$ [3, 17, 26, 57]⁴. In fact, the large radial gradients in the Alfvén speed near the plasmapause act as an effective potential well, trapping FLRs[16, 51, 54, 55, 64, 90].

In addition to being radially localized, FLRs in the Pc4 frequency band (also called Pc4 pulsations, or just Pc4s) are localized in magnetic local time (MLT⁵). They have also

²The Alfvén speed is given by v_A is given by $v_A^2 \equiv \frac{B^2}{\mu_0 \rho}$, where B is the magnitude of the magnetic field, μ_0 is the magnetic constant, and ρ is the mass density of the ambient plasma. It can vary by several orders of magnitude over the length of a magnetic field line.

³The Alfvén frequency is the inverse of the Alfvén bounce time: $\frac{2\pi}{\omega_A} \equiv \oint \frac{dz}{v_A}$.

⁴Not coincidentally, these are the same L -shells where the Van Allen Probes spend most of their time; see Chapter 8.

⁵Noon points toward the Sun and midnight away from it, with 06:00 and 18:00 at the respective dawn and dusk flanks.

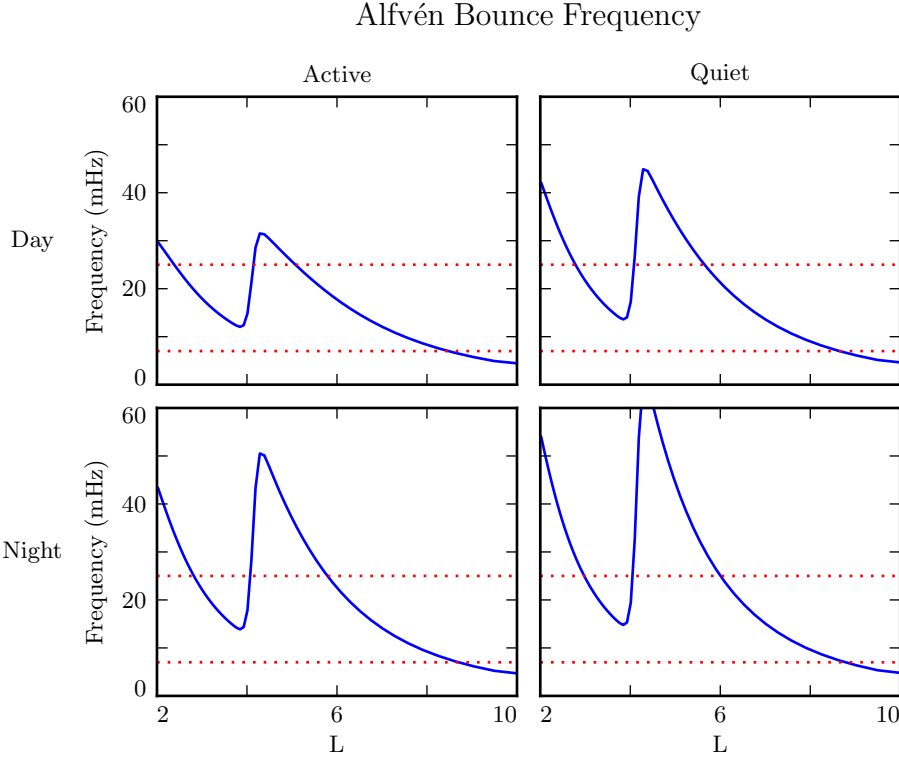


Figure 3.1: The above are bounce frequencies for an Alfvén wave moving back and forth along a geomagnetic field line. Alfvén speeds are computed based on profiles from Kelley[49], as discussed in Section 5.2. Notably, the bounce frequency depends significantly on the position of the plasmasphere, taken here to be at $L = 4$. Dotted lines indicate the Pc4 frequency range: 7 mHz to 25 mHz.

been shown to occur preferentially on the dayside, during storms or storm recovery[3, 17, 26, 53, 57, 99].

In the inner magnetosphere, the Alfvén frequency — and thus the frequency of FLRs — often coincides with integer or half-integer⁶ multiples of particle drift frequencies[18]. The resulting wave-particle interactions can give rise to significant energization and radial diffusion of the particles. In some cases, the waves also include an electric field parallel to the background magnetic field, contributing to the precipitation of energetic particles into the neutral atmosphere[33, 34, 95, 105].

⁶See Section 3.1.

The present chapter introduces the structural characteristics of FLRs, how those characteristics affect wave behavior, and several unresolved questions related to that behavior.

TODO: The polarization of long-period Alfven waves is rotated by $\sim 90^\circ$ when passing through the ionosphere[42]. A wave that is azimuthally polarized in space is polarized north-south on the ground, and vice versa. It has been noted specifically that Pgs exhibit east-west polarized ground signatures[94].

TODO: Other planets[32]? Seems exciting but maybe not relevant.

3.1 Harmonic Structure

Wave structure along a geomagnetic field line is indicated by harmonic number. The first (or fundamental) harmonic has a wavelength twice as long as the field line. It exhibits an antinode in the perpendicular electric field at the equator, along with a node in the perpendicular magnetic field. The second harmonic is a single wavelength along the field line. Its perpendicular magnetic perturbation has an antinode at the equator, while its perpendicular electric field has a node. Figure 3.2 shows a qualitative sketch of each: a series of snapshots in time, in the rest frame of the wave. Perpendicular electric and magnetic field perturbations are shown in blue and red respectively.

A first-harmonic FLR that is periodic or localized in the azimuthal direction is conducive to drift-resonant wave-particle interactions[18, 77]. The particle is like a child on a swing: whenever the path of the particle (or child) gets close to the wave (parent), it gets a push, and always in the same direction. The wave fields spend half its time pointing the other direction, just as the parent must shift their weight backward to get ready for the next push, but at that point the particle (child) is far away.

Second-harmonic FLRs interact with particles through the drift-bounce resonance, which is slightly more complicated. As the particle drifts azimuthally, it also zig-zags north-south. The combination of those two periodic motions must align with the phase of the wave electric field. An example path is shown by the purple line in Figure 3.2: the particle experiences a rightward electric field throughout the wave’s oscillation.

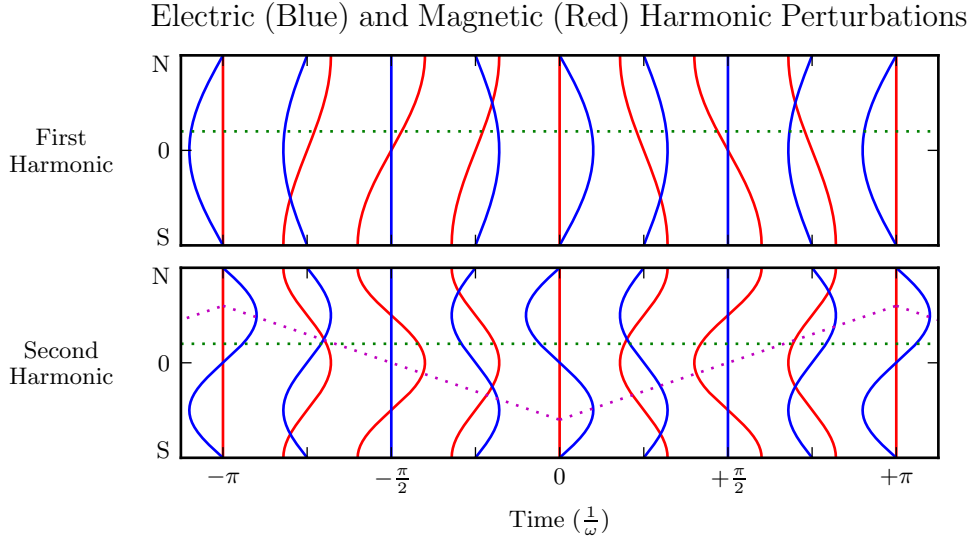


Figure 3.2: The first (or fundamental) harmonic has an antinode in its perpendicular electric field (blue) at the equator, along with a node in its perpendicular magnetic field perturbation (red). A single satellite can identify the first harmonic by the relative phase of the electric and magnetic field perturbations: an observer north of the equator (green) will see the magnetic field perturbation lead the electric field by 90° . The second harmonic is the opposite: it has an electric field node at the equator, and an observer north of the equator will see the magnetic field perturbation lag the electric field by 90° . The purple line sketches the path of a particle in drift-bounce resonance; in the particle's rest frame, the electric field is always to the right. **TODO:** Actually, toroidal waves are flipped — Faraday's law gives $\frac{\partial}{\partial t} B_x \sim \frac{\partial}{\partial z} E_y$ but $\frac{\partial}{\partial t} B_y \sim -\frac{\partial}{\partial z} E_x$.

The drift and drift-bounce resonance conditions are written, respectively[91]:

$$\omega - m\omega_D = 0 \quad \text{and} \quad \omega - m\omega_D = \omega_B \quad (3.1)$$

Where ω is the frequency of the wave, ω_D and ω_B are the particle's drift and bounce frequencies respectively, and m is the wave's azimuthal modenumber, as discussed in Section 3.2.

In principle, the first and second harmonics can be distinguished by their frequencies, even from a single-point observation[15, 35]. In practice, however, this is not a reliable

approach[92]. There are significant uncertainties surrounding the number density profile — and thus the Alfvén speed profile — along a geomagnetic field line.

Harmonic structure can also be deduced by noting the phase offset between the wave magnetic field and its electric field (or the plasma velocity)[17, 94]. In Figure 3.2, the green line indicates an observer just north of the magnetic equator. For the first harmonic, the observer sees the electric field waveform lead the magnetic field by a phase of 90° ; for the second harmonic, the electric field waveform lags by 90° . (South of the equator, the signs are reversed.) Notably, this approach has only become viable with the advent of satellites carrying both electric and magnetic field instrumentation, such as THEMIS in 2007[4] and the Van Allen Probes⁷ in 2012[88].

Strictly speaking, the the phase offset of the electric and magnetic fields does not provide the harmonic number — only its parity. It's reasonably safe to assume that an even mode is the second harmonic; the second harmonic is by far the most commonly observed[45, 85, 93], due in part to its excitement by the antisymmetric balloon instability[9, 11, 13, 87]. However, the distinction between the first and third harmonics is not always clear; this issue is discussed further in Chapter 8. Higher harmonics than that are not expected in the Pc4 frequency band.

TODO: Second-harmonic FLRs are unlikely to cause ground signatures[94].

TODO: Dai found a nice event[18] that was unambiguously determined to be a fundamental-mode Pc4 in drift-resonant interaction with $\sim 10^5$ eV ions. Consistent with [96]. Other observations of odd harmonics: [106, 27].

3.2 Azimuthal Modenumber

The wavelength of an FLR in the azimuthal direction is indicated by its azimuthal wavelength. A wave with modenumber m has an azimuthal wavelength that spans $\frac{24}{m}$ hours in MLT.

⁷The Van Allen Probes were previously called RBSP, for Radiation Belt Storm Probes.

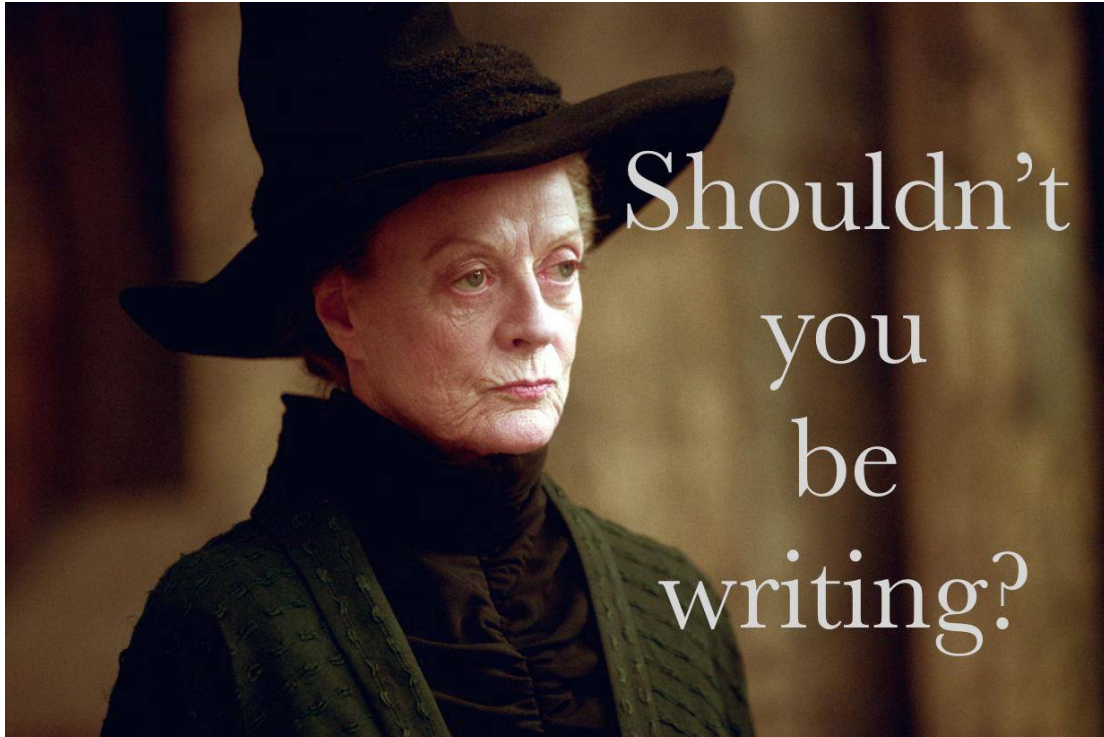


Figure 3.3: TODO: Large and small azimuthal modenumbers.

Waves with small azimuthal modenumbers ($0 < m < 10$) are typically driven by broadband energy sources at the magnetosphere's boundary, such as variations in the solar wind pressure[19, 39, 50, 109, 110], sporadic magnetic reconnection[43], or Kelvin-Helmholtz waves on the magnetopause[10, 59, 86]. In the low- m regime, the shear and compressional Alfvén waves are coupled, which allows energy to move across field lines until the driving frequency lines up with the local Alfvén frequency[61]. Because of their broadband energy source, low- m FLRs often have a mishmash of frequencies present in their spectra[17].

When the azimuthal modenumber is large (or, equally, when the azimuthal wavelength is small), the shear and compressional Alfvén waves are decoupled[15, 80]⁸. As a result, FLRs must be driven from within the magnetosphere. Proposed energy sources include

⁸Equally, the strength of a wave's parallel component hint at its modenumber, a point which is revisited in Chapter 8.

phase space gradients near the plasmapause[18], particularly as the plasmasphere refills after a storm or substorm[26, 56].

The ionosphere is known to attenuate waves with small spatial extent in the perpendicular direction[44, 104, 108]. As a result, FLRs may create no signature on the ground if their azimuthal modenumber is large. For example, a recent paper by Takahashi shows a strong (2 nT at $L \sim 10$), clear resonance with $|m| \gtrsim 70$ and no corresponding ground signature[92].

Southwood[87] and Glassmeier[30] show that a low frequency wave passing through the ionosphere on its way to Earth will be attenuated per

$$\frac{B_E}{B_I} = \frac{\Sigma_H}{\Sigma_P} \exp\left(-m \frac{R_I - R_E}{R_E \sin \theta}\right) \quad (3.2)$$

Where B_E and B_I are the magnetic field strengths at R_E (Earth's surface, 6783 km geocentric) and R_I (the ionosphere, \sim 6900 km geocentric) respectively. The integrated ionospheric Pedersen and Hall conductivities, Σ_P and Σ_H , are typically within a factor of two of one another. Field lines near the plasmapause can be traced to Earth at $\sin \theta \sim 0.4$. That is, by the time it reaches the ground, the magnetic field from an FLR with $m = 10$ is weaker by a factor of two; at $m = 100$, the factor is closer to 100.

3.3 Poloidal and Toroidal Polarizations

Based on polarization, each FLR can be classified as either poloidal or toroidal. The poloidal mode is a field line displacement in the meridional plane, as shown in Figure 3.4, with an accompanying electric field in the azimuthal direction. The toroidal mode's magnetic displacement is azimuthal, per Figure 3.5; the associated electric field is in the meridional plane.

Both poloidal and toroidal waves are noted for their ability to contribute to the energization and radial diffusion of trapped particles. The poloidal mode interacts more strongly,

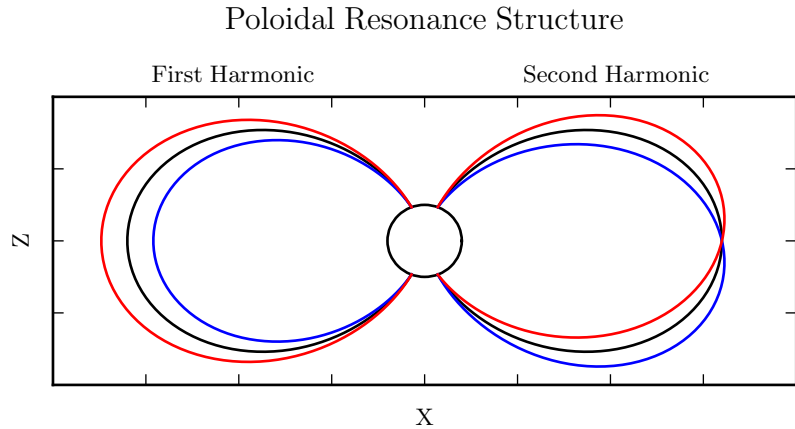


Figure 3.4: The poloidal resonance is a magnetic field in the meridional plane. The displacement is radial near the equator, and can be accompanied by enhancement in the parallel magnetic field near the ionosphere. The first harmonic is shown on the left, and the second harmonic on the right. Lines are colored red and blue only to contrast with the unperturbed black field line.

since its electric field is aligned with the trapped particles’ drift motion. Poloidally-polarized waves are also more prone to creating magnetic signatures on the ground, due to ducting in the ionosphere[28, 37].

Toroidal modes have been shown to far outnumber poloidal modes[3]. Perhaps not coincidentally, poloidally-polarized waves rotate asymptotically to the toroidal mode[66, 67, 80]. Poloidal waves with low azimuthal modenumber — such as those driven by broadband sources at the magnetopause — rotate on timescales comparable to their oscillation periods.

TODO: Fishbone instability[12, 69]. Like the poloidal mode, but for lab plasmas.

TODO: Poloidal and toroidal modes are coupled by the ionospheric Hall conductivity[48]. The Hall conductivity also increases the “ringtime” of these resonances, allowing them to oscillate through the inductive process rather than be dissipated as Joule heating[102].

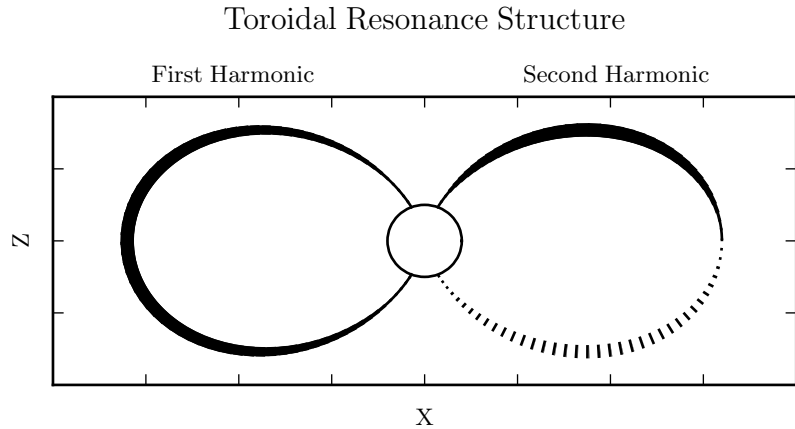


Figure 3.5: A toroidally-polarized FLR has a magnetic perturbation in the azimuthal direction, as shown. Bold lines are taken to be above the page, and dotted lines below the page, with the displacement indicated by the line's width. The first harmonic — where the entire field line oscillates in and out of the page — is shown on the left. The second harmonic is on the right, with northern and southern halves perturbed in opposite directions.

TODO: Toroidal modes show a clear frequency dependence with L . Poloidal modes less so. Citation...?

3.4 Giant Pulsations

The study of geomagnetic pulsations long predates satellites, sounding rockets, or even the word “magnetohydrodynamics”⁹. Large, regular oscillations in the magnetic field were noted as early as 1901[5]. Eventually, the term “giant pulsation,” or Pg, arose to describe such pulsations.

On the ground, Pgs are notable for their strikingly sinusoidal waveforms, their eastward drifts, and their specific occurrence pattern: Pgs are typically seen pre-dawn, at latitudes of 60° to 70° . Pgs generally fall into the Pc4 frequency band¹⁰. Their harmonic structure was a source of controversy for decades, but recent multisatellite observations seem to be in agreement that they are odd harmonics, probably fundamental[31, 41, 52, 53, 91, 94]. They are poloidally polarized, with modenumbers $10 \lesssim m \lesssim 40$ [29, 41, 77, 83, 94].

Whereas FLRs are waves in space which may produce ground signatures, “giant pulsation” refers to the ground signature specifically¹¹. That is, Takahashi’s satellite observation of a sinusoidal, morningside, high- m , fundamental poloidal resonance was not classified as a Pg because it did not produce a signal on the ground[92].

TODO: Pgs are localized to within 2° to 5° in latitude[72, 91, 100].

Due to their remarkably clear waveforms, Pgs are typically found by “visual inspection of magnetometer data”[72]. Over the course of the past century, a number of multi-year (sometimes multi-decade[7]) surveys have totaled nearly one thousand Pg events. On average, a ground magnetometer near 66° magnetic latitude observes ~ 10 Pg events per year[7, 40, 82, 89]. Observations are not distributed uniformly; rather, giant pulsations become more common near the equinox and during times of low solar activity.

Unlike Pc4 pulsations in general, Pgs show no particular correlation with storm phase[72]. However, they do often occur as the magnetosphere recovers from a substorm[72, 83].

⁹The term was first used by Alfvén in the 1940s[2].

¹⁰The Pc4 range is periods of 45 s to 140 s, while Pgs are often said to range from 60 s to 200 s[7].

¹¹Historically, the wave designations shown in Table 3.1 all referred to ground phenomena. Over time, they have come to describe satellite observations as well, including those without corresponding signatures on the ground.

3.5 Motivations for the Present Work

A great deal has been learned — and continues to be learned — through observations of field line resonance. However, the cost-to-benefit ratio is climbing. As summarized in the sections above, FLR behavior depends significantly on harmonic structure, azimuthal modenumber, and polarization — not to mention frequency, spectral width, and so on. With each degree of freedom comes the necessity for an additional simultaneous observation.

Similarly, as FLRs have been shown to depend on ever-more-specific magnetospheric conditions, analytical techniques have fallen out of favor. The height-resolved ionosphere, the multidimensional Alfvén speed profile, and the inconvenient geometry combine to create a problem beyond the reasonable purview of pencil and paper.

That is, the topic of field line resonance is ripe for numerical modeling.

Past models of the magnetosphere have been ill-suited for the consideration of FLRs. Reasons include overly-simplified treatment of the ionospheric boundary, no consideration of the plasmapause, limited range in m , and the inability to compute ground signatures. Chapter 5 presents a model which addresses these issues, allowing the computation of field line resonance with unparalleled attention to realism.

The model allows a bird’s-eye view of the structure and evolution of FLRs. As such, not only can several open questions be addressed, but their answers serve to unify a number of seemingly-disparate properties described in the sections above.

The rotation of poloidally-polarized waves to the toroidal mode is investigated. Particular attention is paid to the importance of azimuthal modenumber and ionospheric conductivity. The interplay between said rotation and the transport of energy across field lines — which also depends on azimuthal modenumber — is considered as well.

By their nature, drifting particles have the potential to spur wave-particle interactions at all MLT. However, Pc4 observations are strongly peaked on the dayside. In a 2015 paper, Dai notes, “It is not clear why noncompressional [high- m] Pc4 poloidal waves, which are presumably driven by instability within the magnetosphere, preferentially occur on the dayside”[17]. Motoba, later that year, echoes, “It is unclear whether other

generation mechanisms of fundamental standing waves ... can explain the localization of Pgs in local time”[72]. This, too, is considered numerically: to what degree is field line resonance affected by the (day-night asymmetric) conditions of the ionosphere?

TODO: Transition... With the above in mind, what data would be super helpful?

It’s been shown that a ground magnetometer 66° north of the magnetic equator observes \sim 10 Pg events per year. It’s also been shown that poloidal Pc4s are rare compared to toroidal ones, and that most poloidal Pc4s are even harmonics. However, little attention has been paid to how these rates line up with one another. Given the relative occurrence rate of poloidal and toroidal waves, of odd and even harmonics, and of diffuse and sharp spectral peaks, just how unusual are giant pulsations?

Chapter 4

Waves in Cold Resistive Plasma

Before delving into the implementation of the numerical model, it's instructive to consider the fundamental equations of waves in a cold, resistive plasma.

The evolution of electric and magnetic fields is governed by Ampère's law and Faraday's law. Notably, the present work takes the linearized versions of Maxwell's equations; the vectors \underline{E} and \underline{B} indicate perturbations above the zeroth-order magnetic field.

$$\underline{\epsilon} \cdot \frac{\partial}{\partial t} \underline{E} = \frac{1}{\mu_0} \nabla \times \underline{B} - \underline{J} \quad \frac{\partial}{\partial t} \underline{B} = -\nabla \times \underline{E} \quad (4.1)$$

Current follows Ohm's law. For currents perpendicular to the background magnetic field, Kirchhoff's formulation is sufficient. Conductivity is much higher along the magnetic field lines¹, so it's appropriate to also include the electron inertial term².

$$0 = \underline{\sigma}_{\perp} \cdot \underline{E}_{\perp} - \underline{J}_{\perp} \quad \frac{1}{\nu} \frac{\partial}{\partial t} J_z = \sigma_0 E_z - J_z \quad (4.2)$$

¹The dipole coordinate system is defined rigorously in Section 5.1; at present, it's sufficient to take \hat{z} parallel to the zeroth-order magnetic field, and \hat{x} and \hat{y} perpendicular to \hat{z} (and to each other).

²Electron inertial effects are not included in the model described in Chapter 5, or in the results in Chapter 7; however, their implementation and impact are explored in Chapter 6.

Derivatives in Equations (4.1) and (4.2) can be evaluated by performing a Fourier transform. They can then be combined, eliminating the magnetic field and current terms.

$$\begin{aligned} 0 &= \underline{\underline{E}}_{\perp} + \frac{v_A^2}{\omega^2} (\underline{k} \times \underline{k} \times \underline{E})_{\perp} + \frac{i}{\epsilon_{\perp}\omega} \underline{\sigma}_{\perp} \cdot \underline{\underline{E}}_{\perp} \\ 0 &= E_z + \frac{c^2}{\omega^2} (\underline{k} \times \underline{k} \times \underline{E})_z + \frac{i\omega_P^2}{\omega(\nu - i\omega)} E_z \end{aligned} \quad (4.3)$$

The speed of light, Alfvén speed (including the displacement current correction), plasma frequency, and parallel conductivity are defined in the usual way:

$$c^2 \equiv \frac{1}{\mu_0\epsilon_0} \quad v_A^2 \equiv \frac{1}{\mu_0\epsilon_{\perp}} \quad \omega_P^2 \equiv \frac{ne^2}{m_e\epsilon_0} \quad \sigma_0 \equiv \frac{ne^2}{m_e\nu} \quad (4.4)$$

Using the vector identity $\underline{k} \times \underline{k} \times \underline{E} = \underline{k} \underline{k} \cdot \underline{E} - k^2 \underline{E}$, Equation (4.3) can be reassembled into a single expression,

$$0 = \left(\underline{\underline{\mathbb{I}}} + \frac{1}{\omega^2} \underline{\underline{V}}^2 \cdot \underline{k} \underline{k} - \frac{k^2}{\omega^2} \underline{\underline{V}}^2 + \frac{i}{\omega} \underline{\underline{\Omega}} \right) \cdot \underline{E} \quad (4.5)$$

Where $\underline{\underline{\mathbb{I}}}$ is the identity tensor and in x - y - z coordinates,

$$\underline{\underline{V}}^2 \equiv \begin{bmatrix} v_A^2 & 0 & 0 \\ 0 & v_A^2 & 0 \\ 0 & 0 & c^2 \end{bmatrix} \quad \text{and} \quad \underline{\underline{\Omega}} \equiv \begin{bmatrix} \frac{\sigma_P}{\epsilon_{\perp}} & \frac{-\sigma_H}{\epsilon_{\perp}} & 0 \\ \frac{\sigma_H}{\epsilon_{\perp}} & \frac{\sigma_P}{\epsilon_{\perp}} & 0 \\ 0 & 0 & \frac{\omega_P^2}{(\nu - i\omega)} \end{bmatrix} \quad (4.6)$$

In Equation (4.5), the expression in parentheses is the dispersion tensor. Nontrivial solutions exist only when its determinant is zero. This gives rise to a seventh-order polynomial in ω , so rather than a direct solution it's necessary to consider limits of specific interest.

Without loss of generality, the wave vector \underline{k} may be taken to lie in the x - z plane — that is, with $k_y = 0$. The distinction between the two perpendicular directions is discussed in Section 4.4.

4.1 Guided Propagation

The wave vector of a field line resonance aligns closely to the background magnetic field. By supposing that the two align exactly (that is, taking $k_x = 0$), the parallel and perpendicular components of the dispersion relation are decoupled.

The parallel-polarized component — that is, the solution when $E_x = E_y = 0$ — is quadratic, and thus can be solved directly.

$$0 = \omega^2 + i\nu\omega - \omega_P^2 \quad \text{so} \quad \omega = -\frac{i\nu}{2} \pm \sqrt{\omega_P^2 - \frac{\nu^2}{4}} \quad (4.7)$$

It bears noting that the plasma frequency is large — not just compared to Pc4 frequencies, but even compared to the collision frequencies in the ionosphere³.

Expanding Equation (4.7) with respect to large ω_P , the dispersion relation becomes

$$\omega^2 = \omega_P^2 \pm i\nu\omega_P + \dots \quad (4.8)$$

Equation (4.8) can hardly be called a wave, as it does not depend on the wave vector \underline{k} . Rather, it is the plasma oscillation⁴: electrons vibrating in response to a charge separation along the background magnetic field.

The plasma oscillation is not specifically relevant to the study of field line resonance. The two phenomena are separated by six orders of magnitude in frequency. The topic is revisited in Chapter 6 insomuch as it is inseparable from the electron inertial effects in Ohm's law.

³The collision frequency may match or exceed the plasma frequency for a thin slice at the bottom of the ionosphere, where the density of neutral atoms is large; however, it falls off quickly. Above an altitude of 200 km, conservatively[75], the plasma frequency exceeds the collision frequency by an order of magnitude or more.

⁴The plasma oscillation is also called the Langmuir wave, after Irving Langmuir.

The perpendicular ($E_z = 0$) components of the dispersion relation give an expression quartic in ω .

$$0 = \omega^4 + 2i\frac{\sigma_P}{\epsilon_\perp}\omega^3 - \left(2k_z^2v_A^2 + \frac{\sigma_P^2 + \sigma_H^2}{\epsilon_\perp^2}\right)\omega^2 - 2ik_z^2v_A^2\frac{\sigma_P}{\epsilon_\perp}\omega + k_z^4v_A^4 \quad (4.9)$$

Like the parallel-polarized component above, Equation (4.9) can be solved directly. Noting that \pm and \oplus are independent,

$$\omega = \left(\frac{\pm\sigma_H - i\sigma_P}{2\epsilon_\perp}\right) \oplus \sqrt{k_z^2v_A^2 + \left(\frac{\pm\sigma_H - i\sigma_P}{2\epsilon_\perp}\right)^2} \quad (4.10)$$

Also like the parallel-polarized component, the exact solution is less useful than its Taylor expansion. The Pedersen and Hall conductivities are large near the ionospheric boundary, but fall off quickly; for the vast majority of the field line, the ratios $\frac{\sigma_P}{\epsilon_\perp}$ and $\frac{\sigma_H}{\epsilon_\perp}$ are small compared to field line resonance frequencies. Expanding with respect to small conductivity gives

$$\omega^2 = k_z^2v_A^2 \oplus k_zv_A\frac{\sigma_H \pm i\sigma_P}{\epsilon_\perp} + \dots \quad (4.11)$$

This is the shear Alfvén wave, with a shift to its frequency due to the conductivity of the ionosphere. It travels along the background magnetic field like a bead on a string, with electric and magnetic field perturbations perpendicular to the magnetic field line (and to one another).

4.2 Compressional Propagation

The partner to guided motion is compressional motion; in order for energy to move across field lines, the wave vector must have a component perpendicular to \hat{z} . If the wave vector is completely perpendicular to the magnetic field line ($k_z = 0$), the parallel and perpendicular components of the dispersion relation decouple, as in Section 4.1.

The parallel-polarized ($E_x = E_y = 0$) component of the dispersion relation is

$$0 = \omega^3 + i\nu\omega^2 - (k_x^2 c^2 + \omega_P^2) \omega - ik_x^2 c^2 \nu \quad (4.12)$$

Equation (4.12) can be solved directly, though its solution (as a cubic) is far too long to be useful. Expanding with respect to the large plasma frequency, gives

$$\omega^2 = k^2 c^2 + \omega_P^2 - i\nu\omega_P + \dots \quad (4.13)$$

This is the O mode, a compressional wave with an electric field perturbation along the background magnetic field. Like the plasma oscillation discussed in Section 4.1, its frequency is very large compared to that of a field line resonance.

The perpendicular-polarized ($E_z = 0$) component of the compressional dispersion relation is also cubic.

$$0 = \omega^3 + 2i\frac{\sigma_P}{\epsilon_\perp}\omega^2 - \left(2k_x^2 v_A^2 + \frac{\sigma_P^2 + \sigma_H^2}{\epsilon_\perp^2}\right)\omega - ik_x^2 v_A^2 \frac{\sigma_P}{\epsilon_\perp} \quad (4.14)$$

A wave moving across magnetic field lines near the ionospheric boundary will encounter large $\frac{\sigma_P}{\epsilon_\perp}$ and $\frac{\sigma_H}{\epsilon_\perp}$, while at moderate to high altitudes those ratios will be small. Solving Equation (4.14) in those two limits respectively gives:

$$\omega^2 = k_x^2 v_A^2 \pm ik_x v_A \frac{\sigma_P}{\epsilon_\perp} + \dots \quad \text{and} \quad \omega^2 = k_x^2 v_A^2 + \left(\frac{\sigma_H \pm i\sigma_P}{\epsilon_\perp}\right)^2 + \dots \quad (4.15)$$

In both limits, Equation (4.15) describes a compressional Alfvén wave. The magnetic field perturbation is along the background magnetic field — indicating compression of the frozen-in plasma — while the electric field perturbation is perpendicular to both the magnetic field and the wave vector.

TODO: Double check terminology. Jesse's dissertation disagrees with Bob's notes.

4.3 High Altitude Limit

In the limit of large radial distance, it's reasonable to take the collision frequency to zero; doing so also neglects the Pedersen and Hall conductivities.

Whereas in Sections 4.1 and 4.2 it was the parallel-polarized component of the dispersion relation that factored out from the other two, the high altitude limit decouples the component polarized out of the x - z plane. The y -polarized dispersion ($E_x = E_z = 0$) is simply:

$$\omega^2 = k^2 v_A^2 \quad (4.16)$$

Equation (4.16) describes an Alfvén wave with an arbitrary angle of propagation. Depending on the angle between the wave vector and the background magnetic field, it could be guided, compressional, or somewhere in between. Regardless of propagation angle, the electric field perturbation is perpendicular to both the direction of propagation and the magnetic field perturbation.

The other two components (from $E_y = 0$) of the high altitude dispersion tensor give an expression quadratic in ω^2 :

$$0 = \omega^4 - (k_x^2 c^2 + k_z^2 v_A^2 + \omega_P^2) \omega^2 + k_z^2 v_A^2 \omega_P^2 \quad (4.17)$$

Which can be solved for

$$\omega^2 = \frac{1}{2} (k_x^2 c^2 + k_z^2 v_A^2 + \omega_P^2) \pm \sqrt{\frac{1}{4} (k_x^2 c^2 + k_z^2 v_A^2 + \omega_P^2)^2 - k_z^2 v_A^2 \omega_P^2} \quad (4.18)$$

Noting again that ω_P is very large, the two roots can be expanded to

$$\omega^2 = k_z^2 v_A^2 \left(1 + \frac{k_x^2 c^2 + k_z^2 v_A^2}{\omega_P^2} \right) + \dots \quad \text{and} \quad \omega^2 = k_x^2 c^2 + k_z^2 v_A^2 + \omega_P^2 + \dots \quad (4.19)$$

The first is a shear Alfvén wave, as in Equation (4.11). The second oscillates faster than the plasma frequency; like the plasma oscillation in Equation (4.8) and the O mode in Equation (4.13), it's far outside the Pc4 frequency range.

4.4 Implications to the Present Work

The present section's findings carry three significant implications for the present work.

First — with the exception of the plasma oscillation and similar modes, which are revisited in Chapter 6 — waves propagate at the Alfvén speed. This, in combination with the grid configuration, will constrain the time step that can be used to model them numerically. The time step must be sufficiently small that information traveling at the Alfvén speed cannot “skip over” entire grid cells⁵.

Second, the results of the present section allow an estimate of the magnitude of parallel electric field that might be expected from a field line resonance compared to its perpendicular electric field. Between the full dispersion tensor form in Equation (4.5) and the Alfvén wave described by Equation (4.19),

$$\left| \frac{E_z}{E_x} \right| = \frac{k_x k_z c^2}{\omega^2 - k_x^2 c^2 - \omega_P^2} \sim \frac{k^2 c^2}{\omega_P^2} \quad (4.20)$$

In essence, the relative magnitudes of the parallel and perpendicular electric fields should be in proportion to the square of the relative magnitudes of the electron inertial length (1 km to 100 km) and the wavelength ($\sim 10^5$ km). That is, parallel electric fields should be smaller than the perpendicular electric fields by six or more orders of magnitude.

Finally, the dispersion relations shown above indicate how the behavior of a field line resonance should behave as the azimuthal modenumber becomes large.

Whereas the shear Alfvén wave's dispersion relation depends only on the parallel component of the wave vector, the compressional Alfvén wave depends on its magnitude: $\omega^2 = k^2 v_A^2$. If the frequency is smaller than $k v_A$, the wave will become evanescent. The

⁵As is the convention, the time step is scaled down from the smallest Alfvén zone crossing time by a Courant factor, typically 0.1, meaning that it takes at least ten time steps to cross a grid cell.

wave vector's magnitude can be no smaller than its smallest component, however, and the azimuthal component scales with the azimuthal modenumber: $k_y \sim \frac{m}{2\pi r}$.

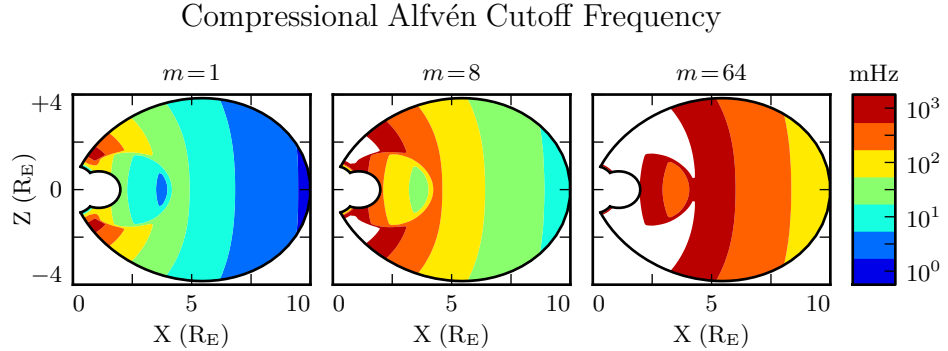


Figure 4.1: Taking $k_y \sim \frac{m}{2\pi r}$ as a lower bound for the magnitude of the wave vector, the above figure demonstrates the lowest frequency at which compressional Alfvén waves may propagate as a function of position and m . Regions shown in white are off the color scale — they have a lower bound on the order of 10^4 mHz or more. The above Alfvén frequency profile is from Kelley[49], for quiet dayside conditions, as discussed in Section 5.2.

This imposes a frequency cutoff on compressional Alfvén waves which scales with the azimuthal modenumber, as shown in Figure 4.1. At small values of m , most of the magnetosphere is conducive to compressional Alfvén waves in the Pc4 frequency range. As m increases, and the wave vector with it, the inner magnetosphere becomes increasingly inaccessible to them.

Chapter 5

“Tuna Half” Dimensional Model

The present section describes the implementation of Tuna, a new two and a half dimensional Alfvén wave code based largely on work by Lysak[60, 63].

The half-integer dimensionality refers to the fact that Tuna’s spatial grid resolves a two-dimensional slice of the magnetosphere, but that electric and magnetic fields — as well as their curls — are three-dimensional vectors. This apparent contradiction is reconciled by the use of a fixed azimuthal modenumber, m . Electric and magnetic fields are taken to be complex-valued, varying azimuthally per $\exp(im\phi)$; derivatives with respect to ϕ are then replaced by a factor of im .

Unlike a fully three-dimensional code, Tuna cannot resolve the evolution of wave structures in the azimuthal direction. Furthermore, the model does not allow coupling between the dayside and nightside magnetospheres. What Tuna does offer is efficiency. The model’s economical geometry allows it to include a realistic Earthward boundary: grid spacing on the order of 10 km, a height-resolved ionospheric conductivity tensor, and even the computation of magnetic field signatures at the ground. Such features are computationally infeasible for a large global code.

Tuna was developed with field line resonance in mind. As discussed in Chapter 3, such waves are azimuthally localized, minimizing the importance of Tuna’s missing half dimension. Moreover, because field line resonances are known to be affected by both

the ionosphere and the plasmasphere, a faithful treatment of the inner magnetosphere is a crucial part of studying them numerically.

Perhaps the most exciting feature of Tuna is its novel driving mechanism: ring current perturbation. Codes similar to Tuna have traditionally been driven using compressional pulses at the outer boundary[60, 63, 102, 103]. This has precluded the investigation of waves with large azimuthal modenumber — such as giant pulsations — which are guided, and thus must be driven from within the magnetosphere.

TODO: The dipole geometry isn't super new, but it's not widely used. The height-resolved ionosphere is new and exciting! Ground signatures are new and exciting!

TODO: The support software — the driver and the plotter — are also significant. Do they get mentioned here? Does the Git repository where the code can be accessed get mentioned here?

5.1 Coordinate System

Field line resonance has traditionally been modeled by straightening the field lines into a rectangular configuration[22, 66], by unrolling the azimuthal coordinate into a cylindrical coordinate system[80], or through the use of dipole coordinates[79]¹:

$$x \equiv -\frac{\sin^2 \theta}{r} \quad y \equiv \phi \quad z \equiv \frac{\cos \theta}{r^2} \quad (5.1)$$

Where r , θ , and ϕ take on their usual spherical meanings of radial distance, colatitude, and azimuthal angle respectively.

The dipole coordinate x is constant over each equipotential shell², y is azimuthal angle, and z indexes each field line from south to north. The unit vectors \hat{x} , \hat{y} , and \hat{z} point

¹The dipole coordinates x , y and z are perhaps more commonly named μ , ϕ , and ν respectively; however, in the present work, μ and ν take other meanings.

²In fact, x is inversely proportional to the McIlwain parameter L .

in the crosswise³ (radially outward at the equator), azimuthal (eastward), and parallel (northward at the equator) directions respectively.

Notably, the dipole coordinates in Equation (5.1) are normal to one another. While mathematically convenient, they do not readily accommodate a fixed-altitude boundary at the ionosphere, nor do they allow the dipole magnetic field to intersect the boundary at an oblique angle, as Earth's field does. As a solution, a nonorthogonal set of dipole coordinates was developed numerically by Proehl[78], then formalized analytically by Lysak[60] in terms of their contravariant components:

$$u^1 = -\frac{R_I}{r} \sin^2 \theta \quad u^2 = \phi \quad u^3 = \frac{R_I^2}{r^2} \frac{\cos \theta}{\cos \theta_0} \quad (5.2)$$

Above, R_I is the position of the ionosphere relative to Earth's center; it's typically taken to be $1 R_E + 100 \text{ km}$.

Like the dipole coordinates x , y , and z , Lysak's coordinates u^1 , u^2 , and u^3 correspond to L -shell, azimuthal angle, and position along a field line respectively. However, compared to z , u^3 has been renormalized using the invariant colatitude⁴ θ_0 . As a result, u^3 takes the value $+1$ at the northern ionospheric boundary and -1 at the southern ionospheric boundary for all field lines.

Because Lysak's coordinate system is not orthogonal⁵, it's necessary to consider covariant and contravariant basis vectors separately.

$$\hat{e}_i \equiv \frac{\partial}{\partial u^i} \underline{x} \quad \hat{e}^i \equiv \frac{\partial}{\partial \underline{x}} u^i \quad (5.3)$$

Covariant basis vectors \hat{e}_i are normal to the curve defined by constant u^i , while contravariant basis vectors \hat{e}^i are tangent to the coordinate curve (equivalently, \hat{e}^i is normal

³In the context of in situ measurements taken near the equatorial plane, \hat{x} is referred to as the radial direction; however, the present work extends the dipole grid to low altitudes, where \hat{x} can be more horizontal than vertical. The term "crosswise" is meant to indicate that \hat{x} is defined by the cross product of \hat{y} and \hat{z} .

⁴The invariant colatitude is the colatitude θ at which a field line intersects the ionosphere. It is related to the McIlwain parameter by $\cos \theta_0 \equiv \sqrt{1 - \frac{R_I}{L}}$.

⁵Curves of constant u^1 and curves of constant u^3 can intersect at non-right angles.

to the plane defined by constant u^j for all $j \neq i$). These vectors are reciprocal⁶ to one another, and can be combined to give components of the metric tensor $\underline{\underline{g}}$ [20].

$$\hat{e}^i \cdot \hat{e}_j = \delta_j^i \quad g_{ij} \equiv \hat{e}_i \cdot \hat{e}_j \quad g^{ij} \equiv \hat{e}^i \cdot \hat{e}^j \quad (5.4)$$

The metric tensor allows rotation between covariant and contravariant representations of vectors.

$$A_i = g_{ij} A^j \quad \text{and} \quad A^i = g^{ij} A_j \quad \text{where} \quad A_i \equiv \underline{A} \cdot \hat{e}_i \quad \text{and} \quad A^i \equiv \underline{A} \cdot \hat{e}^i \quad (5.5)$$

In addition, the determinant of the metric tensor is used to define cross products and curls⁷.

$$(\underline{A} \times \underline{B})^i = \frac{\varepsilon^{ijk}}{\sqrt{g}} A_j B_k \quad \text{and} \quad (\nabla \times \underline{A})^i = \frac{\varepsilon^{ijk}}{\sqrt{g}} \frac{\partial}{\partial u^j} A_k \quad \text{where} \quad g \equiv \det \underline{\underline{g}} \quad (5.6)$$

Explicit forms of the basis vectors and metric tensor can be found in the appendix of Lysak's 2004 paper[60]. At present, it's sufficient to note the mapping between Lysak's basis vectors and the usual dipole unit vectors.

$$\hat{x} = \frac{1}{\sqrt{g^{11}}} \hat{e}^1 \quad \hat{y} = \frac{1}{\sqrt{g^{22}}} \hat{e}^2 \quad \hat{z} = \frac{1}{\sqrt{g^{33}}} \hat{e}^3 \quad (5.7)$$

TODO: Do these need to be written out? Referring people to the code, which will be in a public Git repository, is also a possibility.

The basis vectors can also be mapped to the spherical unit vectors, though Equation (5.8) is valid only at the ionospheric boundary.

$$\hat{\theta} = \frac{1}{\sqrt{g_{11}}} \hat{e}_1 \quad \hat{\phi} = \frac{1}{\sqrt{g_{22}}} \hat{e}_2 \quad \hat{r} = \frac{1}{\sqrt{g_{33}}} \hat{e}_3 \quad (5.8)$$

⁶The symbol δ_j^i is the Kronecker delta; the present work also makes use of the Levi-Civita symbol ε^{ijk} and Einstein's convention of implied summation over repeated indeces[24].

⁷The square root of the determinant of the metric tensor is called the Jacobian. It's sometimes denoted using the letter J , which is reserved for current in the present work.

The coordinates converge at the equatorial ionosphere, so an inner boundary is necessary to maintain finite grid spacing. It's typically placed at $L = 2$. The outer boundary is at $L = 10$. The dipole approximation of Earth's magnetic field is tenuous at the outer boundary (particularly on the dayside); however, in practice, wave activity is localized inside $L \sim 7$. The grid is spaced uniformly in u^1 , which gives finer resolution close to Earth and coarser resolution at large distances.

Spacing in u^3 is set by placing grid points along the outermost field line. The points are closest together at the ionosphere, and grow towards the equator. The spacing increases in a geometric fashion, typically by 3%.

Typically, Tuna uses a grid 150 points in u^1 by 350 points in u^3 . The result is a resolution on the order of 10 km at the ionosphere, which increases to the order of 10³ km at the midpoint of the outermost field line.

There are no grid points in u^2 due to the two-and-a-half-dimensional nature of the model. Fields are assumed to vary as $\exp(imu^2)$ — equally, $\exp(im\phi)$ — so derivatives with respect to u^2 are equivalent to a factor of im . In effect, the real component of each field is azimuthally in phase with the (purely real) driving, while imaginary values represent behavior that is azimuthally offset.

The simulation's time step is set based on the grid spacing. As is the convention, δt is set to match the smallest Alfvén zone crossing time, scaled down by a Courant factor (typically 0.1). It bears noting that the smallest crossing time need not correspond to the smallest zone; the Alfvén speed peaks several thousand kilometers above Earth's surface, in the so-called Ionospheric Alfvén Resonator[63]. A typical time step is on the order of 10⁻⁵ s.

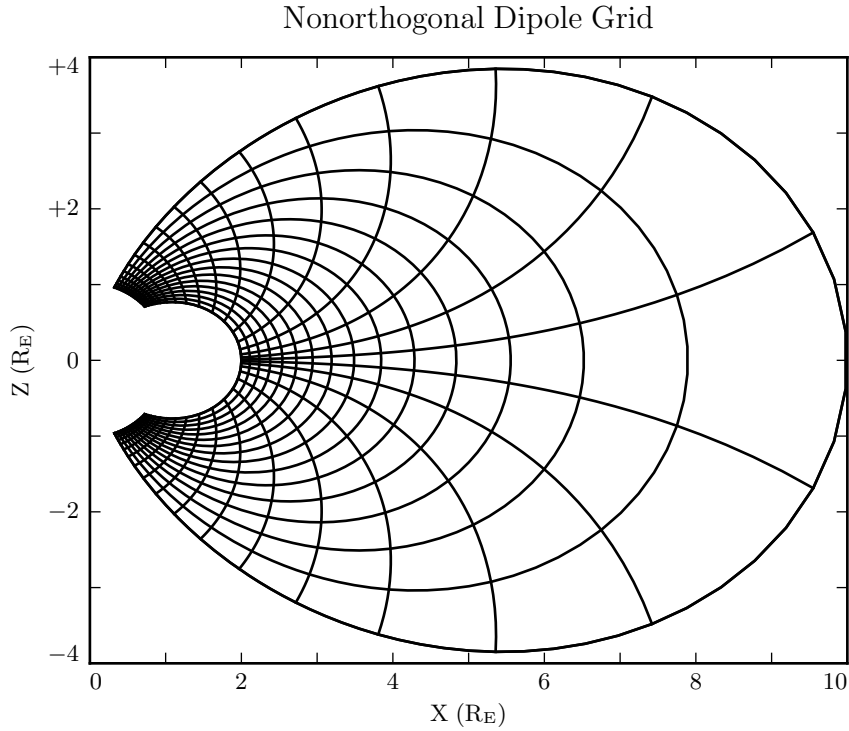


Figure 5.1: The model’s nonorthogonal dipole grid. Every fifth point is shown in each direction. The high concentration of grid points near Earth’s equator is a consequence of the coordinate system, which converges at the equatorial ionosphere. Earth (not shown) is centered at the origin with unit radius.

5.2 Physical Parameter Profiles

Tuna models Earth’s magnetic field to be an ideal dipole, so the zeroth-order field strength is written in the usual form:

$$\underline{B}_0 = 3.1 \times 10^4 \text{ nT} \left(\frac{R_E}{r} \right)^3 \left(2 \cos \theta \hat{r} - \sin \theta \hat{\theta} \right) \quad (5.9)$$

Number density is taken to be the sum of an inverse-radial-dependent auroral profile and a plasmaspheric profile dependent on the L -shell[63]:

$$n = n_{AZ} \frac{r_{AZ}}{r} + n_{PS} \exp\left(\frac{-L}{L_{PS}}\right) \left(\frac{1}{2} - \frac{1}{2} \tanh \frac{L - L_{PP}}{\delta L_{PP}} \right) \quad (5.10)$$

Where typical values are shown in Table 5.1.

Table 5.1: Typical Parameters for the Tuna Density Profile

Variable	Value	Description
L_{PS}	1.1	Scale L of the plasmasphere.
L_{PP}	4.0	Location of the plasmapause.
δL_{PP}	0.1	Thickness of the plasmapause.
n_{AZ}	$10 / \text{cm}^3$	Number density at the base of the auroral zone.
n_{PS}	$10^4 / \text{cm}^3$	Number density at the base of the plasmasphere.
r_{AZ}	1 R_E	Scale height of the auroral density distribution.

The perpendicular component of the electric tensor, ϵ_{\perp} , is computed based on Kelley's[49] tabulated low-density values, ϵ_K , which are adjusted to take into account the effects of high density in the plasmapause.

$$\epsilon_{\perp} = \epsilon_K + \frac{Mn}{B_0^2} \quad (5.11)$$

Where M is the mean molecular mass, which is large ($\sim 28 \text{ u}$) at 100 km altitude, then drops quickly (down to 1 u by $\sim 1000 \text{ km}$)[63].

The Alfvén speed profile is computed from the perpendicular electric constant in the usual way, $v_A^2 \equiv \frac{1}{\mu_0 \epsilon_{\perp}}$. This form takes into account the effect of the displacement current, which becomes important in regions where the Alfvén speed approaches the speed of light.

While the density profile is held constant for all runs discussed in the present work, the Alfvén speed profile is not. Four different profiles are used for the low-density

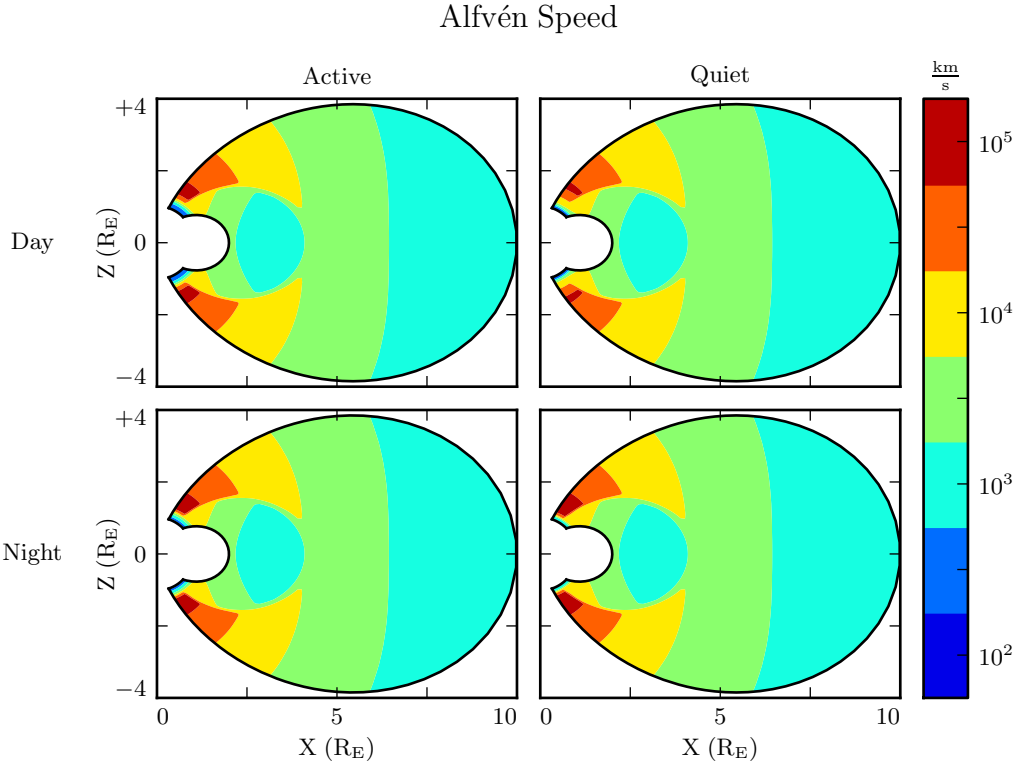


Figure 5.2: Alfvén speed profiles are based on low-density values tabulated by Kelley[49]. They are adjusted to take into account the density of the plasmapause and mass loading near the Earthward boundary.

perpendicular electric constant ϵ_K , corresponding to the differing ionospheric conditions between the dayside and the nightside, and between the high and low points in the solar cycle. These differences are visible in Figure 5.2, particularly in the size of the ionospheric Alfvén resonator (the peak in Alfvén speed in the high-latitude ionosphere).

TODO: Runs are only carried out for day and night... is it even worth showing the flank profile?

Ionospheric conductivity profiles are also based on values tabulated by Kelley, adjusted by Lysak[63] to take into account the abundance of heavy ions near the Earthward boundary. Pedersen, Hall, and parallel conductivities are each resolved by altitude, as shown in Figure 5.3.

Pedersen (Blue), Hall (Red), and Parallel (Green) Conductivities

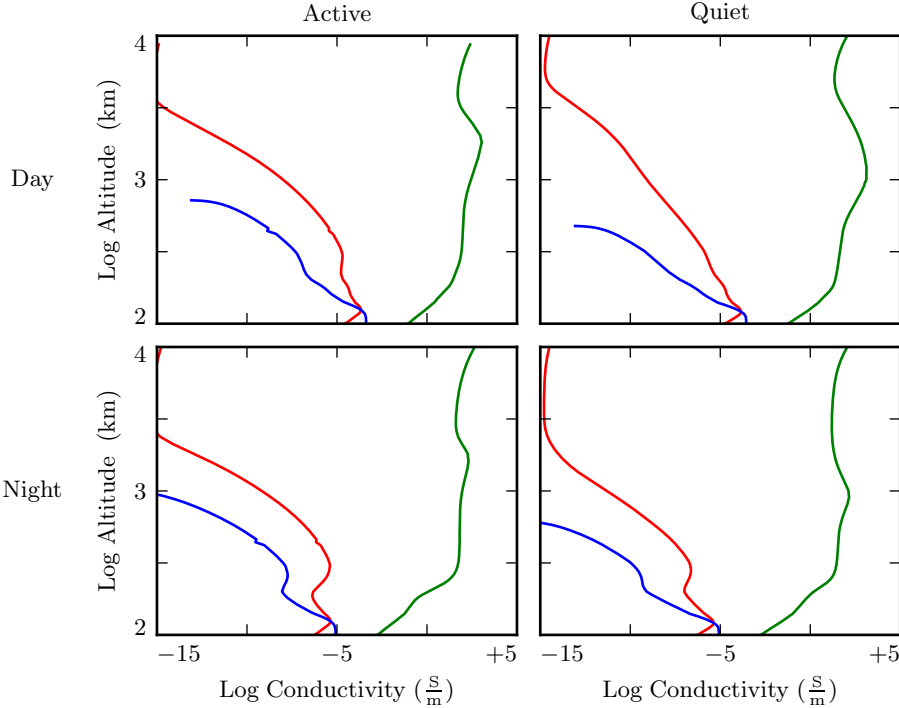


Figure 5.3: Ionospheric conductivity profiles are adapted by Lysak[63] from Kelley's tabulated values[49]. These profiles allow Tuna to simulate magnetosphere-ionosphere coupling under a variety of conditions.

Tuna's physical parameter profiles are static over the course of each run. Even so-called ultra low frequency waves like Pc4 pulsations are fast compared to convective timescales in the magnetosphere.

5.3 Driving

Models similar to Tuna have traditionally been driven using compression at the outer boundary[60, 63, 102, 103]. Such driving acts as a proxy for solar wind compression, Kelvin-Helmholtz effects at the magnetopause, and so on. However, because of the constraints imposed by the dispersion relation for Alfvén waves⁸, simulations driven from the outer boundary are constrained to the consideration of waves with low azimuthal modenumber (equivalently, large azimuthal wavelength).

This issue is demonstrated in Figure 5.4. At low modenumber, energy delivered at the outer boundary propagates across field lines in order to stimulate resonances in the inner magnetosphere. However, as modenumber increases, Alfvén waves become increasingly guided, and the inner magnetosphere is unaffected by perturbations at the outer boundary.

In order to simulate high-modenumber Alfvén waves in the inner magnetosphere — such as giant pulsations — a new driving mechanism is necessary. Perturbation of the ring current is a natural choice, as Alfvén waves in the Pc4 range are known to interact with ring current particles through drift and drift-bounce resonances. The ring current is a dynamic region, particularly during and after geomagnetic storms; it's easy to imagine the formation of localized inhomogeneities.

In order to estimate an appropriate magnitude for perturbations of the ring current, the Sym-H storm index is used. The index is measured once per minute, and so cannot directly detect ring current modulations in the Pc4 frequency range. Instead, the index is transformed into the frequency domain, allowing a fit of its pink noise⁹.

TODO: Sym-H is basically the same as Dst[101].

As shown in Figure 5.5, a Fourier transform of the Sym-H index (taken here from the June 2013 storm) suggests that magnetic field perturbations at Earth's surface due to ring current activity in the Pc4 frequency range could be up to the order of 10^{-2} nT. Supposing that the ring current is centered around $5 R_E$ geocentric, that corresponds to

⁸See Section 4.4.

⁹Pink noise, also called $\frac{1}{f}$ noise, refers to the power law decay present in the Fourier transforms of all manner of physical signals.

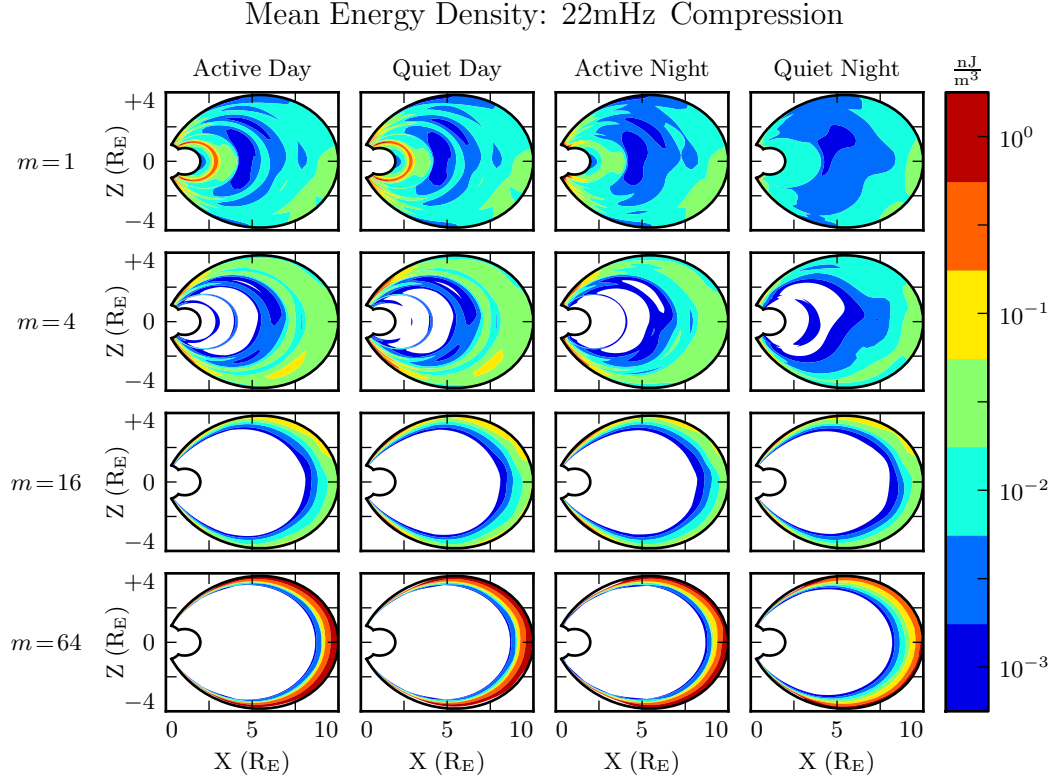


Figure 5.4: Each cell presents the mean energy density over the course of a 300s run, as a function of position, due to compressional driving at the outer boundary. Azimuthal modenumber varies by row, and ionospheric conditions vary by column. For runs with small azimuthal modenumber, it's clear that energy is able to propagate across field lines and stimulate wave activity in the inner magnetosphere. When the modenumber is large, energy is unable to penetrate to the inner magnetosphere. Notably, the large values on the bottom row should be taken with a grain of salt; it's not clear that the model's results are reliable when waves are continuously forced against the boundary.

a current on the order of 0.1 MA. Tuna's driving is spread using a Gaussian profile in u^1 (typically centered at $L = 5$) and u^3 (typically centered just off the equator), with a characteristic area of $1 R_E^2$; this gives a current density on the order of $10^{-4} \mu\text{A}/\text{m}^2$.

TODO: Admittedly, estimating the strength of localized perturbations using Sym-H — an index averaged over the entire globe — is a bit of a kludge.

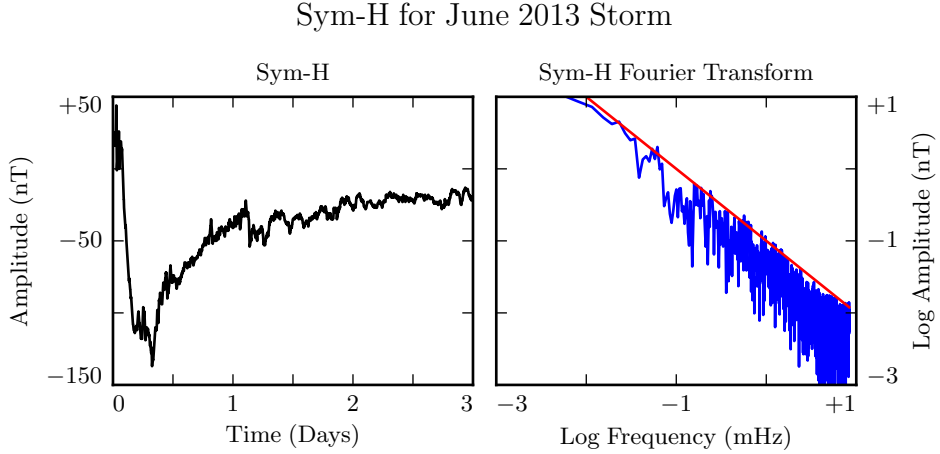


Figure 5.5: The Sym-H storm index[73] measures magnetic perturbations on Earth’s surface due to ring current activity. The amplitude of oscillations in the Pc4 range is estimated by fitting the pink noise in its Fourier transform.

In situ observations of Pc4 pulsations and giant pulsations have shown waves with modenumbers across the range $1 \lesssim m \lesssim 100$ [17, 18, 92]. Simulations are carried out across that range, corresponding to ring current perturbations with azimuthal extent as small as $0.5 R_E$.

TODO: Driving is delivered in the azimuthal component of the current only.

TODO: Driving is sinusoidal.

TODO: In case it’s not clear: Chapter 7 discusses ONLY simulations using ring current driving. The only compressional driving we look at is Figure 5.4.

5.4 Maxwell’s Equations

Tuna simulates the evolution of electromagnetic waves in accordance with Ampère’s law and Faraday’s law. Computation is carried out on a Yee grid[107]: electric fields and magnetic fields are offset by half a time step, and each field component is defined

on either odd or even grid points in each dimension to ensure that curls are computed using centered differences.

The Ohmic current in Ampère's law is replaced with $\underline{\sigma} \cdot \underline{E}$ per Kirchhoff's formulation of Ohm's law. Then, taking \underline{J} to represent the driving current discussed in Section 5.3, Maxwell's equations can be written

$$\frac{\partial}{\partial t} \underline{B} = -\nabla \times \underline{E} \quad \underline{\epsilon} \cdot \frac{\partial}{\partial t} \underline{E} = \frac{1}{\mu_0} \nabla \times \underline{B} - \underline{J} - \underline{\sigma} \cdot \underline{E} \quad (5.12)$$

It is convenient to introduce shorthand for the curl of each field: $\underline{C} \equiv \nabla \times \underline{E}$ and $\underline{F} \equiv \nabla \times \underline{B} - \mu_0 \underline{J}$. Or, recalling Equation (5.6),

$$C^i = \frac{\varepsilon^{ijk}}{\sqrt{g}} \frac{\partial}{\partial u^j} E_k \quad F^i = \frac{\varepsilon^{ijk}}{\sqrt{g}} \frac{\partial}{\partial u^j} B_k - J^i \quad (5.13)$$

In these terms, Faraday's law can simply be written:

$$\frac{\partial}{\partial t} B^i = -C^i \quad (5.14)$$

Writing each component out explicitly, and using the metric tensor (per Equation (5.5)) to eliminate contravariant magnetic field components¹⁰, Equation (5.14) becomes:

$$\begin{aligned} B_1 &\leftarrow B_1 - g_{11} \delta t C^1 - g_{13} \delta t C^3 \\ B_2 &\leftarrow B_2 - g_{22} \delta t C^2 \\ B_3 &\leftarrow B_3 - g_{31} \delta t C^1 - g_{33} \delta t C^3 \end{aligned} \quad (5.15)$$

Note that the \leftarrow operator is used in Equation (5.15) to indicate assignment, rather than equality. Terms on the left are new, while those on the right are old.

¹⁰Fields are stored only in terms of their covariant components, and curls in terms of their contravariant components. This reduces Tuna's memory footprint (since each field need not be stored twice) as well as its computational cost (since time need not be spent rotating between bases). As a result, Tuna's solutions to Maxwell's equations are linear expressions whose coefficients are a mishmash of physical constants and geometric factors. To save time, each coefficient is computed once and stored, rather than being multiplied out from scratch with each time step.

Unlike Faraday's law, Ampère's law cannot be trivially solved. Not only does the derivative of \underline{E} depend on its own future value, but the crosswise and azimuthal components of the equation are coupled by the Hall terms in the conductivity tensor. Fortunately, the electric tensor can be inverted, allowing a solution by integrating factors:

$$\underline{\epsilon} \cdot \frac{\partial}{\partial t} \underline{E} = \frac{1}{\mu_0} \underline{F} - \underline{\sigma} \cdot \underline{E} \quad \text{becomes} \quad \left(\underline{\Omega} + \underline{\mathbb{I}} \frac{\partial}{\partial t} \right) \cdot \underline{E} = \underline{V}^2 \cdot \underline{F} \quad (5.16)$$

Where $\underline{\mathbb{I}}$ is the identity tensor and in x - y - z coordinates¹¹,

$$\underline{V}^2 \equiv \frac{1}{\mu_0} \underline{\epsilon}^{-1} = \begin{bmatrix} v_A^2 & 0 & 0 \\ 0 & v_A^2 & 0 \\ 0 & 0 & c^2 \end{bmatrix} \quad \text{and} \quad \underline{\Omega} \equiv \underline{\epsilon}^{-1} \cdot \underline{\sigma} = \begin{bmatrix} \frac{\sigma_P}{\epsilon_{\perp}} & \frac{-\sigma_H}{\epsilon_{\perp}} & 0 \\ \frac{\sigma_H}{\epsilon_{\perp}} & \frac{\sigma_P}{\epsilon_{\perp}} & 0 \\ 0 & 0 & \frac{\sigma_0}{\epsilon_0} \end{bmatrix} \quad (5.17)$$

Multiplying through by $\exp(\underline{\Omega} t)$ and applying the product rule, Equation (5.16) becomes¹²

$$\frac{\partial}{\partial t} \left(\exp(\underline{\Omega} t) \cdot \underline{E} \right) = \exp(\underline{\Omega} t) \cdot \underline{V}^2 \cdot \underline{F} \quad (5.18)$$

Equation (5.18) can then be integrated over a small time step δt and expressed in terms of the assignment operator introduced in Equation (5.15).

$$\underline{E} \leftarrow \exp(-\underline{\Omega} \delta t) \cdot \underline{E} + \delta t \exp(-\underline{\Omega} \frac{\delta t}{2}) \cdot \underline{V}^2 \cdot \underline{F} \quad (5.19)$$

The tensor exponential can be evaluated by splitting $\underline{\Omega}$ into the sum of its diagonal and Hall components¹³. The Hall exponential condenses into sines and cosines, giving a rotation around the magnetic field line:

$$\underline{E} \leftarrow \exp(-\underline{\Omega}' \delta t) \cdot \underline{R}_z \left(\frac{-\sigma_H \delta t}{\epsilon_{\perp}} \right) \cdot \underline{E} + \delta t \underline{V}^2 \cdot \exp(-\underline{\Omega}' \frac{\delta t}{2}) \cdot \underline{R}_z \left(\frac{-\sigma_H \delta t}{2\epsilon_{\perp}} \right) \cdot \underline{F} \quad (5.20)$$

¹¹Note the parallel component of the present definition of $\underline{\Omega}$ differs slightly from that used in Chapter 4, due to the present neglect of inertial effects; see Chapter 6.

¹²Tensor exponentiation is analogous to scalar exponentiation[38]: $\exp(\underline{T}) \equiv \sum_n \frac{1}{n!} \underline{T}^n$.

¹³For tensors, $\exp(\underline{S} + \underline{T}) = \exp(\underline{S}) \exp(\underline{T})$ as long as $\underline{S} \cdot \underline{T} = \underline{T} \cdot \underline{S}$.

Where

$$\underline{\underline{R}}_z(\theta) = \begin{bmatrix} \cos \theta & -\sin \theta & 0 \\ \sin \theta & \cos \theta & 0 \\ 0 & 0 & 1 \end{bmatrix} \quad \text{and} \quad \underline{\underline{\Omega}}' \equiv \begin{bmatrix} \frac{\sigma_P}{\epsilon_{\perp}} & 0 & 0 \\ 0 & \frac{\sigma_P}{\epsilon_{\perp}} & 0 \\ 0 & 0 & \frac{\sigma_0}{\epsilon_0} \end{bmatrix} \quad (5.21)$$

The parallel component of term of Equation (5.20) is simply

$$E_z \leftarrow E_z \exp\left(\frac{-\sigma_0 \delta t}{\epsilon_0}\right) + c^2 \delta t F_z \exp\left(\frac{-\sigma_0 \delta t}{2\epsilon_0}\right) \quad (5.22)$$

Or, using Equation (5.7) to map to the covariant basis,

$$E_3 \leftarrow E_3 \exp\left(\frac{-\sigma_0 \delta t}{\epsilon_0}\right) + c^2 \delta t (g_{31} F^1 + g_{33} F^3) \exp\left(\frac{-\sigma_0 \delta t}{2\epsilon_0}\right) \quad (5.23)$$

Tuna's conductivity profile gives a minimum value of $\frac{\sigma_0 \delta t}{\epsilon_0}$ on the order of 10^3 , making $\exp\left(\frac{-\sigma_0 \delta t}{\epsilon_0}\right)$ far too small to be stored in a double precision variable¹⁴. That is, this model takes E_3 (and, proportionally, E_z) to be uniformly zero. This issue is revisited in Chapter 6.

The perpendicular components of Equation (5.20) give the expressions:

$$\begin{aligned} E_1 + \frac{g^{13}}{g^{11}} E_3 &\leftarrow E_1 \cos\left(\frac{-\sigma_H \delta t}{\epsilon_{\perp}}\right) \exp\left(\frac{-\sigma_P \delta t}{\epsilon_{\perp}}\right) \\ &\quad + E_2 \sin\left(\frac{-\sigma_H \delta t}{\epsilon_{\perp}}\right) \exp\left(\frac{-\sigma_P \delta t}{\epsilon_{\perp}}\right) \sqrt{\frac{g^{22}}{g^{11}}} \\ &\quad + E_3 \cos\left(\frac{-\sigma_H \delta t}{\epsilon_{\perp}}\right) \exp\left(\frac{-\sigma_P \delta t}{\epsilon_{\perp}}\right) \frac{g^{13}}{g^{11}} \\ &\quad + F^1 \cos\left(\frac{-\sigma_H \delta t}{2\epsilon_{\perp}}\right) \exp\left(\frac{-\sigma_P \delta t}{2\epsilon_{\perp}}\right) \frac{v_A^2 \delta t}{g^{11}} \\ &\quad + F^2 \sin\left(\frac{-\sigma_H \delta t}{2\epsilon_{\perp}}\right) \exp\left(\frac{-\sigma_P \delta t}{2\epsilon_{\perp}}\right) \frac{v_A^2 \delta t}{\sqrt{g^{11} g^{22}}} \end{aligned} \quad (5.24)$$

¹⁴Not coincidentally, $\frac{\sigma_0}{\epsilon_0}$ can also be written $\frac{\omega_P^2}{\nu}$. At the ionosphere, the collision frequency ν is fast compared to field line resonance timescales, but it's still slow compared to the plasma frequency.

and

$$\begin{aligned}
E_2 \leftarrow & -E_1 \sin\left(\frac{-\sigma_H \delta t}{\epsilon_{\perp}}\right) \exp\left(\frac{-\sigma_P \delta t}{\epsilon_{\perp}}\right) \sqrt{\frac{g^{11}}{g^{22}}} \\
& + E_2 \cos\left(\frac{-\sigma_H \delta t}{\epsilon_{\perp}}\right) \exp\left(\frac{-\sigma_P \delta t}{\epsilon_{\perp}}\right) \\
& - E_3 \sin\left(\frac{-\sigma_H \delta t}{\epsilon_{\perp}}\right) \exp\left(\frac{-\sigma_P \delta t}{\epsilon_{\perp}}\right) \frac{g^{13}}{\sqrt{g^{11} g^{22}}} \\
& - F^1 \sin\left(\frac{-\sigma_H \delta t}{2\epsilon_{\perp}}\right) \exp\left(\frac{-\sigma_P \delta t}{2\epsilon_{\perp}}\right) \frac{v_A^2 \delta t}{\sqrt{g^{11} g^{22}}} \\
& + F^2 \cos\left(\frac{-\sigma_H \delta t}{2\epsilon_{\perp}}\right) \exp\left(\frac{-\sigma_P \delta t}{2\epsilon_{\perp}}\right) \frac{v_A^2 \delta t}{g^{22}}
\end{aligned} \tag{5.25}$$

The E_3 terms in Equations (5.24) and (5.25) can be ignored at present. They are revisited in Chapter 6.

It bears recalling that the driving current is defined as part of \underline{F} , per Equation (5.13). When the driving current is purely azimuthal ($J^1 = J^3 = 0$), the driving is in principle applied to both the poloidal and the toroidal electric fields through F^2 . However, in practice, the driving applied to the toroidal electric field is vanishingly small. The driving current J^2 is localized around $5 R_E$ geocentric, and $\exp\left(\frac{-\sigma_P \delta t}{2\epsilon_{\perp}}\right)$ drops off quickly with altitude.

5.5 Boundary Conditions

Dirichlet and Neumann boundary conditions are applied to the electric field components and magnetic field components respectively. That is, electric fields are forced to go to zero at the inner and outer boundaries, and magnetic fields are forced to have a zero derivative normal to the inner and outer boundaries.

These boundary conditions can in principle cause nonphysical reflections at the boundary¹⁵. However, in practice, wave activity is concentrated well within the simulation domain. Simulation results are robust under an exchange of Dirichlet and Neumann

¹⁵See, for example, the bottom row of Figure 5.4.

boundary conditions (though a self-inconsistent set of boundary conditions, such as applying Neumann boundary conditions to B_1 but Dirichlet boundary conditions to B_3 , quickly causes instability).

The Earthward boundary conditions are as follows.

Between the top of the neutral atmosphere and the bottom of the ionosphere, the model includes a thin, horizontal current sheet representing the ionosphere's E layer[60]. By integrating Ampère's law over the layer, it can be shown[28] that the horizontal electric field values at the edge of the grid are determined by the jump in the horizontal magnetic fields:

$$\underline{\underline{\Sigma}} \cdot \underline{E} = \frac{1}{\mu_0} \lim_{\delta r \rightarrow 0} \left[\hat{r} \times \underline{B} \right]_{R_I - \delta r}^{R_I + \delta r} \quad (5.26)$$

The integrated conductivity tensor $\underline{\underline{\Sigma}}$ can be written in θ - ϕ coordinates as[60]:

$$\underline{\underline{\Sigma}} \equiv \begin{bmatrix} \frac{\Sigma_0 \Sigma_P}{\Sigma_0 \cos^2 \alpha + \Sigma_P \sin^2 \alpha} & \frac{-\Sigma_0 \Sigma_H}{\Sigma_0 \cos^2 \alpha + \Sigma_P \sin^2 \alpha} \\ \frac{\Sigma_0 \Sigma_H}{\Sigma_0 \cos^2 \alpha + \Sigma_P \sin^2 \alpha} & \Sigma_P + \frac{\Sigma_H^2 \sin^2 \alpha}{\Sigma_0 \cos^2 \alpha + \Sigma_P \sin^2 \alpha} \end{bmatrix} \quad (5.27)$$

Where α is the angle between the magnetic field and the vertical direction, given by $\cos \alpha \equiv \frac{-2 \cos \theta}{\sqrt{1+3 \cos^2 \theta}}$, and Σ_P , Σ_H , and Σ_0 are the height-integrated Pedersen, Hall, and parallel conductivities respectively. Their values are determined by integrating Kelley's[49] conductivity profiles from Earth's surface to the ionospheric boundary; values are shown in Table 5.2.

Table 5.2: Integrated Atmospheric Conductivity (S)

	Σ_0	Σ_P	Σ_H
Active Day	424	0.65	6.03
Quiet Day	284	0.44	4.02
Active Night	9	0.01	0.12
Quiet Night	9	0.01	0.12

An expression for the horizontal electric fields at the boundary can be obtained by inverting Equation (5.26). After mapping to covariant coordinates per Equation (5.8), and taking $\Sigma \equiv \det \underline{\underline{\Sigma}}$,

$$\begin{aligned} E_1 &\leftarrow \frac{1}{\mu_0 \Sigma} \lim_{\delta r \rightarrow 0} \left[-\Sigma_{\theta\phi} B_1 - \sqrt{\frac{g_{11}}{g_{22}}} \Sigma_{\phi\phi} B_2 \right]_{R_I-\delta r}^{R_I+\delta r} \\ E_2 &\leftarrow \frac{1}{\mu_0 \Sigma} \lim_{\delta r \rightarrow 0} \left[\sqrt{\frac{g_{22}}{g_{11}}} \Sigma_{\theta\theta} B_1 + \Sigma_{\phi\theta} B_2 \right]_{R_I-\delta r}^{R_I+\delta r} \end{aligned} \quad (5.28)$$

In order to compute the atmospheric magnetic field, a scalar magnetic potential (Ψ such that $\underline{B} = \nabla \Psi$) is computed as a linear combination of harmonics. The neutral atmosphere is considered to be a perfect insulator, giving $\nabla \times \underline{B} = 0$. Combined with $\nabla \cdot \underline{B} = 0$ (per Maxwell's equations), Ψ satisfies Laplace's equation, $\nabla^2 \Psi = 0$.

Laplace's equation can be solved analytically; however, a numerical solution is preferable to ensure orthonormality on a discrete and incomplete¹⁶ grid. After separating out the radial and azimuthal dependence in the usual way, the latitudinal component of Laplace's equation can be written in terms of $s \equiv -\sin^2 \theta$:

$$(4s^2 + 4s) \frac{d^2}{ds^2} Y_\ell + (4 + 6s) \frac{d}{ds} Y_\ell - \frac{m^2}{s} Y_\ell = \ell (\ell + 1) Y_\ell \quad (5.29)$$

Using centered differences to linearize the derivatives, Equation (5.29) becomes a system of coupled linear equations, one per field line. It can be solved numerically for eigenvalues $\ell (\ell + 1)$ and eigenfunctions Y_ℓ ¹⁷. In terms of the harmonics Y_ℓ , Ψ between the Earth's surface and the top of the atmosphere can be written using eigenweights a_ℓ and b_ℓ :

$$\Psi = \sum_\ell \left(a_\ell r^\ell + b_\ell r^{-\ell-1} \right) Y_\ell \quad (5.30)$$

¹⁶As discussed in Section 5.1, the grid is constrained to finite L , which excludes the equator as well as the poles.

¹⁷Solving Laplace's equation analytically results in spherical harmonics indexed by both ℓ and m , the separation constants for θ and ϕ respectively. In two and a half dimensions, ϕ is not explicitly resolved, so m is set manually.

As a boundary condition for Ψ , Earth is assumed to be a perfect conductor. This forces the magnetic field at Earth's surface to be horizontal; that is, $B_r = \frac{\partial}{\partial r} \Psi = 0$. Noting that solutions to Laplace's equation are orthonormal, each element of the sum in Equation (5.30) must be independently zero at R_E . This allows the coefficients a_ℓ and b_ℓ to be expressed in terms of one another.

$$b_\ell = \frac{\ell}{\ell + 1} R_E^{2\ell+1} a_\ell \quad (5.31)$$

The current sheet at the top of the atmosphere is assumed to be horizontal, so the radial component of the magnetic field must be the same just above and just below it. Taking the radial derivative of Equation (5.30) at the top of the atmosphere, and eliminating b_ℓ with Equation (5.31), gives

$$B_r = \sum_\ell \ell a_\ell R_I^{\ell-1} \left(1 - \lambda^{2\ell+1}\right) Y_\ell \quad \text{where} \quad \lambda \equiv \frac{R_E}{R_I} \sim 0.975 \quad (5.32)$$

The summation can be collapsed by “integrating” over a harmonic¹⁸. Inverse harmonics can be obtained by inverting the eigenvector matrix. Then $Y_\ell \cdot Y_{\ell'}^{-1} = \delta_{\ell\ell'}$ by construction.

$$a_\ell = \frac{1}{\ell R_I^{\ell-1}} \frac{B_r \cdot Y_\ell^{-1}}{1 - \lambda^{2\ell+1}} \quad (5.33)$$

Combining Equations (5.30), (5.31), and (5.33) allows the expression of Ψ at the top and bottom of the atmosphere as a linear combination of radial magnetic field components at the bottom of the ionosphere.

$$\begin{aligned} \Psi_E &= \sum_\ell Y_\ell \frac{R_I}{\ell (\ell - 1)} \frac{(2\ell - 1) \lambda^\ell}{1 - \lambda^{2\ell+1}} B_r \cdot Y_\ell^{-1} \\ \Psi_I &= \sum_\ell Y_\ell \frac{R_I}{\ell (\ell - 1)} \frac{(\ell - 1) + \ell \lambda^{2\ell+1}}{1 - \lambda^{2\ell+1}} B_r \cdot Y_\ell^{-1} \end{aligned} \quad (5.34)$$

¹⁸Because the functions are defined on a discrete grid, their inner product is not an integral, but a sum: $B_r \cdot Y_\ell^{-1} \equiv \sum_i B_r[i] Y_\ell^{-1}[i]$.

Horizontal magnetic fields are obtained by taking derivatives of Ψ .

$$B_1 = \frac{\partial}{\partial u^1} \Psi \quad B_2 = \frac{\partial}{\partial u^2} \Psi \quad (5.35)$$

Horizontal magnetic field values at the top of the atmosphere are used to impose boundary conditions on the electric fields at the bottom of the ionosphere, per Equation (5.28). Those at Earth's surface are valuable because they allow a direct comparison between model output and ground magnetometer data, after being mapped to physical coordinates per Equation (5.8).

Chapter 6

Electron Inertial Effects

As laid out in Chapter 5, Tuna resolves neither parallel currents nor parallel electric fields. This is unfortunate; parallel electric fields generated by kinetic and inertial Alfvén waves (including fundamental field line resonances[81, 97]) are a topic of particular interest in the study of auroral particle precipitation.

Parallel currents and electric fields can be added to Tuna through the consideration of electron inertial effects in Ohm's law:

$$0 = \sigma_0 E_z - J_z \quad \text{becomes} \quad \frac{1}{\nu} \frac{\partial}{\partial t} J_z = \sigma_0 E_z - J_z \quad (6.1)$$

With the addition of the electron inertial term, it is necessary to track the parallel current independent of the parallel electric field¹. Solving by integrating factors² gives

$$J_3 \leftarrow J_3 \exp(-\nu \delta t) + \delta t \frac{ne^2}{m_e} E_3 \exp\left(-\nu \frac{\delta t}{2}\right) \quad (6.2)$$

¹The parallel current J_z is defined on the same points of the Yee grid as E_z . It is offset in time by half of a time step.

²The integrating factors technique is laid out explicitly for Ampère's law in Section 5.4.

From there, the parallel electric field can be updated directly; Equation (5.23) is replaced by the following:

$$E_3 \leftarrow E_3 + c^2 \delta t (g_{31} F^1 + g_{33} F^3) - \frac{\delta t}{\epsilon_0} J_3 \quad (6.3)$$

The present section explores the complications that arise from the addition of the electron inertial term to Ohm's law, as well as a few results that may be gleaned despite those complications. Notably — for reasons discussed in Section 6.3 — the results presented in Chapter 7 do not make use of the electron inertial term.

6.1 The Boris Factor

With the addition of the electron inertial term, a cyclical dependence appears between Ampère's law and Ohm's law:

$$\frac{\partial}{\partial t} E_z \sim -\frac{1}{\epsilon_0} J_z \quad \text{and} \quad \frac{\partial}{\partial t} J_z \sim \frac{ne^2}{m_e} E_z \quad \text{so} \quad \frac{\partial^2}{\partial t^2} E_z \sim -\omega_P^2 E_z \quad (6.4)$$

That is, electron inertial effects come hand in hand with the plasma oscillation.

As mentioned in Chapter 4 and shown in Figure 6.1, plasma oscillation is quite fast — several orders of magnitude smaller than Tuna's time step as determined in Section 5.1 ($\sim 10 \mu s$). This poses a conundrum. At Tuna's usual time step, the plasma oscillation becomes unstable within seconds³. On the other hand, reducing the time step by three orders of magnitude to resolve the plasma oscillation is computationally infeasible; a run slated for an hour would require six weeks to complete.

As it happens, this problem can be solved by artificially increasing the parallel electric constant above its usual value of ϵ_0 . Doing so lowers both the speed of light and the plasma frequency within the simulation.

This technique — and others like it — has been widespread in numerical modeling since it was presented by Boris in 1970[6]. More recently, Lysak and Song considered its use

³For stability, $\omega_P \delta t < 1$ is necessary.

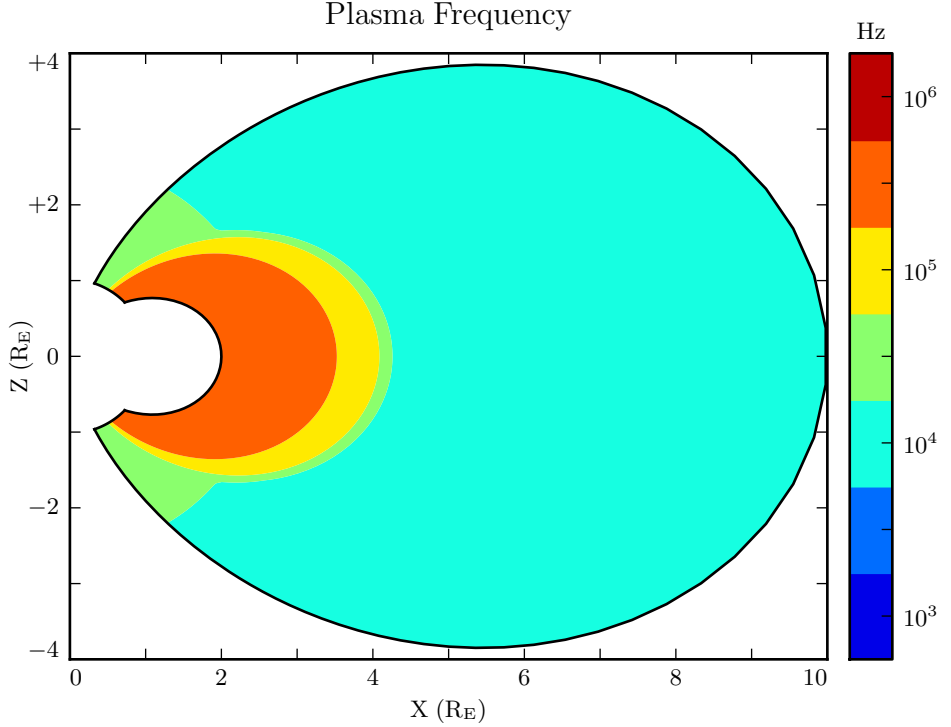


Figure 6.1: The plasma frequency reaches a peak value just under 10^6 Hz near the equator. Outside the plasmasphere, its value is closer to 10^4 Hz, which is still not well-resolved by Tuna's usual time step.

specifically for the case of electron inertial effects[62]. The following paraphrases their argument.

Supposing that the current and electric field are oscillating at frequency ω , the parallel components of Ampère's law and Ohm's law can be written

$$-i\omega\epsilon_0 E_z = \frac{1}{\mu_0} (\nabla \times \underline{B})_z - J_z \quad -\frac{i\omega}{\nu} J_z = \sigma_0 E_z - J_z \quad (6.5)$$

Then, eliminating the current, the parallel electric field can be related to the curl of the magnetic field by⁴

$$\left(1 - \frac{\omega^2 - i\nu\omega}{\omega_P^2}\right) E_z = \frac{c^2}{\omega_P^2} (\nu - i\omega) (\nabla \times \underline{B})_z \quad (6.6)$$

In Equation (6.6), $\frac{c}{\omega_P}$ is the electron inertial length. While the speed of light and the plasma frequency each depend on ϵ_0 , their ratio does not. This allows an estimation of how much the model should be affected by an artificially-large electric constant (and thus an artificially-small plasma frequency). So long as $\frac{\omega^2 - i\nu\omega}{\omega_P^2}$ remains small compared to unity, the model should behave faithfully.

For waves with periods of a minute or so, even perhaps-implausibly large Boris factors are allowed; for example, increasing ϵ_0 by a factor of 10^6 gives $\left|\frac{\omega^2 + i\omega\nu}{\omega_P^2}\right| \lesssim 0.01$.

6.2 Parallel Currents and Electric Fields

As discussed in Section 4.4, parallel electric fields in this regime are expected to be six or more orders of magnitude smaller than the perpendicular electric fields. Numerical results show general agreement: in Figure 6.2, the parallel electric field appears comparable to its perpendicular counterparts only after its been scaled up by six orders of magnitude.

As such, the inclusion of electron inertial effects does not appreciably impact the simulation's gross behavior; in Faraday's law, $\nabla \times \underline{E}$ is essentially unaffected. Side by side snapshots of the magnetic fields in runs carried out with and without electron inertial effects are not visibly distinguishable⁵ (not shown).

Even if there is no significant feedback through Faraday's law, it's informative to consider the structures that arise in parallel currents and electric fields driven by perturbations in the ring current. For example, the parallel electric field perturbation (with

⁴From Equation (4.4), $c^2 \equiv \frac{1}{\mu_0 \epsilon_0}$ and $\sigma_0 \equiv \frac{ne^2}{m_e \nu}$ and $\omega_P^2 \equiv \frac{ne^2}{m_e \epsilon_0}$.

⁵In a sense, this is reassuring. It ensures that the present section does not cast doubt on the results presented in Chapter 7, where electron inertial effects are neglected.

Electric Field Snapshots: Quiet Day, 10mHz Current, $m = 16$

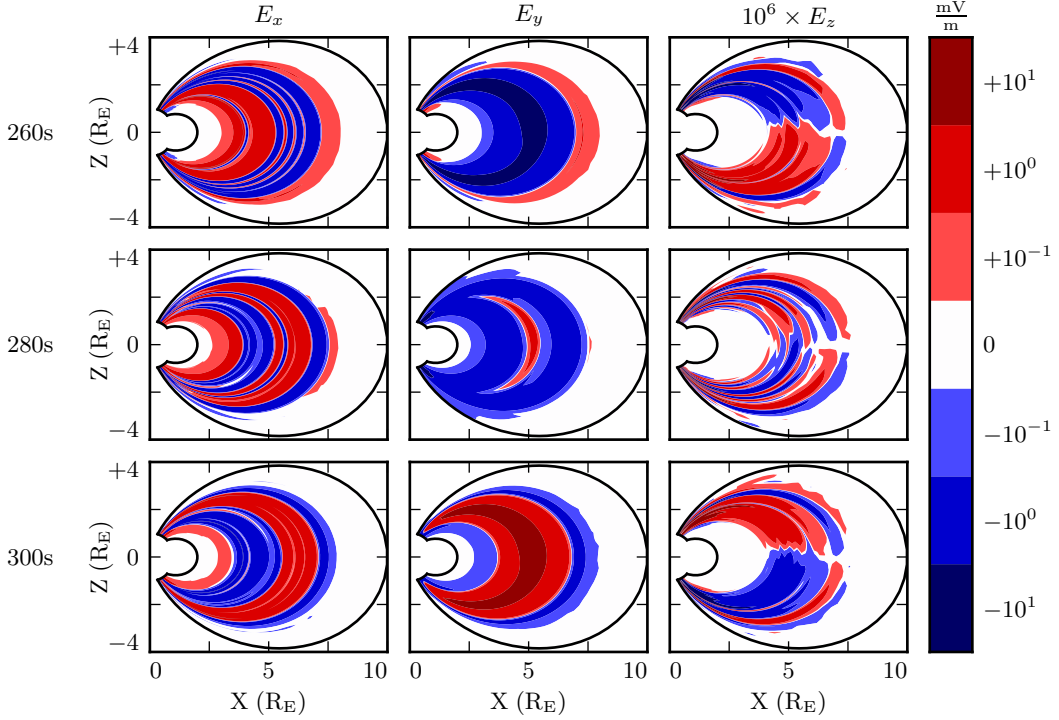


Figure 6.2: Parallel electric fields are smaller than perpendicular electric fields by about six orders of magnitude. As a result, parallel electric fields do not contribute significantly to $\nabla \times \underline{E}$ in Faraday's law.

maxima near the ionosphere) exhibits the opposite harmonic structure to the perpendicular electric field components (which peak near the equator). It is furthermore notable that the parallel electric field (and the parallel current that comes from it) exhibits real and imaginary components of comparable magnitude.

TODO: The compressional component of the magnetic field is also flipped compared to the perpendicular components. Should this have been mentioned in Chapter 3, with the figures showcasing harmonic structure?

At low altitude, where the Hall conductivity muddles all of the electric field components together, parallel currents coincide with strong Poynting flux. The imaginary component of the current lines up with the toroidal Poynting flux (which comes from imaginary E_x

Current and Poynting Flux at 100km: Quiet Day , 16mHz Current

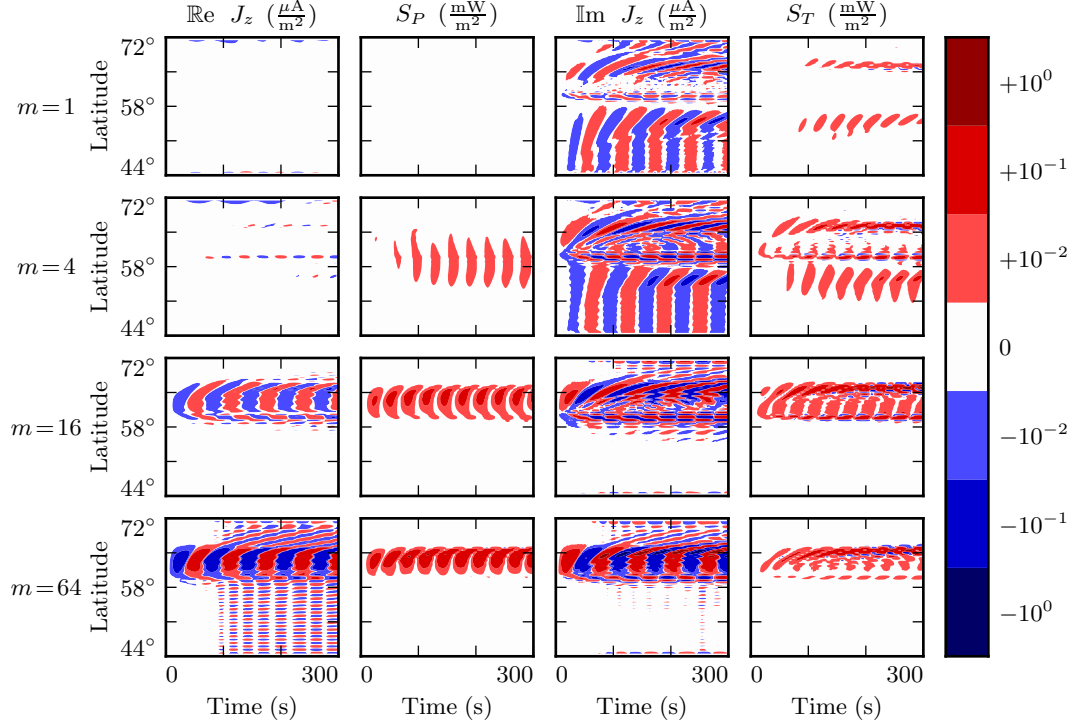


Figure 6.3: TODO: ...

and imaginary B_y^*), while the real current lines up with the poloidal Poynting flux (E_y and B_x^* are real)⁶. This is shown in Figure 6.3, which lays out the real and imaginary components of the parallel current (in the first and third column respectively) next to the poloidal and toroidal Poynting flux (second and fourth columns). Four runs are shown, one per row, with azimuthal modenumbers 1, 4, 16, and 64. Values are measured at an altitude of 100 km, the edge of the simulation.

Notably, the Poynting flux waveforms are rectified — they primarily carry energy Earthward. The current, on the other hand, alternates between upward and downward flow. This effect presumably arises because the current is a linear quantity while the Poynting

⁶As mentioned in Chapter 5, poloidal field components are in practice overwhelmingly real, indicating that they coincide azimuthally with the (real) driving. Toroidal components are overwhelmingly imaginary, which corresponds to an azimuthal offset.

flux is quadratic: the electric and magnetic fields that make it up oscillate in phase, so their product is positive even when they are negative.

At higher altitude, where the Hall conductivity is small, parallel current is associated only with the toroidal mode. Figure 6.4 shows data from the same runs as Figure 6.3, arranged in the same way, but the values are taken at an altitude of 1000 km instead of 100 km.

In Figure 6.4, as in Figure 6.3, the imaginary component of the parallel current (third column) coincides more or less with the toroidal Poynting flux (fourth column). However, the real component of the parallel current (first column) is vanishingly small, even when the poloidal Poynting flux (second column) is strong. TODO: Is this expected? Tikhonchuk[97] looks specifically at the toroidal mode when considering shear Alfvén waves. Does the poloidal mode count as compressional even when it's guided?

The magnitude of the parallel current tops out over $1 \mu\text{A}/\text{m}^2$, just shy of the up-to-tens of $\mu\text{A}/\text{m}^2$ inferred from ground observations and seen *in situ*[8, 47, 84].

It's also possible to consider the effect of parallel currents and electric fields on the ionosphere's energy budget, per Poynting's theorem:

$$\frac{\partial}{\partial t} u = -\nabla \cdot \underline{E} - \underline{J} \cdot \underline{E} \quad (6.7)$$

As shown in Figure 6.5, little energy transfer in the ionosphere is mediated by perpendicular components of the Poynting flux. The parallel component of $\underline{J} \cdot \underline{E}$ is comparably unimportant. The energy deposited in the ionosphere by the Poynting flux matches closely with the energy lost to Joule dissipation — as it should, to conserve energy — but according to the model, parallel currents and electric fields do not contribute significantly.

Current and Poynting Flux at 1000km: Quiet Day , 16mHz Current

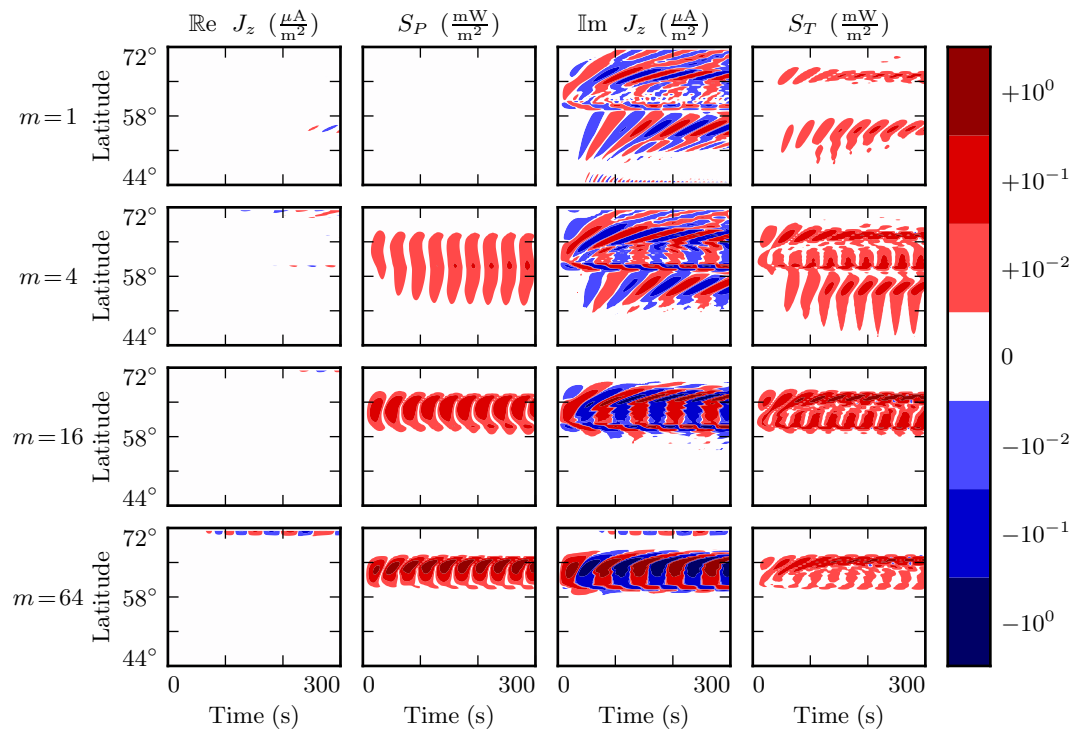


Figure 6.4: TODO: ...

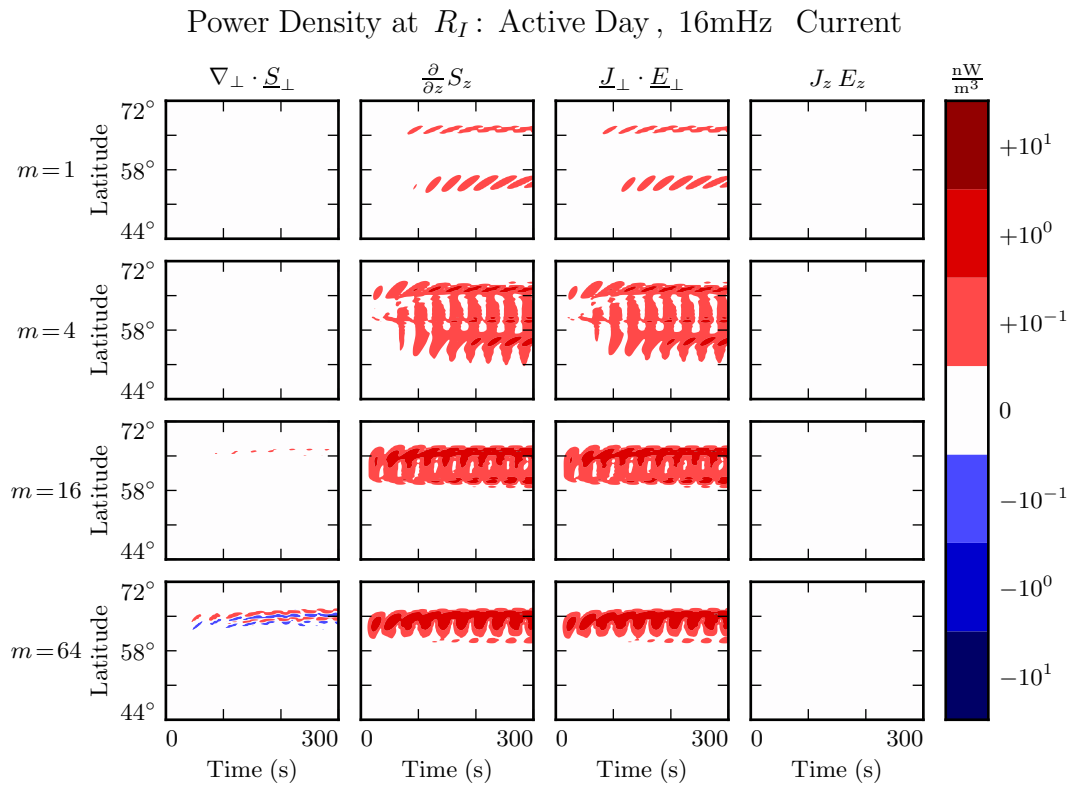


Figure 6.5: While field-aligned currents can be of significant size, they are not particularly good at depositing energy in the ionosphere. Energy deposited by the Poynting flux matches closely with Joule dissipation from the perpendicular currents, while $J_z E_z$ is smaller by several orders of magnitude.

6.3 Inertial Length Scales

It's not quite fair to compare the parallel and perpendicular contributions to $\nabla \times \underline{E}$ as is done in Section 6.2. Perpendicular electric fields are on the order of 1 mV/m, with wavelengths on the order of 10^5 km; they give rise to magnetic field gradients around 0.1 nT/s. Parallel electric fields, closer to 10^{-6} mV/m, would need to vary over length scales of 0.1 km to match with that.

Such scales are believable. The characteristic length scale of the plasma oscillation is the electron inertial length, $\frac{c}{\omega_p}$, which is on the order of 1 km in the auroral ionosphere and 0.1 km in the low-altitude plasmasphere. However, Tuna's usual grid doesn't resolve structures so fine; its resolution bottoms out closer to 10 km. That is, with the inclusion of electron inertial effects, Tuna's grid is too coarse to resolve all of the waves expected to be present. The model is prone to instability as a result.

Figure 6.6 shows a run with perpendicular resolution smaller than the electron inertial length, side by side with an analogous run on the usual grid. In order to carry out the inertial-scale run, several concessions were made to computational cost. The run simulates only a duration of 100 s (other results in previous sections and in Chapter 7 show 300 s), and the grid covers only the auroral latitudes from $L = 5$ to $L = 7$.

Even so, the run presents a significant computational expense. Spread over 16 cores, a 100 s run on Tuna's usual grid takes well under an hour. The inertial-scale run barely finished in 96 hours, the cutoff at the Minnesota Supercomputing Institute⁷.

The snapshot shown in Figure 6.6 uses a perpendicular grid resolution of 0.7 km at the Earthward edge, which just satisfies the Nyquist rate for the minimum inertial length of 1.7 km. It's still too coarse. There is clearly some small-scale structure developing in the ionosphere, but it's not well resolved. The large number of "wiggles" portends an imminent crash.

⁷Runtime goes as the inverse square of grid resolution. Not only does finer resolution require more grid cells, but it also gives rise to proportionally smaller crossing times, imposing a smaller time step.

Parallel Electric Fields: Quiet Day, 100s of 16mHz Current, $m = 16$

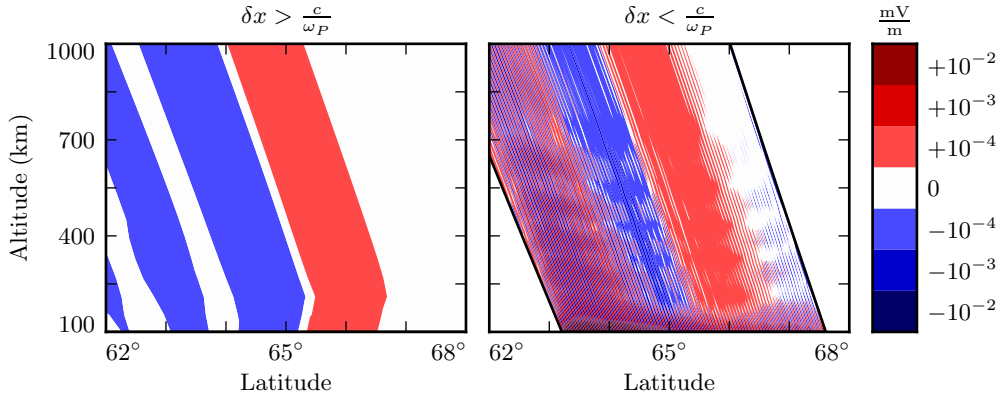


Figure 6.6: The parallel electric field develops significant structure when the perpendicular grid resolution is smaller than the electron inertial length. Unfortunately, such runs are prohibitively expensive. The lower panel — which still fails to resolve wave structure properly — represents a 100-fold increase in computational time.

6.4 Discussion

TODO: The dispersion relation in Chapter 4 suggests that parallel electric fields should be smaller than perpendicular electric fields by at least six orders of magnitude. Tuna agrees.

TODO: Tuna computes parallel currents a bit weaker than those that are observed — $\sim 1 \mu\text{A}/\text{m}^2$ rather than $\sim 10 \mu\text{A}/\text{m}^2$. The currents accompany the toroidal mode, but not the poloidal mode, except where the two are coupled by a strong Hall conductivity. Is this expected?

TODO: When inertial effects are not properly resolved, the code is prone to instability. Resolving inertial scales properly presents a prohibitive computational expense.

Electron inertial effects present a promising first-principles-based approach to the investigation of parallel currents and electric fields associated with field line resonances. Unfortunately, because of the large differences in scale between Pc4 pulsations and the

plasma oscillation, the proper deployment of inertial effects presents a prohibitive computational expense. Results shown in Chapter 7 make use of the core version of Tuna presented in Chapter 5, which does not include the effects of electron inertia.

Chapter 7

Numerical Results

In his 1974 paper, Radoski argues that a poloidally-polarized wave should asymptotically rotate to the toroidal polarization[80] as a result of the curved derivative in the meridional plane. The question of finite poloidal lifetimes is considered further in a 1995 paper by Mann and Wright[66]. Their numerical work used a straightened field line, with an Alfvén speed gradient in the “radial” direction. They also found a rotation over time from poloidal to toroidal polarization, with the characteristic time proportional to the azimuthal modenumber.

TODO: Ding et al[21] did similar work just before Mann and Wright, but results were less clear, possibly due to issues with grid resolution (as discussed in [66]).

TODO: Mann and Wright looked specifically at second harmonics. This work is on first harmonics. (In principle Tuna allows arbitrary driving waveforms and spatial distributions.)

The present chapter builds on the aforementioned results by relaxing several of their nonphysical assumptions. Tuna’s geometry (as described in Chapter 5) is far more realistic than Radoski’s half-cylinder or the box model used by Mann and Wright. Magnetic field lines are dipolar. Alfvén speed is based on an empirical profile, and varies along and across field lines. The present work also features driving delivered over time through perturbation of the ring current; past work has instead considered only the

evolution of an initial condition. Finally, the present model includes a height-resolved ionosphere (rather than perfectly-reflecting boundaries). The ionospheric conductivity provides a direct coupling between the poloidal and toroidal modes, in addition to dissipating energy.

Energy is computed per Poynting's theorem, with due consideration of the unusual geometry. Energy density is integrated over the meridional plane, but not in the azimuthal direction, giving units of gigajoules per radian; more than anything else, this serves as a reminder that the waves under consideration are azimuthally localized. The energy in the poloidal mode and the energy in the toroidal mode are, respectively,

$$U_P = \int \frac{du^1 du^3}{2\mu_0 \sqrt{g}} \left(B_x^2 + \frac{1}{v_A^2} E_y^2 \right) \quad U_T = \int \frac{du^1 du^3}{2\mu_0 \sqrt{g}} \left(B_y^2 + \frac{1}{v_A^2} E_x^2 \right) \quad (7.1)$$

TODO: We look at the interplay between poloidal-to-toroidal rotation, Joule dissipation, etc.

TODO: The overarching motivation for this work is that Pc4 pulsations vary in interesting ways with respect to azimuthal modenumber, and that prior models have been unable to give a good picture of that behavior.

TODO: It's possible that the contour plots (Sections 7.2 and 7.4) should go before the line plots (Sections 7.1 and 7.3). They sorta depend on one another. Unclear if there's a better way to divide things up.

7.1 Finite Poloidal Lifetimes: Dayside

Each subplot in Figures 7.1 and 7.2 is analogous to Figure 3 in Mann and Wright's paper[66]. Blue lines show the total energy in the poloidal mode as a function of time. Red lines show toroidal energy. Runs are organized such that driving frequency is constant down each column, and azimuthal modenumber is constant across each row. Axis bounds are held constant across all subplots.

The 28 runs shown in Figure 7.1 use a high-conductivity profile, corresponding to the dayside with low solar activity (shown in Section 5.2). The two dayside profiles —

active and quiet — are contrasted briefly in Section 7.5. However, the primary focus is on the difference between the dayside and the nightside. The differences between the two dayside profiles are minor in comparison.

The fact that red (toroidal) lines appear at all speaks to the coupling of the poloidal and toroidal modes. As discussed in Section 5.3, driving in Tuna is delivered purely into the poloidal electric field (reflecting the azimuthal direction of the ring current).

As expected, the rotation from poloidal to toroidal is slowest at large azimuthal mode-numbers. The toroidal energy overtakes the poloidal energy within a single drive period at $m = 4$; at $m = 64$, the most of the energy is in the poloidal mode for ~ 10 periods. However, the relationship between azimuthal modenumber and rotation timescale is not linear, as was suggested by Mann and Wright. Instead, the rotation is fastest at $m = 4$.

This hints at two competing effects, and there are only so many options. In addition to the poloidal-to-toroidal rotation, the two modes are coupled by the ionospheric Hall conductivity; energy is also lost when waves propagate out of the simulation domain, when driving interferes destructively with a wave, and as a result of Joule dissipation.

In practice, the Hall conductivity does not move large amounts of energy between the poloidal and toroidal modes. In fact, when the runs shown in Figure 7.1 are repeated with Hall conductivity uniformly zero (not shown), the energy curves do not change appreciably.

Joule dissipation — a recurring topic in the present chapter — is a major player in the simulation’s energy economy, but does not depend directly on the azimuthal modenumber. Similarly, azimuthal modenumber does not immediately impact the interference between a wave and its driver.

That leaves the propagation of energy across field lines, which does explain the observed behavior. As the azimuthal modenumber increases past order unity, compressional Alfvén waves in the Pc4 band become evanescent¹. Runs in the top two rows lose considerable sums of energy as a result of waves propagating out of the simulation

¹See Section 4.4.

domain. In contrast, runs conducted at higher modenumber do not permit the compressional propagation of Alfvén waves, so energy does not escape through the outer boundary.

Notably, the low-modenumber runs at 19 mHz do accumulate significant energy over time, while those at 13 mHz, 16 mHz, and 22 mHz falter. This response is likely non-physical, and is discussed in Section 7.2.

In each run, the energy of the system is asymptotically determined by the balance between the energy input (from driving) and the energy loss (through Joule dissipation in the ionosphere and escape through the boundary). When the driving frequency matches closely with the local Alfvén frequency, energy accumulates over a number of drive periods, leading to a relatively large asymptotic energy in the system.

The system’s resonant frequency (for a fundamental poloidal mode at $L \sim 5$) is affected significantly by the size of the plasmasphere. In Figure 7.1, with the plasmapause at $L_{PP} = 4$, the system resonates at 19 mHz at low m ; as m becomes large, the resonant frequency is closer to 22 mHz. Figure 7.2 shows the effect of moving the plasmapause to $L_{PP} = 5$: resonance is closer to 16 mHz. The runs are otherwise identical to those shown in Figure 7.1.

TODO: In most cases, the energy in the toroidal mode exceeds the energy in the poloidal mode.

TODO: The late, long dips in energy are probably due to “beats” in the interference between the driving frequency and the bounce frequency.

Poloidal (Blue) and Toroidal (Red) Energy: Quiet Day , $L_{PP} = 4$, $L_{drive} = 5$

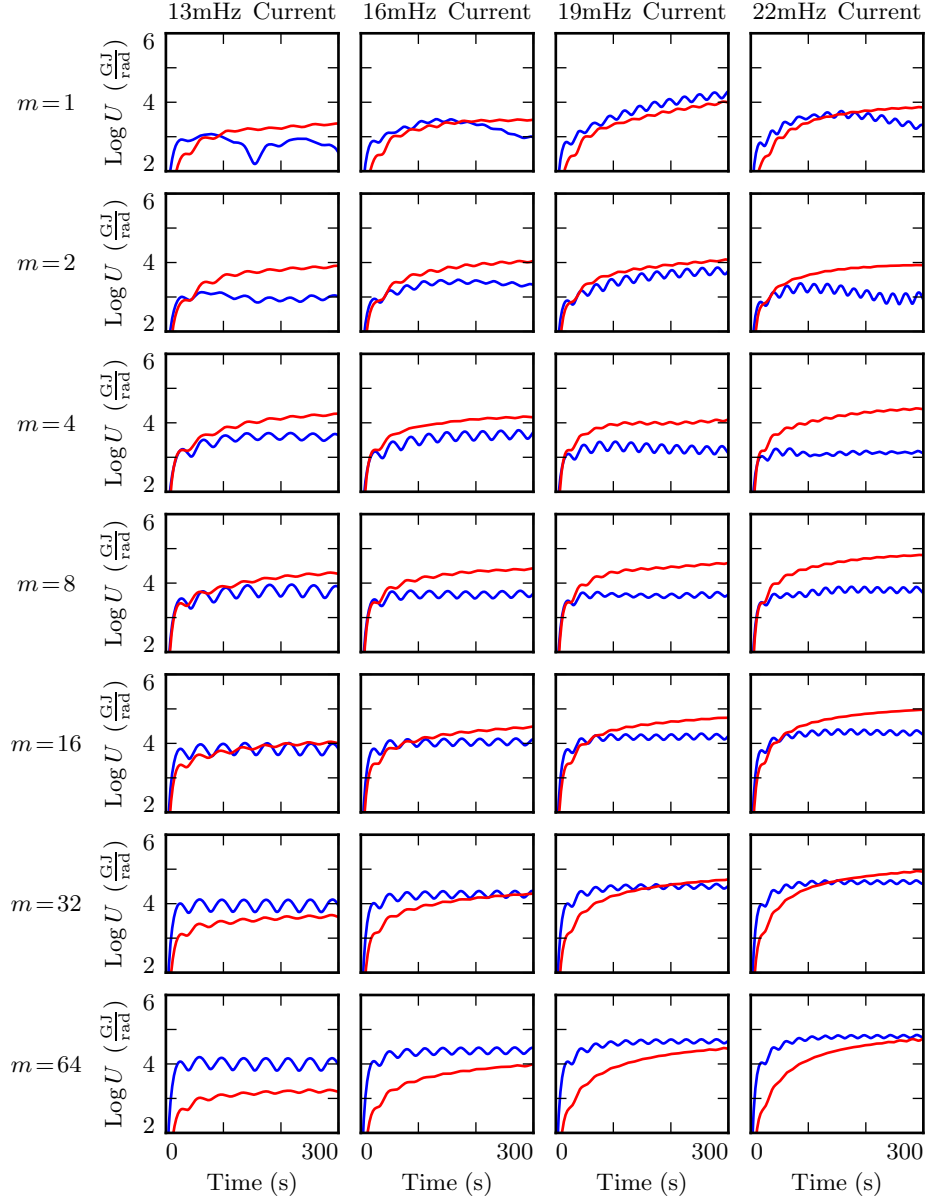


Figure 7.1: Each subplot above corresponds to a 300s run of Tuna. Driving is continuously injected into the poloidal mode (energy in blue). The waves rotate asymptotically to the toroidal mode (red). When the azimuthal modenumber (rows) is large, the rotation is slower. The driving frequency (columns) also affects the asymptotic accumulation of energy.

Poloidal (Blue) and Toroidal (Red) Energy: Quiet Day , $L_{PP} = 5$, $L_{drive} = 5$

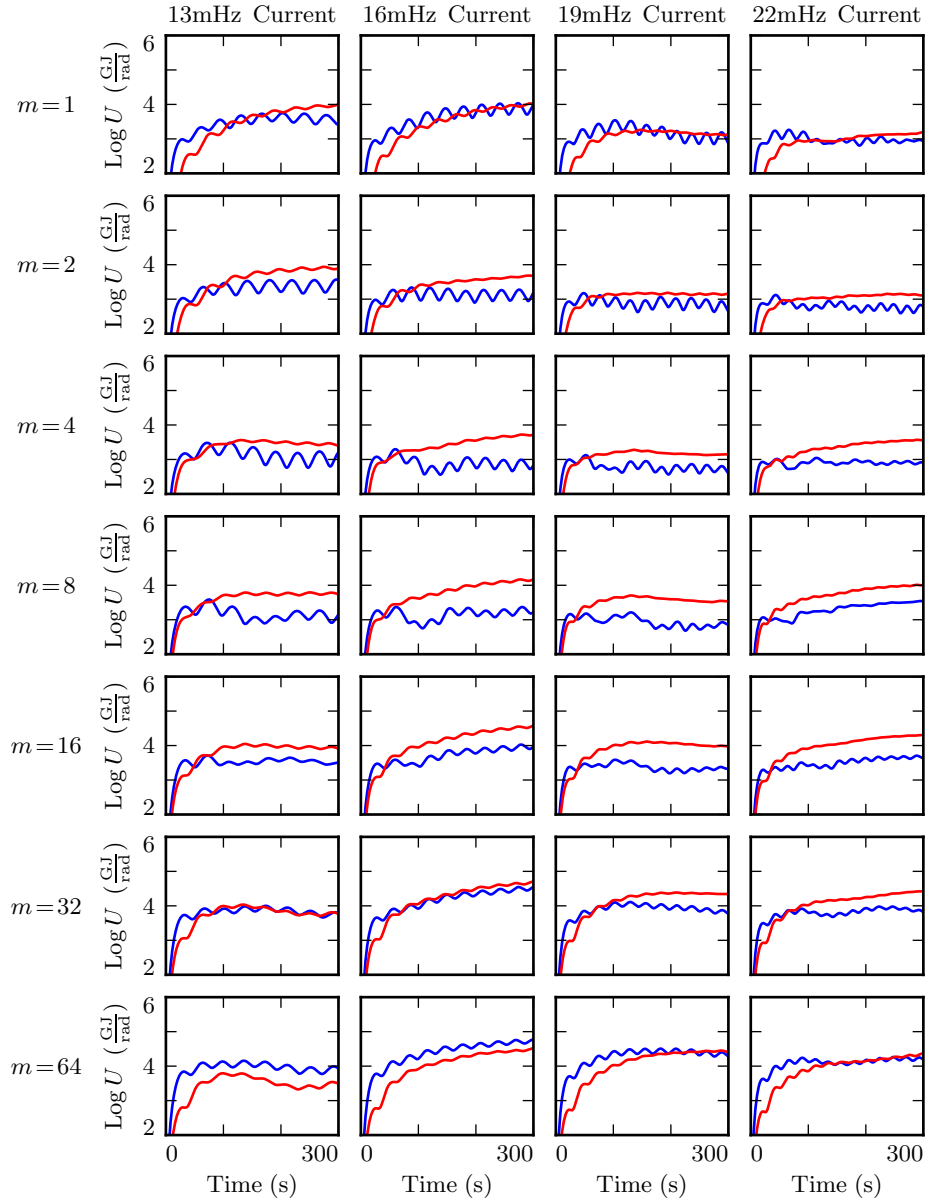


Figure 7.2: Above is a figure identical to Figure 7.1, except that the plasmapause has been moved from $L_{PP} = 4$ to $L_{PP} = 5$. This affects which driving frequency is closest to the resonant Alfvén frequency, and hence is most effective in causing a buildup of energy over time.

7.2 Spatial Distribution of Energy: Dayside

Looking a bit deeper, it's possible to comment on the structure of the poloidal and toroidal modes, not just their magnitudes. The subplots in Figures 7.3 to 7.5 are arranged analogously to those in Section 7.1: each comes from a different run, mode-number is held constant across each row, and frequency down each column.

Contours represent energy density, averaged over the volume of a flux tube. The vertical axis shows L -shell, while the horizontal axis is time. As above, poloidal and toroidal energy density are computed separately.

Figure 7.3 shows why, at low modenumber, the poloidal mode does not resonate well. Its compressional component allows energy to be spread broadly in L — in fact, at $m = 1$, no energy buildup at all is apparent at the location of the driving.

Some energy moves inward, and is trapped in the plasmapause's steep Alfvén speed gradient (particularly visible in the 16 mHz, $m = 4$ run). Some energy builds up in a third harmonic resonance near the outer boundary (shown best in runs with $m = 1$). The time spent propagating across field lines counts against the poloidal mode's finite lifetime — by the time a poloidally-polarized wave reaches the outer boundary, a significant fraction of its energy has rotated to the toroidal mode.

It's likely that at 19 mHz, with $m = 1$, the response is artificially amplified through interaction with the boundary conditions. As mentioned in Section 5.5, nonphysical reflections can occur when waves are very close to the boundary. In most cases, waves are not localized at the boundary, so this is not a concern.

The peak energy density in the bottom-right run (22 mHz driving, $m = 64$) is by far the largest of any run in Figure 7.3. The azimuthal modenumber is large, so the poloidal mode is purely guided; no time is wasted with movement across magnetic field lines. And, crucially, the frequency of the driving aligns closely with the resonant frequency where it's delivered. Other runs on the bottom row also have $m = 64$ (and so are also guided), but their driving frequencies do not align with the local resonant frequency. As a result, they do not accumulate energy over a large number of drive periods.

Similar behavior can be seen in Figure 7.4 (which shows the same runs as Figure 7.2, with the plasmapause moved to $L_{PP} = 5$ from its default location at $L_{PP} = 4$). A third harmonic resonance can be seen at the outer boundary for runs on the top row ($m = 1$). The effect of the plasmapause is particularly visible in the middle row, $m = 8$, where energy accumulates both just inside and just outside $L_{PP} = 5$. At high modenumber, the driving resonates best at 16 mHz; at other frequencies, energy density has a lower asymptotic value, which is reached more quickly.

In Figures 7.3 and 7.4, the poloidal contours show energy smeared across a swath of L -shells. On the other hand — as shown in Figure 7.5 — the toroidal mode appears only where the drive frequency matches the local eigenfrequency.

A horizontal line drawn through the Alfvén speed frequency profiles (recall Figure 3.1) intersects the profile up to three times: once as the Alfvén frequency drops through the Pc4 range from its low-latitude peak, again as the Alfvén frequency rises sharply at the plasmapause, and a third time as the Alfvén frequency drops asymptotically. Toroidal waves can be seen resonating at all three of these locations in the $m = 4, 19$ mHz run in Figure 7.5, along with a third harmonic at large L .

This is consistent with observations: toroidal resonances are noted for having frequencies which depend strongly on L , in contrast to the poloidal mode's less-strict relationship between frequency and location.

The dayside poloidal modes shown in Figures 7.3 and 7.4 attain an energy density on the order of 10^{-1} nJ/m³ only under ideal conditions: high modenumber runs with driving close to the local Alfvén frequency. Between the 56 dayside runs shown, such energy density appears only twice. On the other hand, the toroidal mode reaches $\sim 10^{-1}$ nJ/m³ in six of the runs in Figure 7.5 alone. That is, the poloidal mode only exhibits a high energy density on the dayside only when conditions are ideal; the toroidal mode isn't nearly so particular.

Poloidal Energy Density by L-Shell: Quiet Day , $L_{PP} = 4$, $L_{drive} = 5$

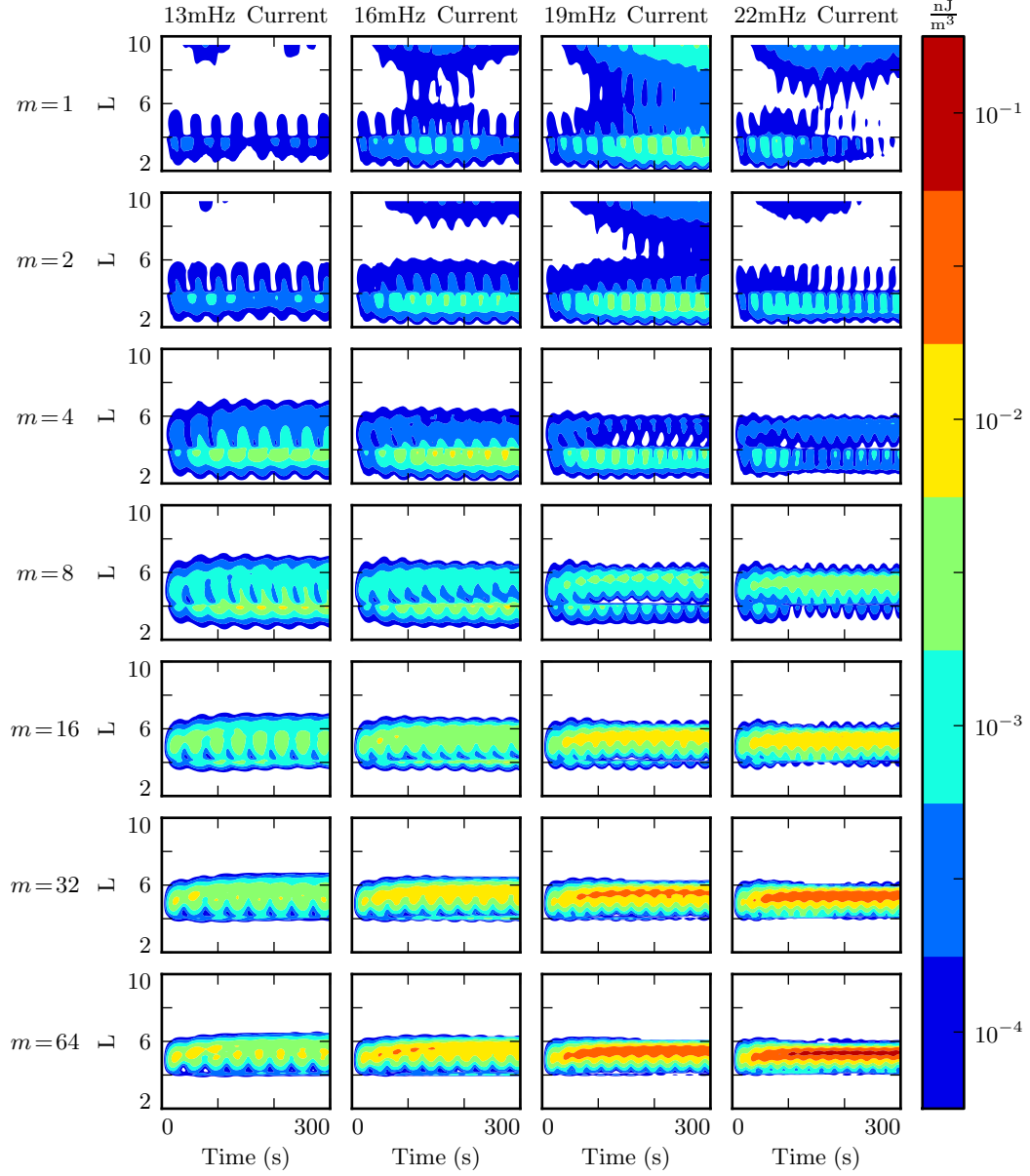


Figure 7.3: Each subplot above corresponds to a 300s run of Tuna, driven in the poloidal mode. At low m , energy instead moves radially and rotates quickly to the toroidal mode, precluding the formation of poloidal FLRs. At high m , the poloidal mode is guided, and the mode rotation is slow, allowing a strong resonance — but only when the driving frequency matches the local Alfvén frequency.

Poloidal Energy Density by L-Shell: Quiet Day , $L_{PP} = 5$, $L_{drive} = 5$

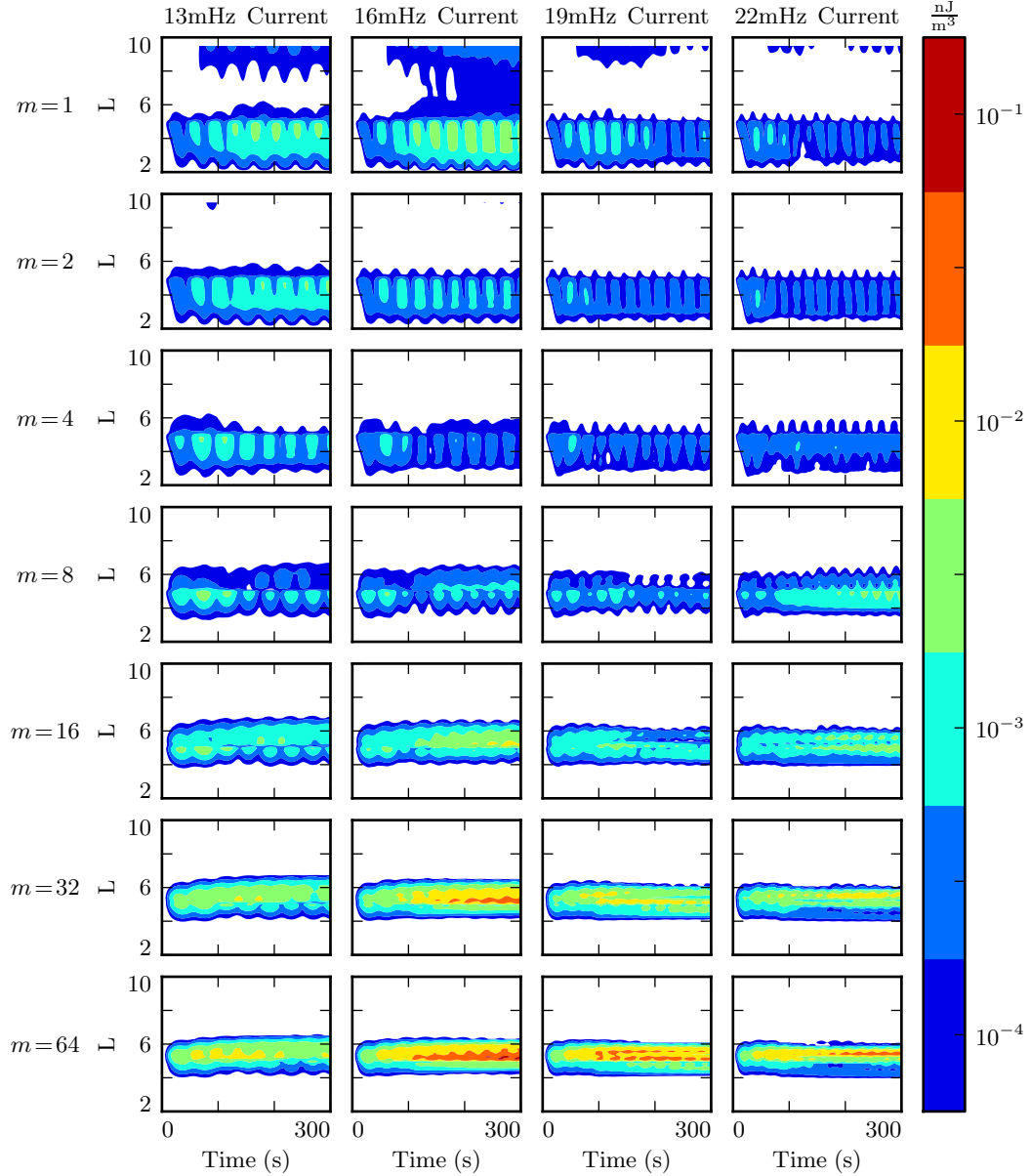


Figure 7.4: The Alfvén frequency profile is significantly affected by the size of the plasmasphere. The runs shown above are identical to those in Figure 7.3, except that the plasmapause has been moved from $L_{PP} = 4$ to $L_{PP} = 5$. As a result, the most effective resonance at $L \sim 5$ is shifted from 22 mHz to 16 mHz.

Toroidal Energy Density by L-Shell: Quiet Day , $L_{PP} = 4$, $L_{drive} = 5$

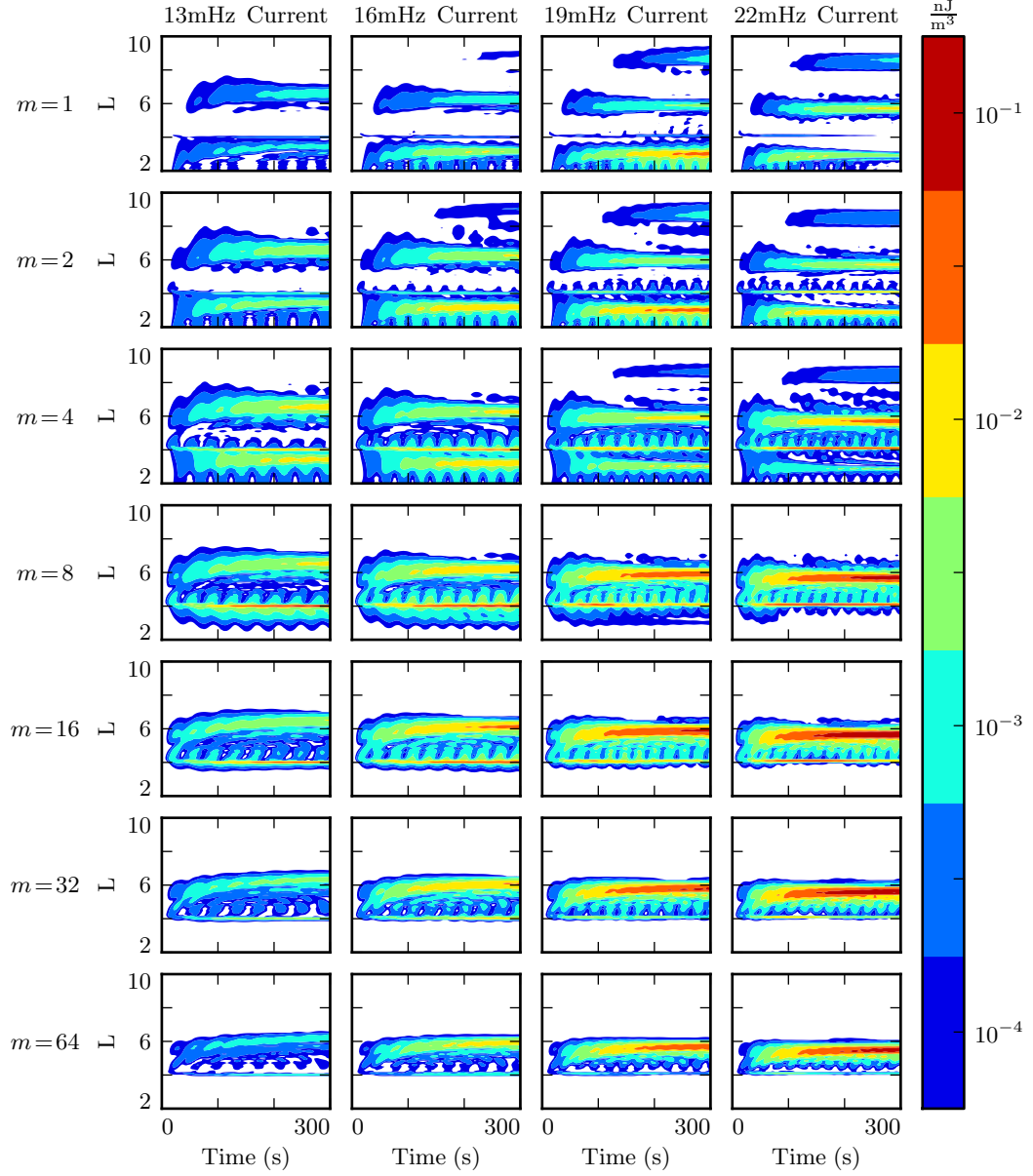


Figure 7.5: On the dayside, energy accumulates in the toroidal mode only at L values where the drive frequency matches a local eigenfrequency. This is in contrast to the more smeared appearance of the poloidal contours shown in Figures 7.3 and 7.4. Furthermore, the toroidal mode attains a high energy density under more diverse conditions than the poloidal mode.

7.3 Finite Poloidal Lifetimes: Nightside

Compared to the dayside ionosphere employed in Section 7.1, the nightside profiles exhibit two major differences. The ionospheric conductivity is lower, and the Alfvén speed is higher. The present section and Section 7.4 show results using only the active nightside profile. The differences between the quiet and active nightside ionospheric profiles are small compared to the differences between either dayside profile and either nightside profile; all four profiles are briefly compared in Section 7.5.

The low conductivity on the nightside gives rise to strong Joule dissipation. Waves are damped out in just a few bounces, so asymptotic energy values are reached quickly. Even so, the poloidal-to-toroidal rotation is qualitatively the same as on the dayside. The further the azimuthal modenumber from the rotation peak at $m = 4$, the lower the asymptotic toroidal energy level is compared to the poloidal. If anything, the effect is exaggerated by the small dissipation timescale. When $m = 64$, no more than $\sim 10\%$ of the energy in the poloidal mode rotates to the toroidal mode before being lost.

Figure 7.6 is arranged analogously to the figures in Section 7.1: each subplot is an independent run, drive frequency is constant down each column, and azimuthal modenumber is constant across each row. Poloidal energy is blue; toroidal energy is red.

The lower energies in Figure 7.6 (compared to Figure 7.1, the analogous dayside runs) are not entirely due to increased Joule dissipation. Due to the difference in electric constant between the dayside and nightside magnetospheres², resonant frequencies just outside the typical ($L_{PP} = 4$) plasmapause fall well outside the $Pc4$ range. None of the frequencies shown in Figure 7.6, when delivered at $L_{drive} = 5$, align with the local eigenfrequency.

As in Section 7.1, the 19 mHz run with $m = 1$ is an apparent exception. A large amount of energy builds up in a third harmonic very close to the outer boundary. The interaction is likely nonphysical.

TODO: It may be significant that $\int \sigma dz$ is constant across all L -shells, but $\int \frac{\sigma}{v_A^2} dz$ is not.

²See Figure 3.1.

Behavior closer to resonance is shown in Figure 7.7. The plasmapause remains at $L_{PP} = 4$, but the driving is moved out to $L_{drive} = 6$, at which point the local Alfvén frequency overlaps the Pc4 frequency band.

There is surprisingly little difference between Figures 7.6 and 7.7 (the subplots of which are arranged analogously). Asymptotic energy levels vary — in the case of high m and low frequency, runs in Figure 7.7 are more energetic by an order of magnitude or more — but the qualitative behavior is the same. Driving is balanced by dissipation over the course of just a few drive periods. Dissipation outstrips poloidal-to-toroidal rotation in the case of large azimuthal modenumber. And, unlike on the dayside, the toroidal mode typically does not match the asymptotic energy level seen in the poloidal mode.

Poloidal (Blue) and Toroidal (Red) Energy: Active Night , $L_{PP} = 4$, $L_{drive} = 5$

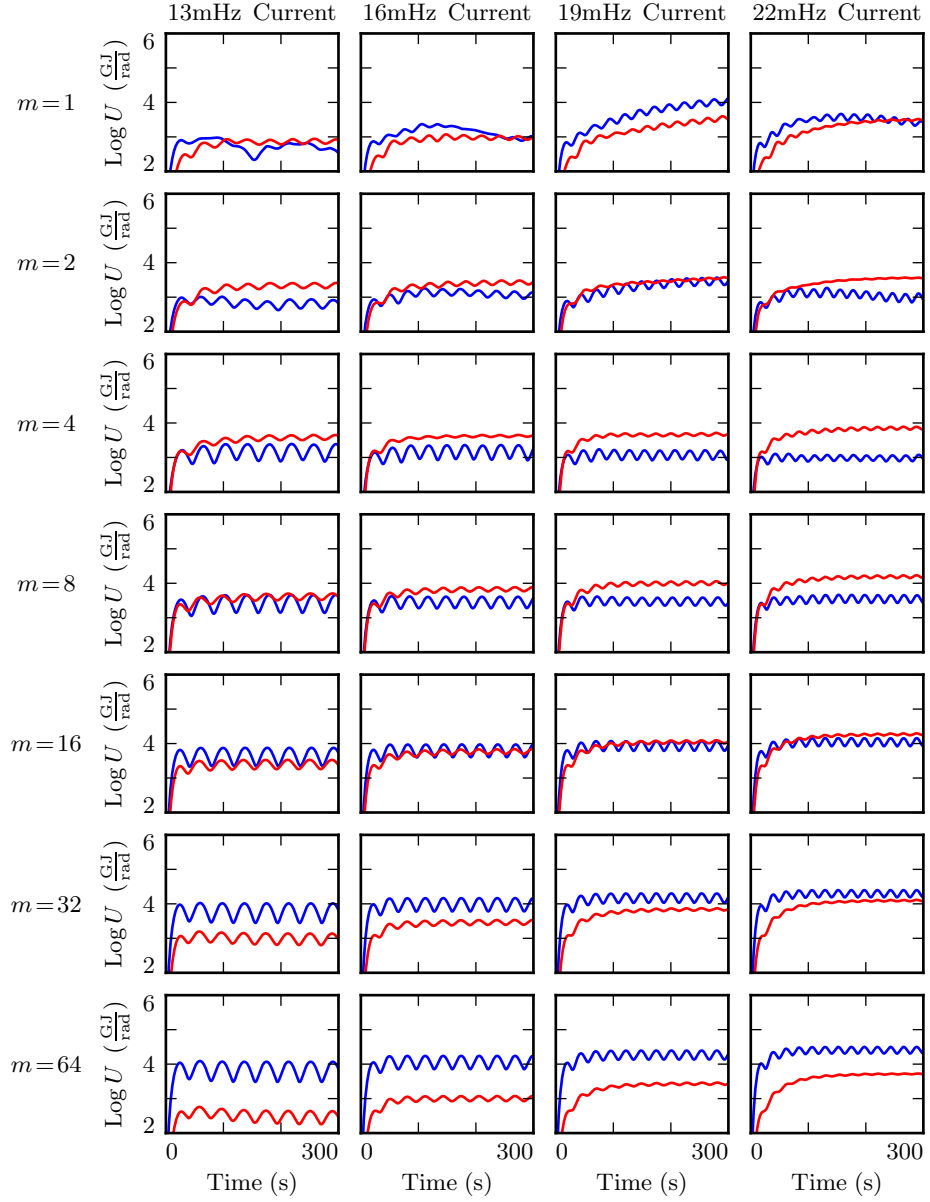


Figure 7.6: On the nightside, driving in the $\text{Pc}4$ band is not resonant at $L \sim 5$. This — combined with the lower ionospheric conductivity — causes the poloidal (blue) and toroidal (red) energies to quickly reach their asymptotic values. As on the dayside, energy rotates from poloidal to toroidal most effectively at small-but-finite m .

Poloidal (Blue) and Toroidal (Red) Energy: Active Night , $L_{PP} = 4$, $L_{drive} = 6$

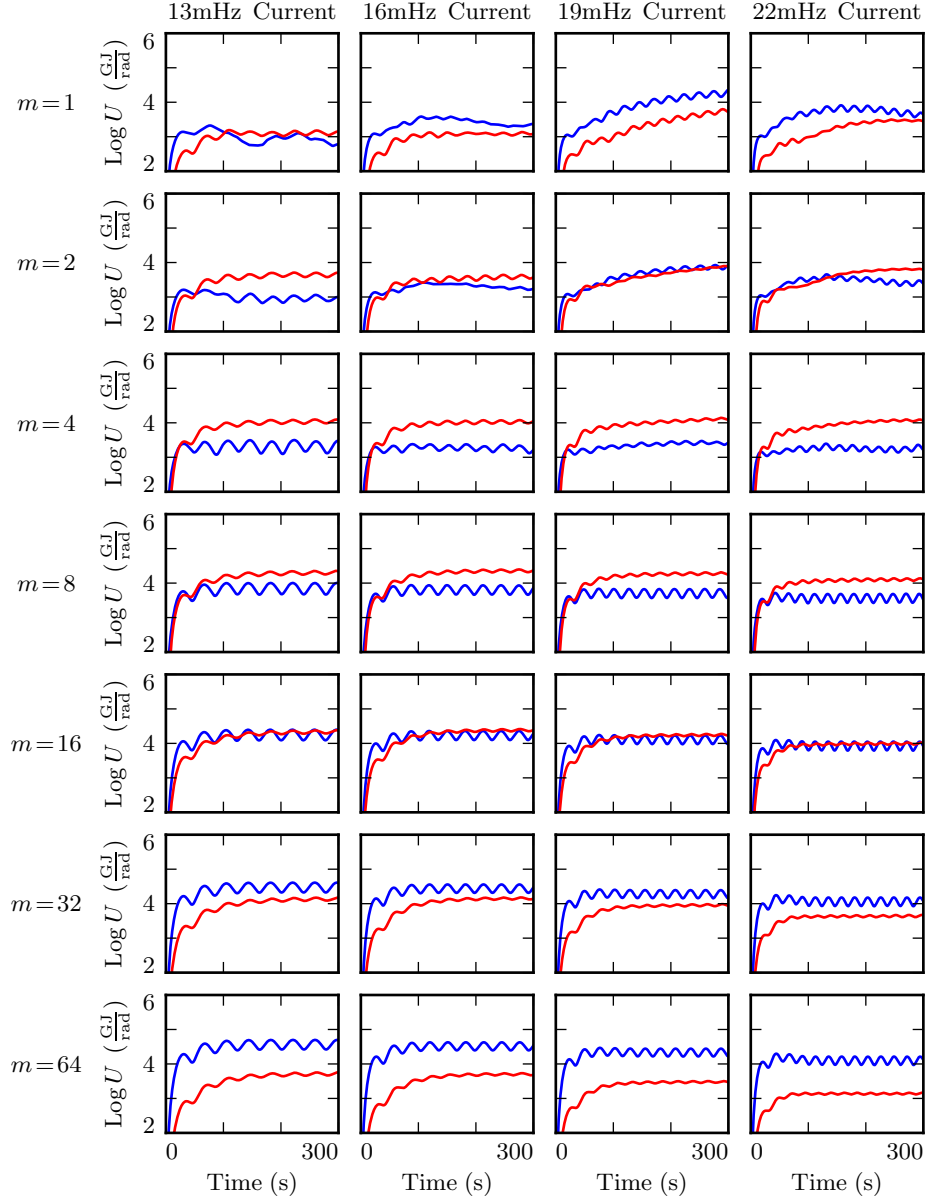


Figure 7.7: Even when the drive frequency does line up with the local Alfvén frequency, the low ionospheric conductivity prevents the accumulation of energy over the course of a large number of drive periods. Asymptotic energies are higher above than in analogous runs shown in Figure 7.6 — but compared to the dayside, the asymptotic energies are still small, and are still reached quickly.

7.4 Spatial Distribution of Energy: Nightside

Figure 7.8 shows the radial distribution of poloidal energy on the nightside — a slice of each run shown in Figure 7.7. Broadly speaking, the behavior is consistent with that seen in Section 7.2: energy is smeared across L -shells at small m and guided at high m , with particularly strong energy buildup when the drive frequency matches the local Alfvén frequency.

As discussed in Section 7.3, the nightside’s relatively low ionospheric conductivity increases the rate of dissipation. Asymptotic energy content is reached quickly, and is small compared to that seen in analogous dayside runs.

The effect is particularly pronounced at large modenumber, where the poloidal-to-toroidal rotation timescale is slower than the nightside dissipation timescale. In most of the dayside runs shown in Section 7.2, the toroidal mode asymptotically exceeds the poloidal mode both in terms of total energy content and in terms of peak energy density. On the nightside, the opposite is true. At high modenumber, the asymptotic rotation from the poloidal mode to the toroidal mode doesn’t occur until most of the energy has been lost to Joule dissipation. Peak poloidal energy densities at $m = 64$ exceed their toroidal counterparts — shown in Figure 7.9 — by an order of magnitude.

TODO: On the nightside, unlike the dayside, toroidal contours are messy. Why?

Poloidal Energy Density by L-Shell: Active Night , $L_{PP} = 4$, $L_{drive} = 6$

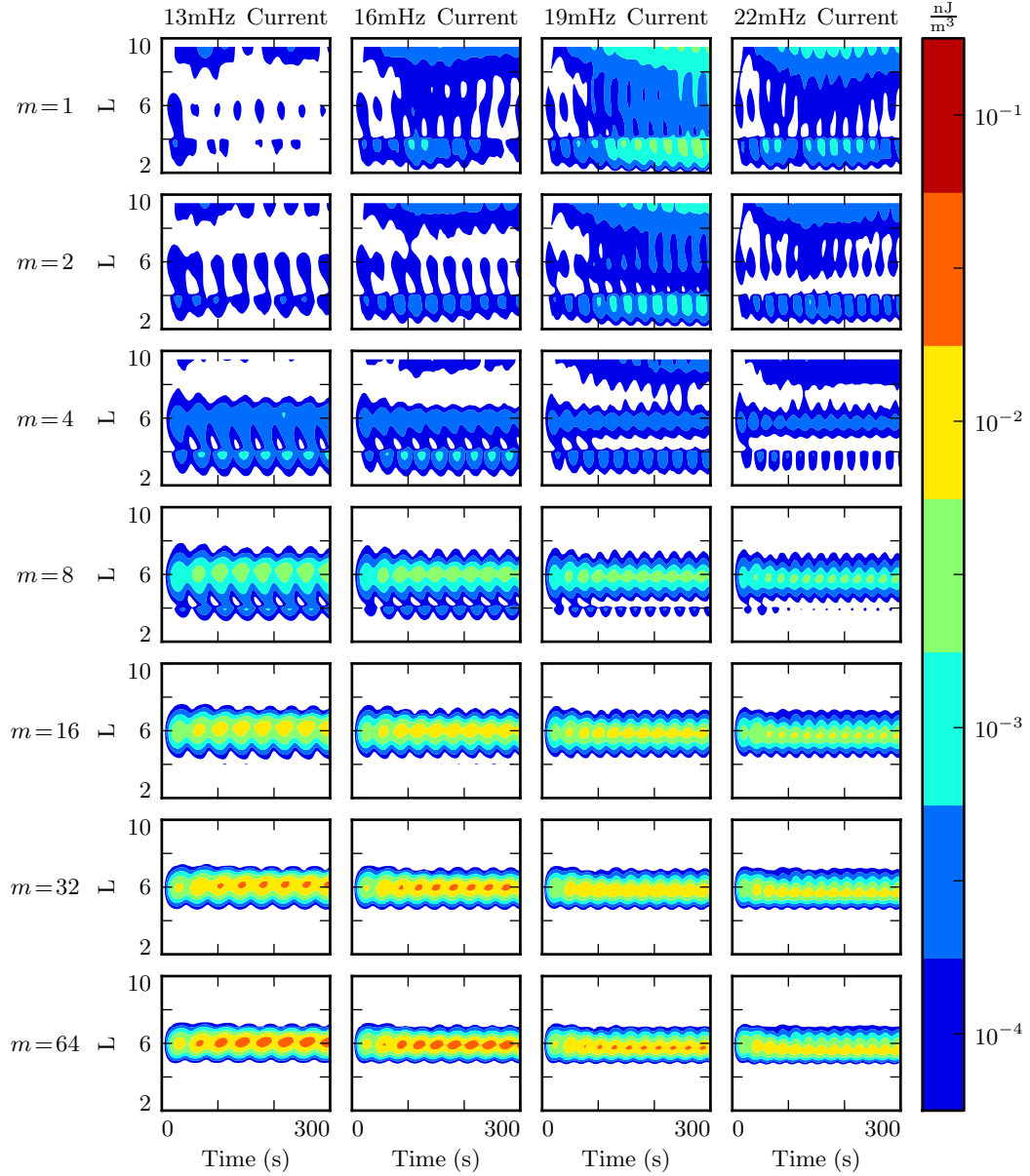


Figure 7.8: The behavior of the poloidal mode on the nightside matches qualitatively with the behavior on the dayside. At low m , energy is lost to the outer boundary. At high m , resonance occurs, but only if the drive frequency is close to the local eigenfrequency. The big difference is that, due to the increased dissipation in the ionosphere, asymptotic energy densities are relatively low, and reached relatively quickly.

Toroidal Energy Density by L-Shell: Active Night , $L_{PP} = 4$, $L_{drive} = 6$

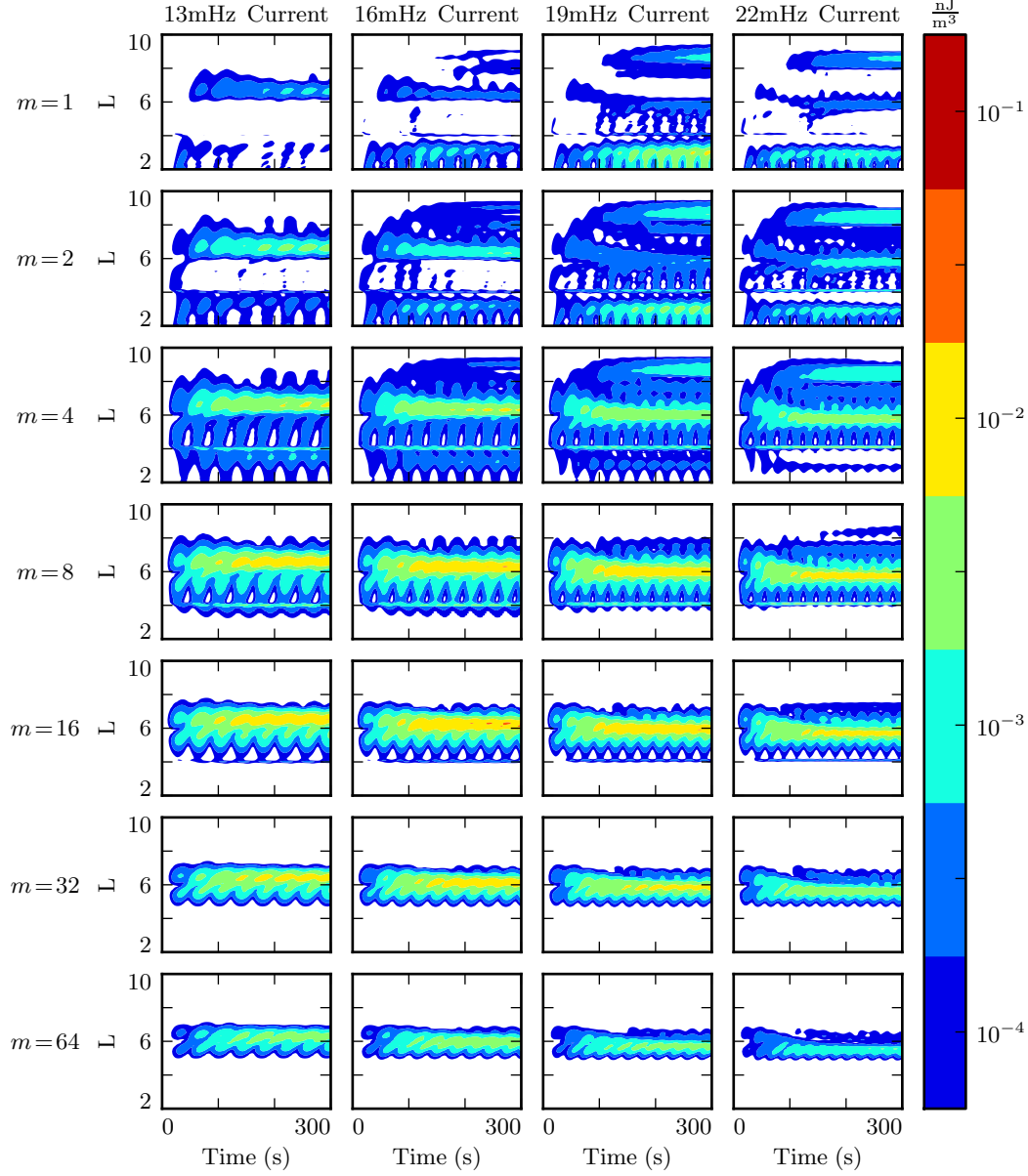


Figure 7.9: In low- m runs, the poloidal mode loses energy to the outer boundary, which impairs the growth of the toroidal mode. At high m , poloidal-to-toroidal rotation is slow compared to dissipative timescales on the nightside. The strongest toroidal waves — which are still weak compared to those on the dayside — thus appear at moderate m .

7.5 Ground Signatures and Giant Pulsations

While the majority of the action is in space, the majority of FLR observations have been ground-based. The present section explores the same simulations discussed in Sections 7.1 to 7.4, but in terms of their ground signatures rather than their broad energy distributions.

As in the figures shown in Sections 7.1 to 7.4, each row in Figures 7.10 and 7.11 shows runs at a different modenumber. The columns are magnetic field contours; the vertical axis is latitude, and the horizontal axis is time. The four columns are components of the magnetic field signatures at the ground: the north-south magnetic field (first and third columns) and the east-west magnetic field (second and fourth columns). The pair on the left show a simulation carried out using the active ionospheric profile, and the pair on the right show a simulation using the quiet profile.

Notably, the magnetic polarization of a low frequency Alfvén wave is rotated by $\sim 90^\circ$ as it passes through the ionosphere[42]. The east-west field on the ground (B_ϕ) corresponds to the poloidal polarization in space, and the north-south field on the ground (B_θ) corresponds to the toroidal mode.

TODO: What's going on with the empty frame for nightside, $m = 1, 16\text{ mHz}$?

TODO: Don't use 19 mHz! It's wonky at low modenumber. Use 22 mHz instead.

The most striking feature of Figures 7.10 and 7.11 is the modenumber dependence. As modenumber increases, the magnetic field signatures become sharply localized in latitude. At high m , ground signatures are concentrated between 60° and 70° , peaking just below 65° . This shows good agreement with observations of Pgs peaked near 66° .

At low modenumber, magnetic signatures are weak on the ground because the waves in space are also weak. At high modenumber, waves in space are strong, but so is the attenuation of magnetic signatures by the ionosphere³. The “sweet spot” at which magnetic ground signatures are maximized falls at $m = 16$ to $m = 32$. For comparison, Pgs are generally observed with azimuthal modenumbers of 16 to 35[94].

³See Equation (3.2).

Ground signatures are maximized at $m = 16$ and $m = 32$ on both the dayside (Figure 7.10) and the nightside (Figure 7.11). Dayside signatures are stronger than those on the nightside, and quiet dayside and quiet nightside responses are stronger than those on the active dayside and active nightside respectively. The strongest magnetic fields at the ground are primarily east-west polarized – as Pgs are[94].

TODO: At present, Tuna's ionospheric profiles do not allow the dawn and dusk flanks to be distinguished from the dayside and nightside.

Magnetic Ground Signatures: 19mHz Current , $L_{PP} = 4$, $L_{drive} = 5$

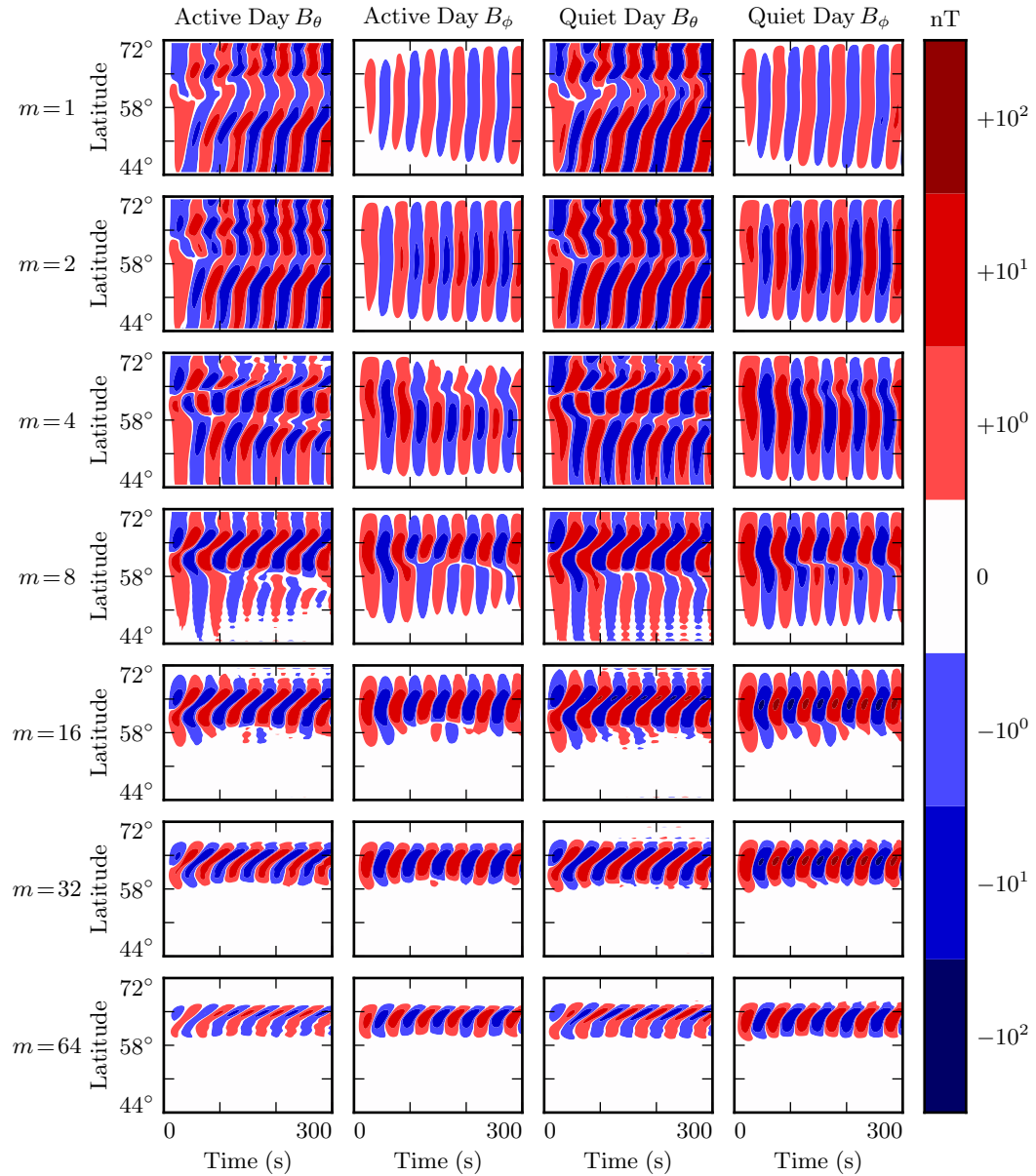


Figure 7.10: TODO: Use 22 mHz instead! At 19 mHz and low m , there's something weird happening at the outer boundary.

Magnetic Ground Signatures: 16mHz Current , $L_{PP} = 4$, $L_{drive} = 5$

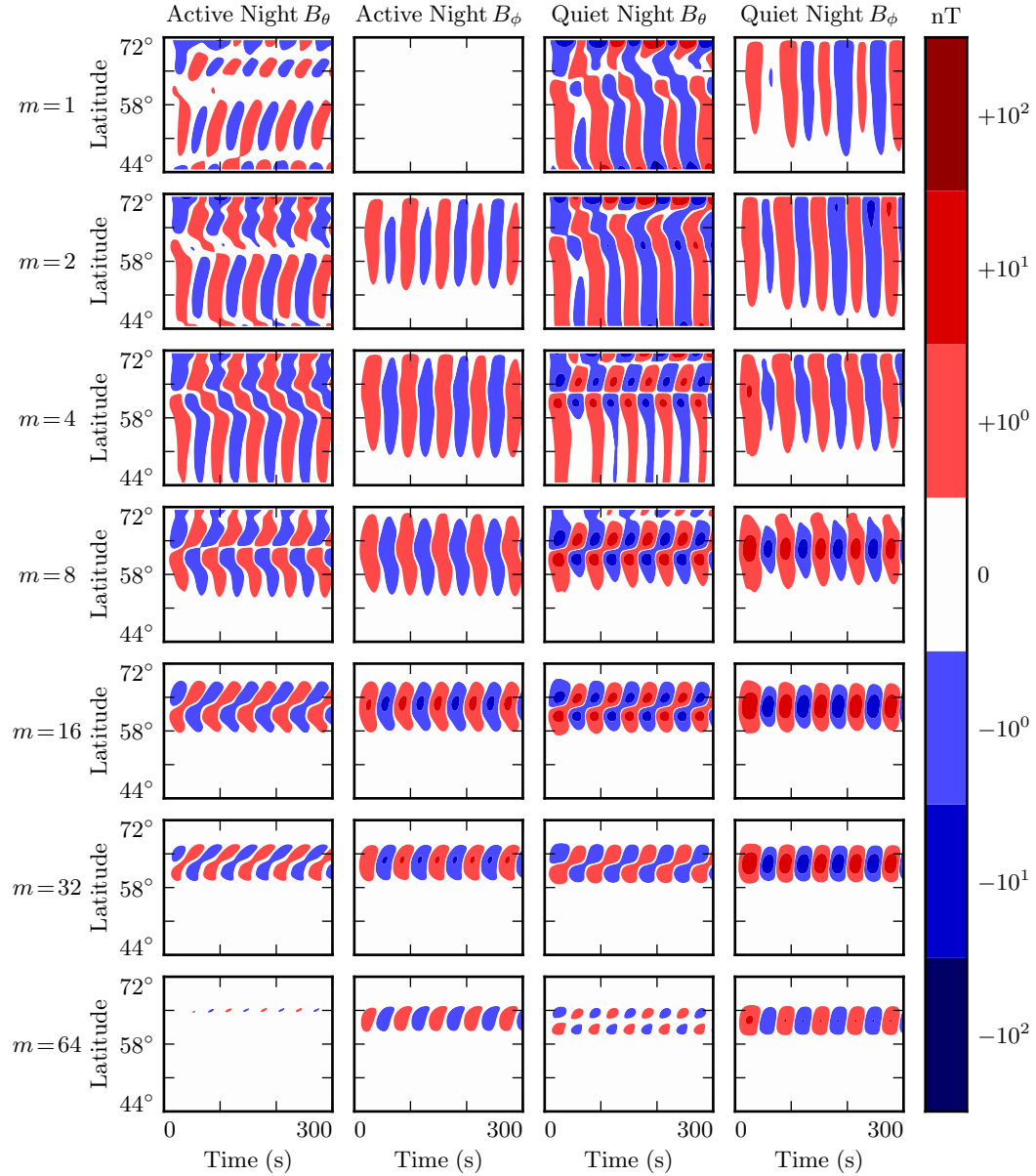


Figure 7.11: Nightside ground signatures are less strongly peaked than those on the dayside, but qualitative features are the same: the strongest signals are in B_ϕ , peaked over just a few degrees in latitude, at a modenumber of 16 or 32, under quiet ionospheric conditions.

7.6 Discussion

TODO: Make this section read nicely.

Poloidal FLRs rotate to the toroidal mode over time. Toroidal modes do not appear to rotate back to the poloidal mode. When m is small, the rotation is comparable to an oscillation period; when m is large, rotation timescales are comparable to ten periods, sometimes more.

On the dayside, little damping takes place over rotation timescales, so the toroidal mode asymptotically exceeds the poloidal mode. The exception is waves with low modenumber, where poloidal waves can escape by propagating across field lines. An evaluation of what happens then — whether they bounce back off the magnetopause, for example — is beyond the scope of the present work.

On the nightside, the conductivity of the ionosphere is low enough that damping timescales become comparable to oscillation timescales. Waves are weaker, since they are unable to accumulate energy over as many periods. High- m toroidal waves are particularly weak, since the dissipation timescale is faster than the poloidal-to-toroidal rotation timescale.

Waves resonate best when the frequency of the driving matches the local eigenfrequency where it's delivered. The eigenfrequency is significantly affected by the size of the plasmasphere.

The poloidal mode, due to its compressional character, exhibits an energy profile which is smeared in L . The toroidal mode, on the other hand, forms sharp resonances where the drive frequency matches the local eigenfrequency. This may explain why the observed frequencies of poloidal waves depend weakly on L , while the frequencies of toroidal waves are strongly dependent on L .

At low m , ground signatures are weak because waves in space are weak because energy can easily escape through the simulation's outer boundary. At large m , ground signatures are attenuated by the ionosphere. The “sweet spot” in azimuthal modenumber at which ground signatures are strongest is around 16 to 32. Furthermore, ground signatures are strongest when ionospheric profiles corresponding to solar minimum are used.

Driving in the poloidal electric field gives rise to primarily ground signatures polarized primarily in the east-west direction at the ground. And, when the frequency of the driving does not match the local eigenfrequency, the high- m resonates weakly in place, rather than tunneling across field lines to resonate strongly somewhere else.

These findings imply, awkwardly, that the morphology of giant pulsations may reveal relatively little about their origins. One can consider a hypothetical magnetosphere subject to constant driving: broadband in frequency, broadband in modenumber, just outside the plasmapause. Low- m poloidal waves will quickly rotate to the toroidal mode (and/or propagate away). High- m waves will resonate in place, accumulating energy over time, and giving rise to “multiharmonic toroidal waves”[91]; Fourier components that do not match the local eigenfrequency will quickly asymptote. Waves with very high modenumbers will be attenuated by the ionosphere. The response on the ground will be significantly stronger during quiet solar conditions. In other words, the measurements on the ground will look very much like a giant pulsation.

TODO: Notably, the present work offers no explanation as to Pgs’ distinctive distribution in MLT!

Chapter 8

Observations

TODO: You know what would be great for putting this numerical work in context? A nice, consistent survey that breaks down the occurrence rate of Pc4 pulsations by harmonic, etc.

TODO: Anderson[3] located events by visual inspection of AMPTE/CCE data. He found that toroidal resonances outnumber poloidal ones about three-to-one. “Harmonic toroidal resonances” are spread 0600 to 1600. “Fundamental toroidal resonances” (which are not mutually exclusive with harmonic ones!) appear everywhere but dusk. Poloidal modes occur everywhere but dawn; odd and even harmonics are not distinguished. Notably, most observation time was spent at $L > 7$. Orbit near the equator, magnetic field instrumentation, so fundamental poloidal modes would have been hard to observe... and I need to reread this to figure out how he managed to observe fundamental toroidal modes!

TODO: Dai[17] found 890 poloidal Pc4 events using RBSP. Due to a cutoff in magnetic field amplitude, his findings are biased in favor of the even mode. Events are shown to be most common near noon, but smeared across the dayside, and with a few stragglers near midnight. Low- m waves were shown to be smeared a bit more, occurring across the entire dusk flank at low rates.

TODO: Motoba[72] looked specifically at Pgs – 105 events. Seen from midnight to noon, with a strong peak before dawn, 0300 or so. Events are identified by visual inspection.

TODO: Probably need some fluff here with appropriate citations for RBSP and its instrumentation.

TODO: The tools used in the present chapter — SPEDAS and the SPICE kernel — are publicly available. They run best with an IDL license, which is not, but they are functional using just the (free) IDL virtual machine. The code is wrapped up in a Git repository: <https://github.com/chizarlicious/RBSP> (maybe should make a GitHub organization to hold this code, to decouple it from my personal account?).

8.1 Sampling Bias and Event Selection

The present analysis makes use of as much Van Allen Probe data as is available at the time of writing: October 2012 to August 2015. Between the two probes, that’s just over 2000 days of observation.

Notably, the two probes are taken to be independent observers. The vast majority of Pc4 observations take place near apogee, where the probes are separated by several hours. Pc4 pulsations tend to be localized in MLT — indeed, this was a key justification for the model described in Chapter 5. The two probes simultaneously observe the same event only TODO: … of the time.

TODO: How common is it for one probe to see an event, then the other probe to fly through that same event an hour or two later?

Electric and magnetic waveform data is cleaned up by averaging over the probe’s spin period, 10.5 s. The three-dimensional electric field is then obtained using the assumption $\underline{E} \cdot \underline{B} = 0$. Notably, this assumption is taken only when the probe’s spin plane is offset from the magnetic field by at least 15° . The rest of the data — about half — is discarded, which introduces a sampling bias against the flanks.

A further bias is introduced by the probes' non-integer number of precessions around Earth. Pc4 pulsations are most commonly observed near apogee. As of July 2014, apogee had precessed once around Earth[17]. The present work considers roughly one and a half precessions; the nightside has been sampled at apogee twice as often as the dayside.

The spatial distribution of usable data — that is, data for which three-dimensional electric and magnetic fields are available — is shown in Figure 8.1. Bins are unitary in L (divided at integer L) and in MLT (centered at integer hours). Event distribution in magnetic latitude is not shown; the Van Allen Probes are localized to within **TODO: 15°** of the equatorial plane.

TODO: L is italicized and MLT is not? That seems weird.

Awkwardly, coverage is weakest from pre-dawn to the mid-afternoon — the exact regions where Pc4 pulsations have been shown to peak. In order to compensate for that fact, results in the present chapter are binned coarsely. Histogram bins are two hours wide in MLT. Only two bins are used in the radial direction: $L \leq 5$ and $L > 5$.

TODO: Most events occur between $L = 4$ and $L = 6$, but splitting at $L = 5$ is otherwise arbitrary. It might make more sense to split the bins wherever the median event is or something.

Field measurements are transformed from GSE coordinates into the same dipole coordinates used in Chapters 5 and 7. The z axis is parallel to the background magnetic field, which is estimated using a ten-minute running average of the magnetic field measurements. The y axis is defined per $\hat{y} \parallel \hat{z} \times \underline{r}$. The x axis is then defined per $\hat{x} \equiv \hat{y} \times \hat{z}$. This method is described by Liu[58], and guarantees that the axes are right-handed and pairwise orthogonal.

The ~ 1000 days of usable data are considered half an hour at a time — ~ 60 data points per event at the ten-second spinfit cadence. This allows for a frequency resolution of ~ 0.5 mHz in the discrete Fourier transform. Spectra are computed for all six field components: \tilde{B}_x , \tilde{B}_y , \tilde{B}_z , \tilde{E}_x , \tilde{E}_y , and \tilde{E}_z .

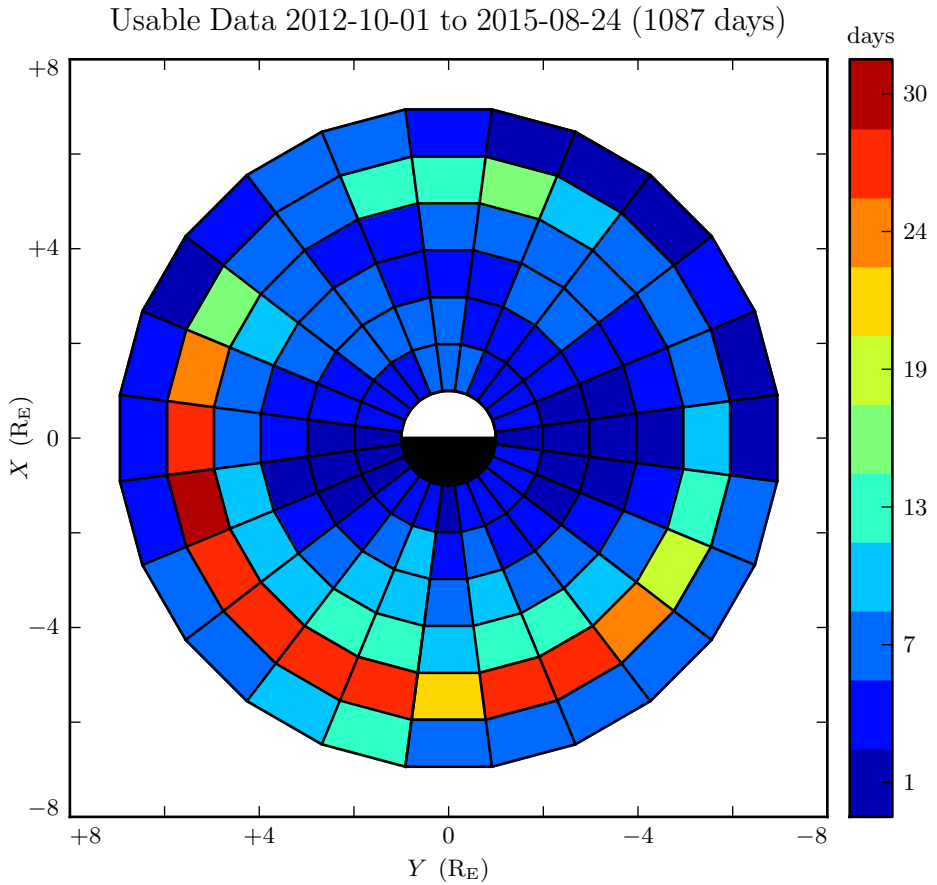


Figure 8.1: Three-dimensional electric field values are computed by assuming $\underline{E} \cdot \underline{B} = 0$. Data is discarded whenever the magnetic field falls within 15° of the spin plane, which introduces a bias against the flanks. Furthermore, the probes have completed only one and a half precessions around Earth; the dayside has been sampled once at apogee, and the nightside twice.

The background magnetic is subtracted off before performing each transform, leaving only the magnetic field perturbation along each axis. (As in Chapters 5 and 7, B_x refers not to the full magnetic field in the x direction, but to its perturbation from the zeroth-order field.) Each waveform is also shifted horizontally so that its mean over the thirty minute event is zero.

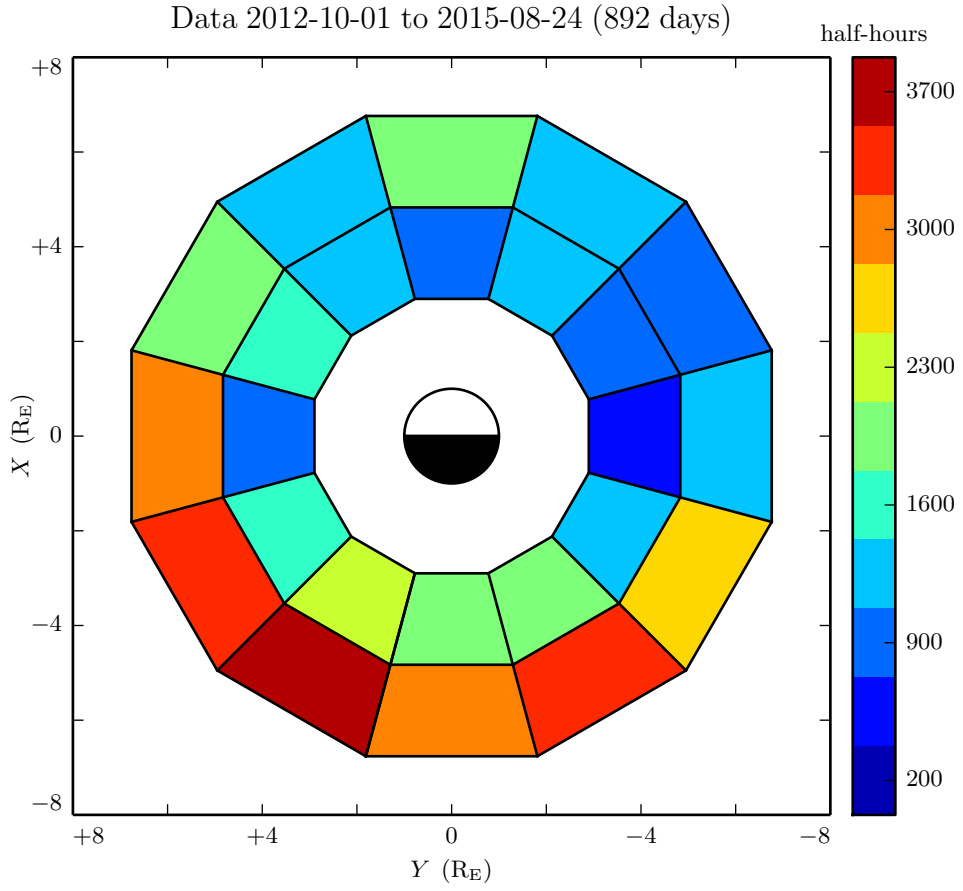


Figure 8.2: **TODO:** This is the sampling distribution used to normalize Dst-agnostic event counts. It's not clear that all of these plots are necessary.

Frequency-domain Poynting flux is computed from the electric and magnetic field transforms. Values are effective at the ionosphere; a factor of L^3 is introduced to account for the compression of the flux tube. Poloidal and toroidal Poynting flux, respectively, are given by:

$$\tilde{S}_P \equiv -\frac{L^3}{\mu_0} \tilde{E}_y \tilde{B}_x^* \quad \tilde{S}_T \equiv \frac{L^3}{\mu_0} \tilde{E}_x \tilde{B}_y^* \quad (8.1)$$

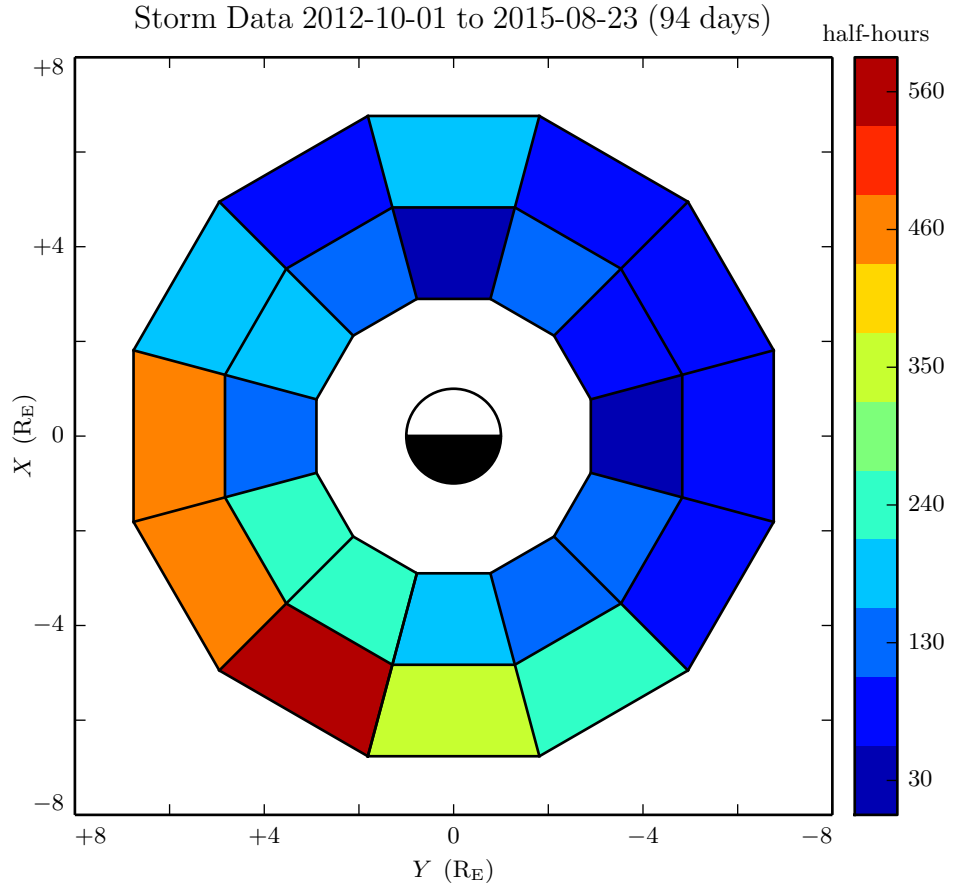


Figure 8.3: TODO: This is the sampling distribution used to normalize event counts at $\text{Dst} \geq -30 \text{ nT}$. It's not clear that all of these plots are necessary.

TODO: The Poynting flux scaled by L^3 to conserve energy. But doesn't the magnetic field be scale with L^3 to conserve flux, and the electric field scale with the magnetic field?

The Poynting fluxes \tilde{S} for each event are filtered based on frequency, magnitude, and phase offset. The poloidal and toroidal channels are checked independently; a given half hour can have no event, a poloidal event, a toroidal event, or both.

A Gaussian profile is fit to $|\text{Im}\tilde{S}|$, which corresponds to the magnitude of the standing wave (in turn, the real component is the traveling wave). If the fit fails, for example due

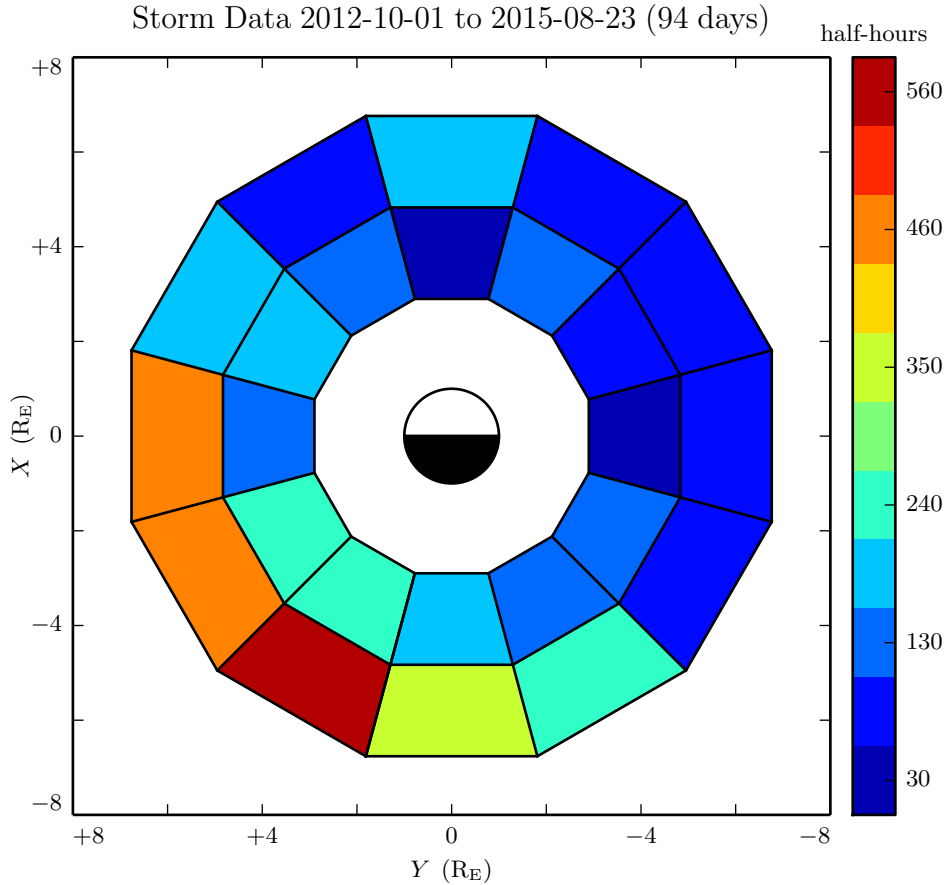


Figure 8.4: **TODO:** This is the sampling distribution used to normalize event counts at $\text{Dst} < -30 \text{ nT}$. It's not clear that all of these plots are necessary.

to non-finite values in the data, the event is discarded. The event is also discarded if the peak of the Gaussian does not correspond to the largest spectral feature in the data, standing or traveling; that is, the event is disqualified if the Gaussian is not centered within 5 mHz of the maximum value of $|\tilde{S}|$.

Non-Pc4 events are filtered out: any event for which the standing wave Gaussian does not fall in the range 7 mHz to 25 mHz. Notably, no filter is imposed on spectral width.

Out of consideration for instrument sensitivity, events are thresholded at a magnitude of $|\text{Im}\tilde{S}| \geq 10^{-2} \text{ mW/m}^2$.

Events are filtered based on the phase offset between the electric and magnetic field waveforms, given by $\arctan \frac{\text{Im} \tilde{S}}{\text{Re} \tilde{S}}$. For a purely traveling wave, the electric and magnetic field waveforms are in phase (0°) or in antiphase (180°). Standing waves have a phase of $\pm 90^\circ$ between their electric and magnetic field components. The events presented here are filtered conservatively in phase; the standing wave must just barely exceed the traveling wave (phase between 45° and 135° in absolute value).

TODO: A stricter cutoff in magnitude, or in phase, does not obviously affect the distributions of events... it just shrinks the sample size and makes everything look noisier.

Events are filtered on coherence, to ensure that the phase offset is credible. If the coherence between \tilde{E} and \tilde{B}^* is less than 0.9, the event is discarded. Coherence and phase are both measured at the discrete Fourier transform point closest to the peak of the Gaussian.

Finally, any event within 3° of the magnetic equator is discarded due to ambiguity in its phase. As discussed in Chapter 3, odd and even harmonics are distinguished by the sign of the phase offset between the electric and magnetic field. For example, in odd poloidal modes, an observer north of the equator sees B_x lead E_y by a phase of 90° , and an observer below the equator sees the opposite. When the probe is very close to the equator, an event's parity becomes ambiguous.

TODO: We try not to worry too much about first vs third harmonic, since we can't tell them apart except by guessing at frequency. Chisham and Orr[14] argue that around $7 R_E$, frequency around 10 mHz precludes higher harmonics. Or maybe look at [35]?

8.2 Overall Rate of Pc4 Events

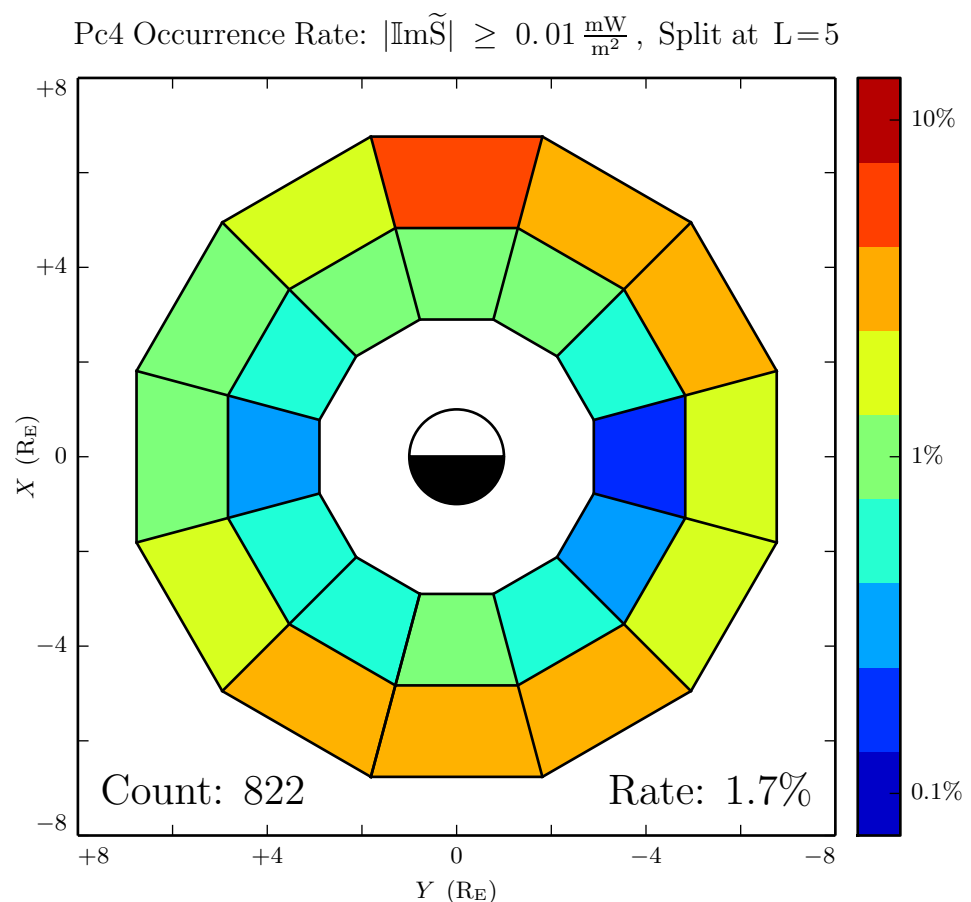


Figure 8.5: TODO: Pc4s are observed at all local times, but are most common near noon and least common near dusk.

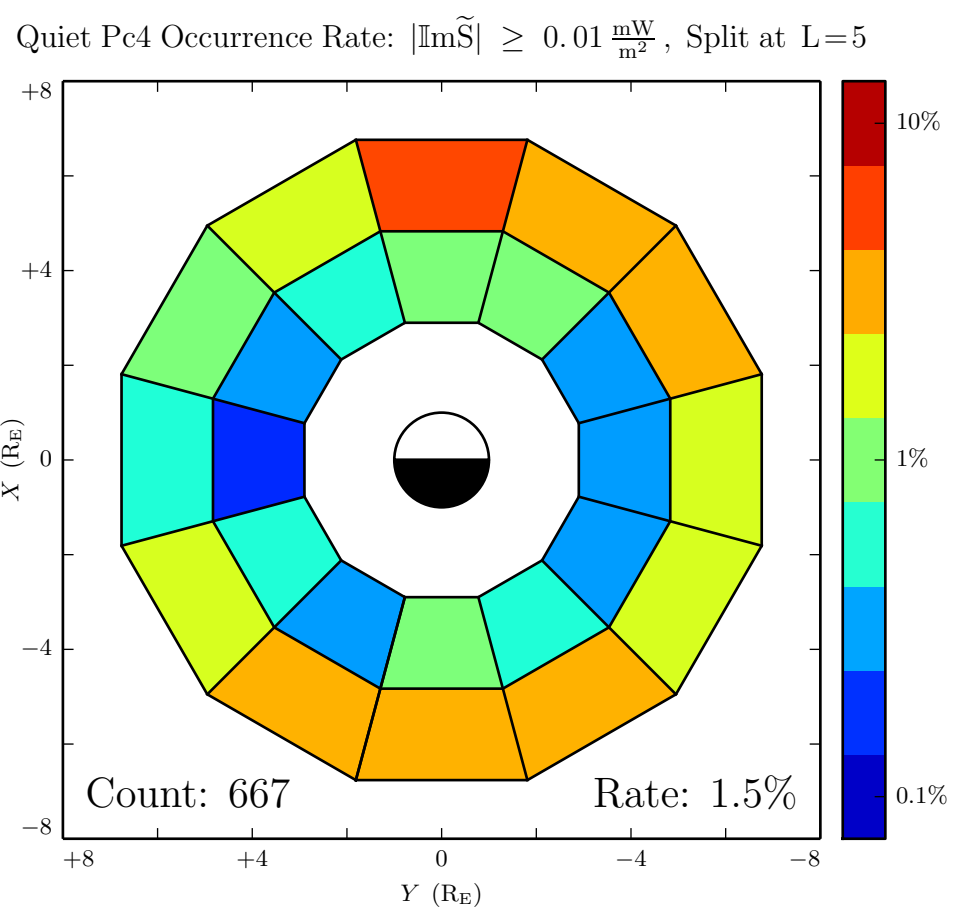


Figure 8.6: **TODO:** ...

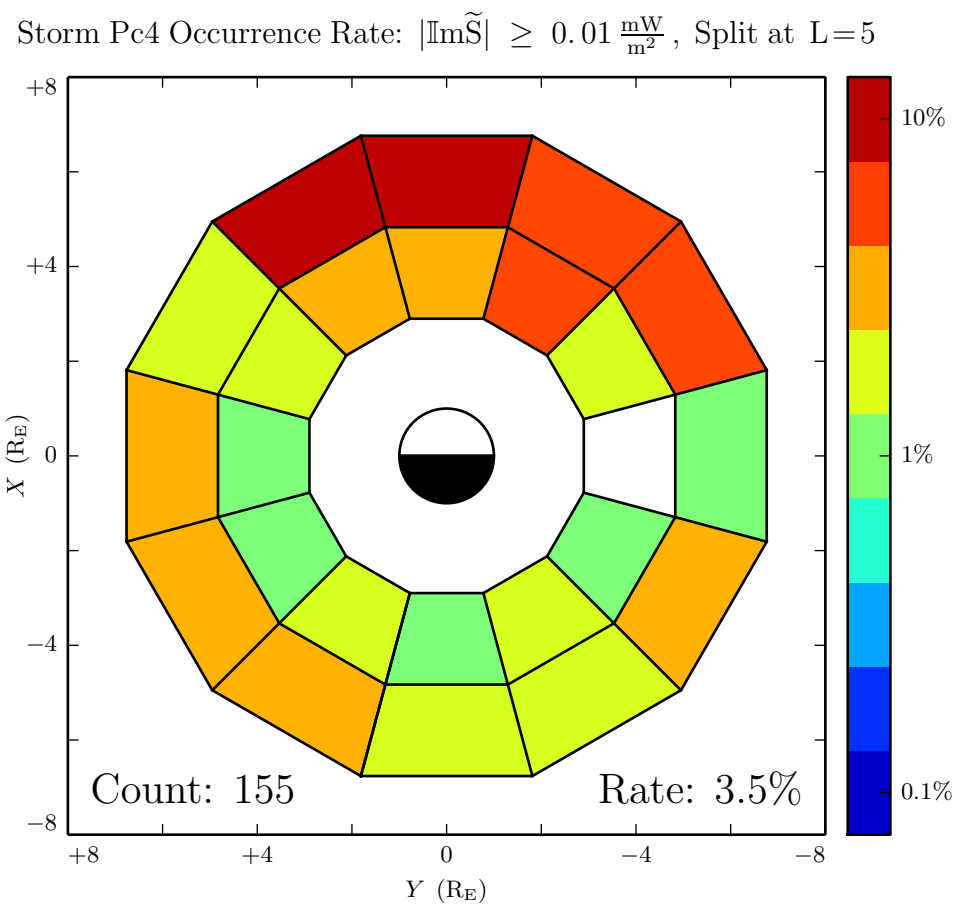


Figure 8.7: TODO: During geomagnetically active times, Pc4 pulsations become significantly more common, particularly near noon.

8.3 Pc4 Events by Mode

The filters described in Section 8.1 yield 822 events: 136 odd poloidal modes, 234 even poloidal modes, 445 odd toroidal modes, and 86 even toroidal modes. The distributions of those events are shown in Figures 8.8 and 8.10; counts are normalized to the sampling rates shown in Figures 8.2 and 8.4 respectively.

TODO: It's good to see that even poloidal modes and even toroidal modes are distributed similarly, since one turns into the other! The relationship is less clear for odd modes, though odd poloidal modes and odd toroidal modes are both least common at dusk.

TODO: Odd toroidal events are by far the most commonly observed.

TODO: Even modes are less likely to be observed on the ground? [94]

Pc4 Occurrence Rate by Mode: $|\text{Im}\tilde{S}| \geq 0.01 \frac{\text{mW}}{\text{m}^2}$, Split at L=5

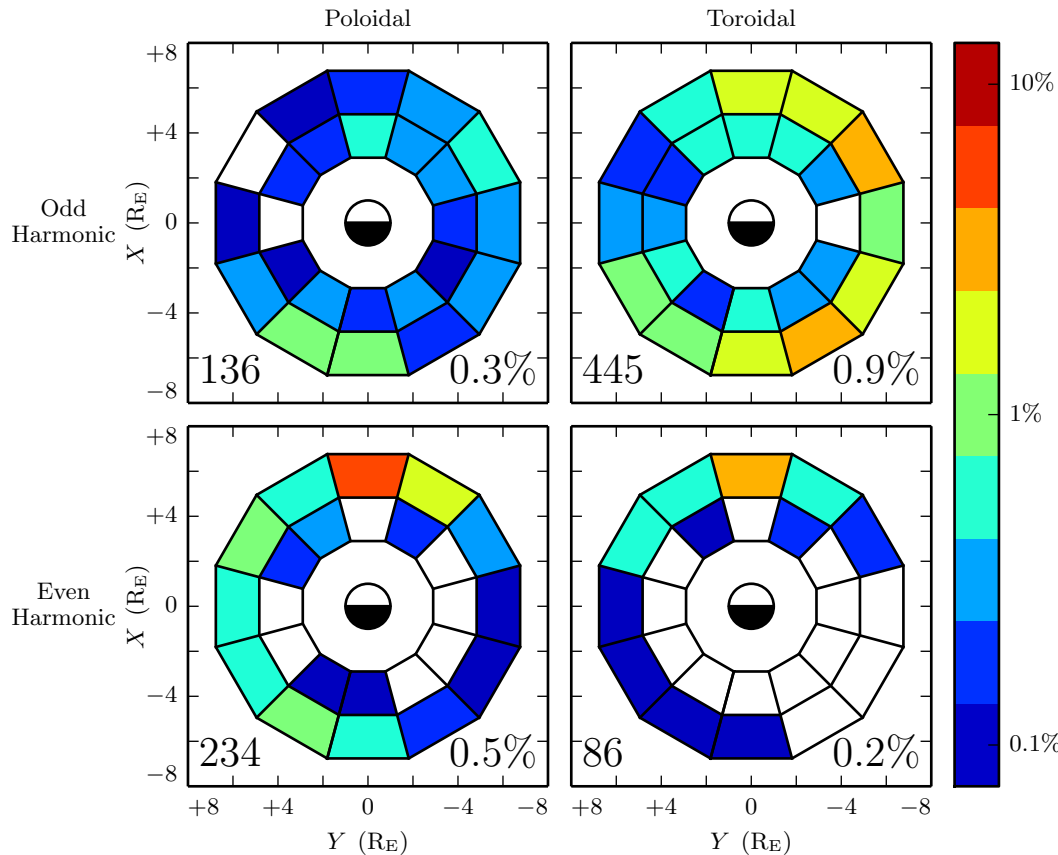


Figure 8.8: TODO: Even harmonics are strongly peaked at noon, with some presence smeared across the dusk side. Odd harmonics, on the other hand, are mostly seen on the dawn side.

Quiet Pc4 Occurrence Rate by Mode: $|\text{Im}\tilde{S}| \geq 0.01 \frac{\text{mW}}{\text{m}^2}$, Split at $L=5$

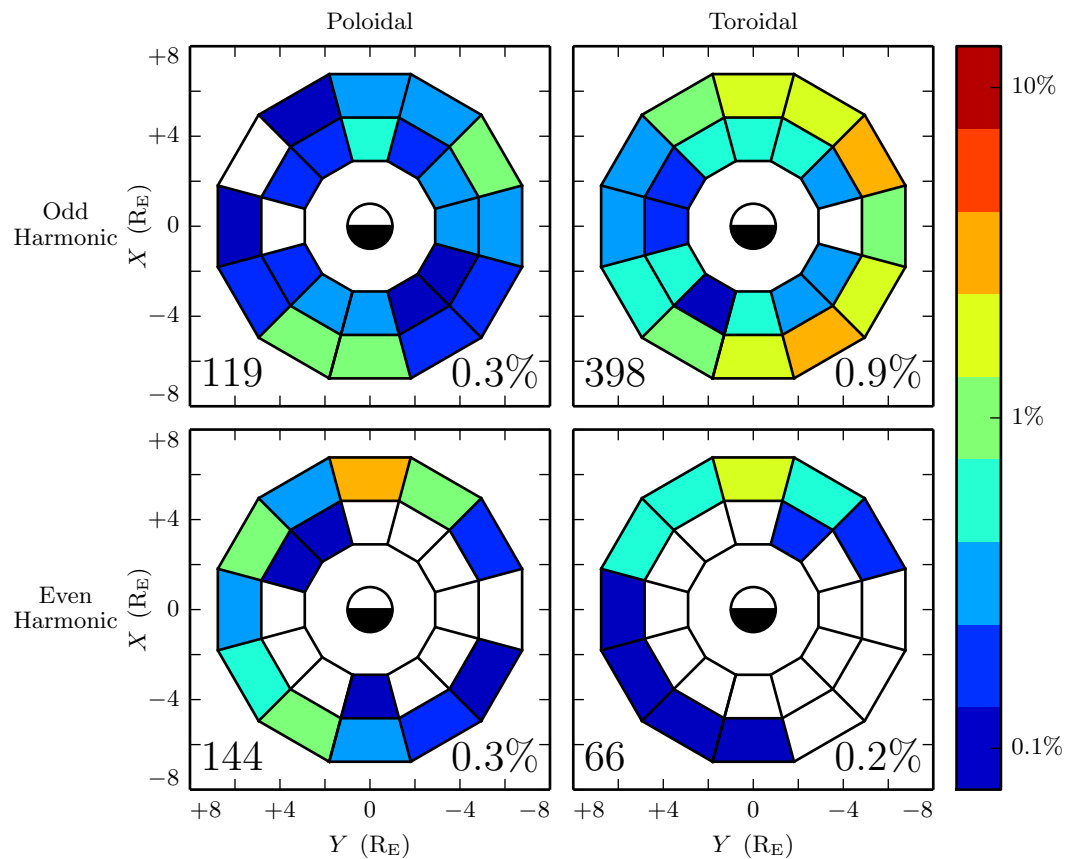


Figure 8.9: **TODO:** ...

Storm Pc4 Occurrence Rate by Mode: $|\text{Im}\tilde{S}| \geq 0.01 \frac{\text{mW}}{\text{m}^2}$, Split at $L=5$

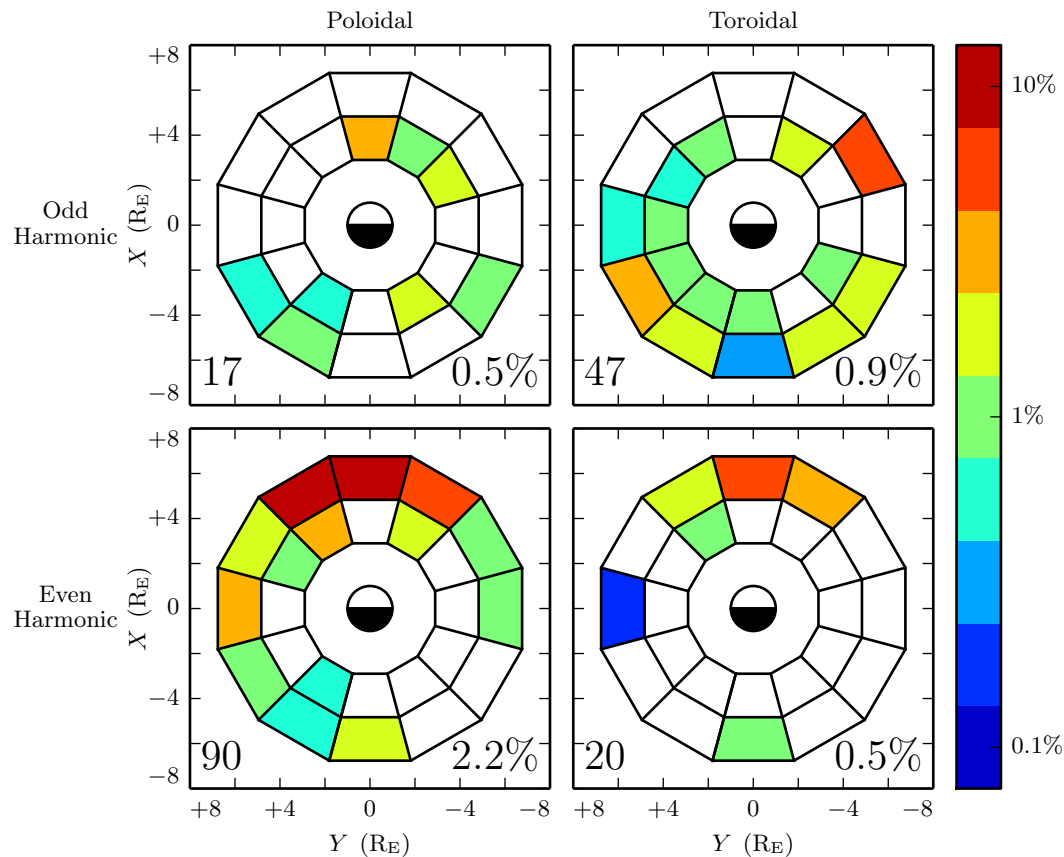


Figure 8.10: TODO: Pc4 events near noon are much more common during geomagnetically active times.

8.4 Pc4 Events Inside and Outside the Plasmapause

TODO: In the present section, bins in the radial direction indicate whether the event is located inside or outside of the plasmapause. Plasmapause locations are estimated from work by Scott. Normalization is also computed based on the sampling rate inside and outside the plasmapause.

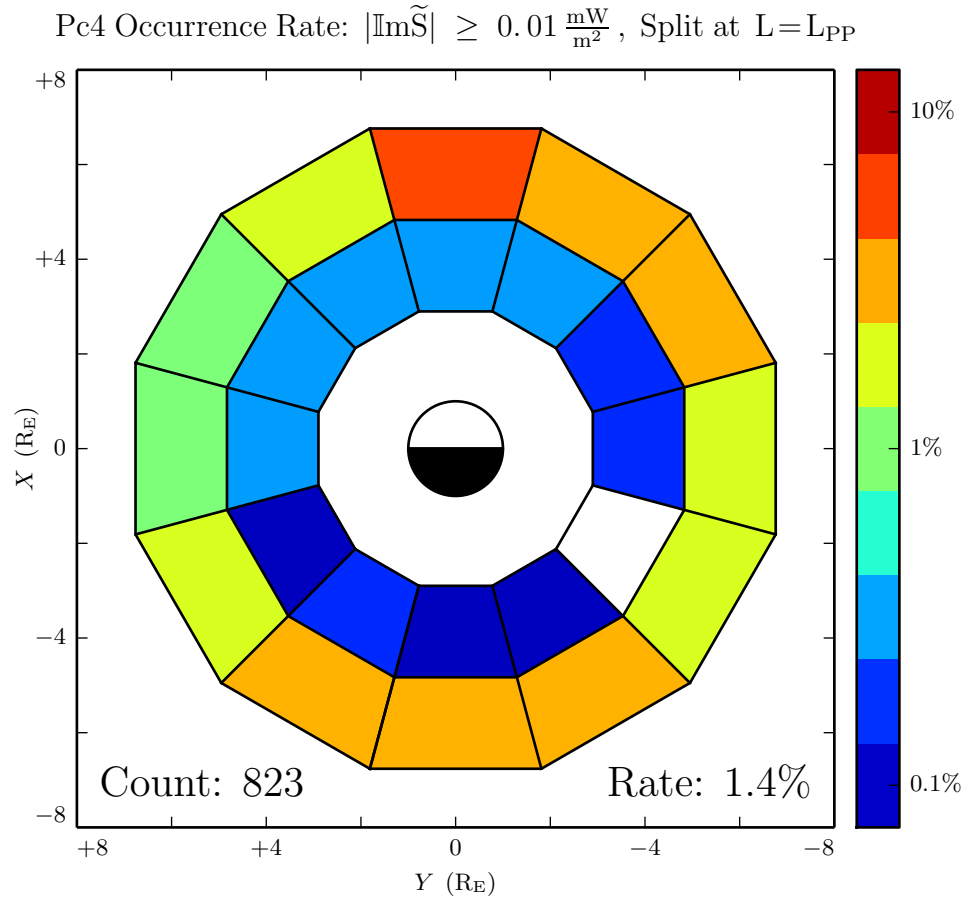


Figure 8.11: TODO: Pc4 events are usually outside the plasmapause.

Pc4 Occurrence Rate by Mode: $|\text{Im}\tilde{S}| \geq 0.01 \frac{\text{mW}}{\text{m}^2}$, Split at $L=L_{\text{PP}}$

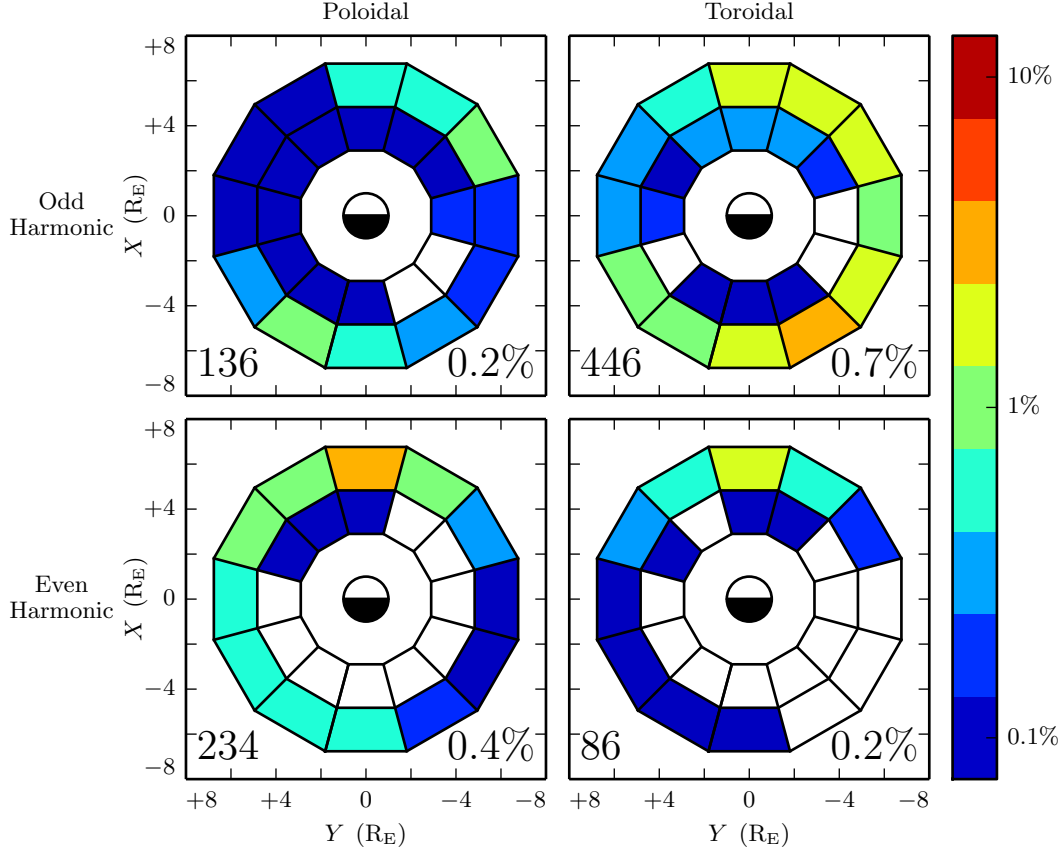


Figure 8.12: TODO: Odd events are sometimes inside the plasmapause. Even events are almost never inside the plasmapause.

8.5 Poloidal Pc4 Events by Compressional Coupling

TODO: Low- m poloidal Pc4 events are coupled to the compressional mode, while high- m ones are not.

TODO: The value of $\tilde{B}_z/\tilde{B}_x = 0.2$ comes from Dai[17]. Can we match this up to an m value?

Poloidal Pc4 by Compressional Coupling: $|\text{Im}\tilde{\mathbf{S}}| \geq 0.01 \frac{\text{mW}}{\text{m}^2}$, Split at $L=5$

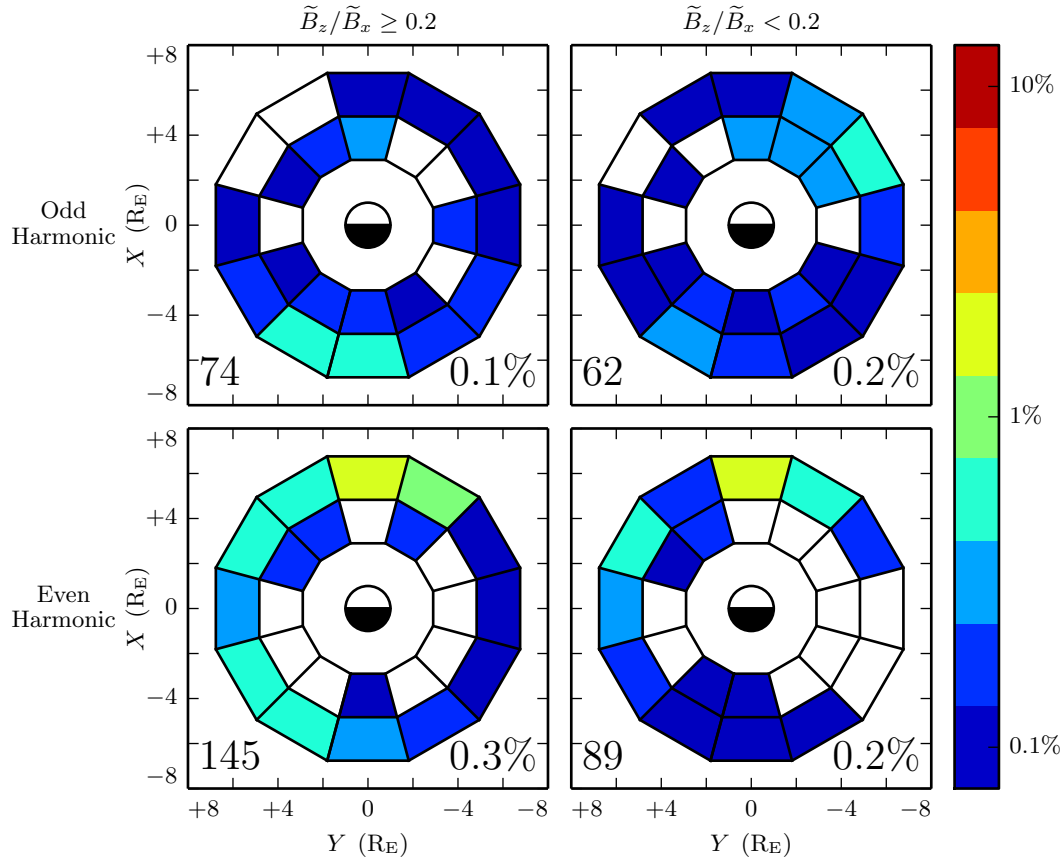


Figure 8.13: TODO: Odd poloidal Pc4 events have a peak pre-noon and another peak near midnight. The pre-noon peak seems to be composed of high- m events, and the midnight peak seems to be low- m events. Low- m even poloidal events are spread broadly across the dusk side, while high- m even events are peaked strongly on the dayside — consistent with Dai's results[17].

Quiet Poloidal Pc4 by Compressional Coupling: $|\text{Im}\tilde{\mathbf{S}}| \geq 0.01 \frac{\text{mW}}{\text{m}^2}$, Split at $L = \xi$

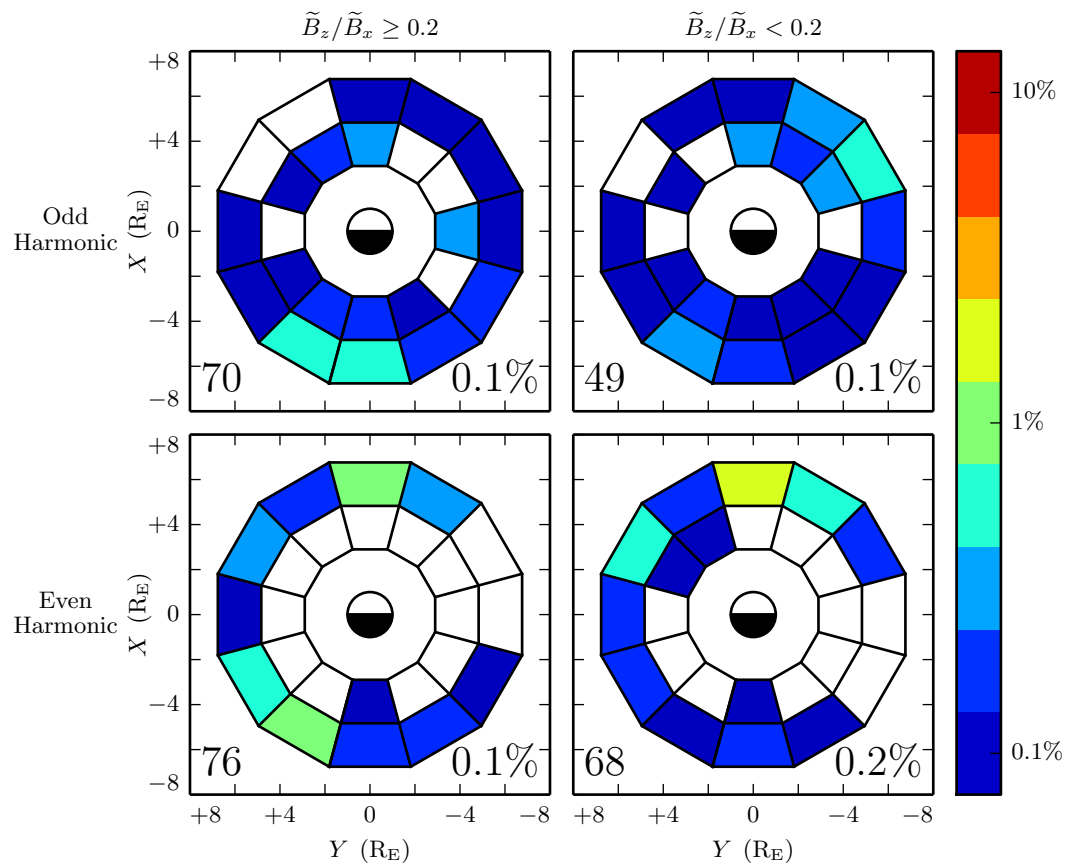


Figure 8.14: TODO: Looks about like Figure 8.13...

Storm Poloidal Pc4 by Compressional Coupling: $|\text{Im}\tilde{S}| \geq 0.01 \frac{\text{mW}}{\text{m}^2}$, Split at $L=5$

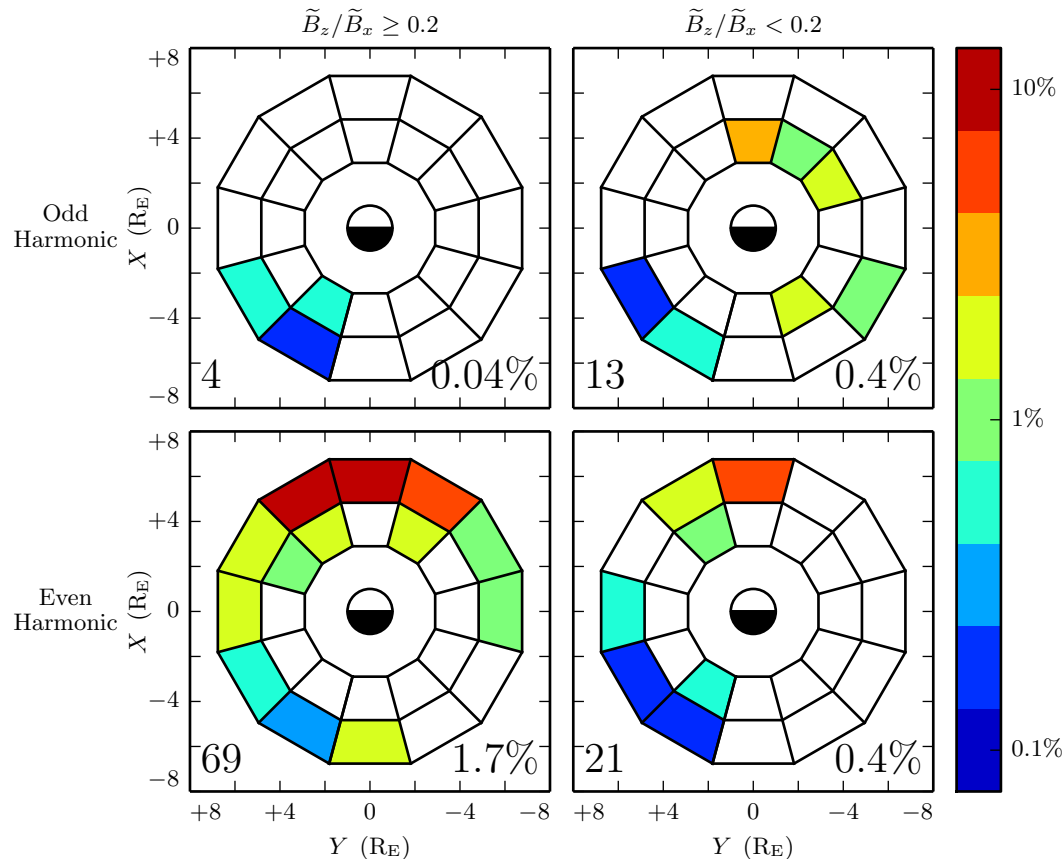


Figure 8.15: TODO: During storm-time, the rate of high- m poloidal modes goes up for both odd and even modes. The rate of low- m even modes goes WAY up. And the rate of low- m odd modes goes down!

8.6 Pc4 Events by Spectral Width

TODO: We did a Gaussian fit of each spectrum as part of the event selection process. That gives FWHM. Let's divide the events at a FWHM of 1.3 mHz, the (rounded) median value.

Poloidal Pc4 by Spectral Width: $|\text{Im}\tilde{S}| \geq 0.01 \frac{\text{mW}}{\text{m}^2}$, Split at L=5

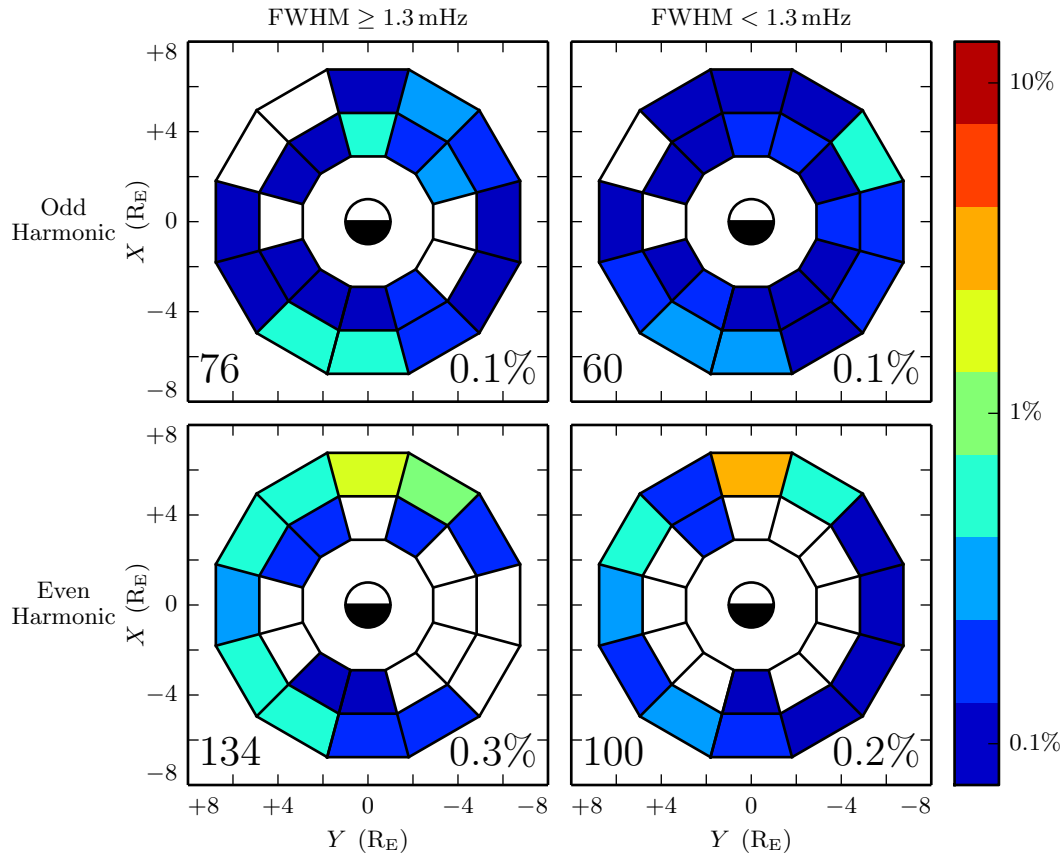


Figure 8.16: TODO: Odd poloidal events skew a bit toward midnight when the spectra are broad/messy. Even poloidal modes skew significantly duskward — or, maybe, nice clean peaks are particularly common near noon.

Quiet Poloidal Pc4 by Spectral Width: $|\text{Im}\tilde{S}| \geq 0.01 \frac{\text{mW}}{\text{m}^2}$, Split at $L=5$

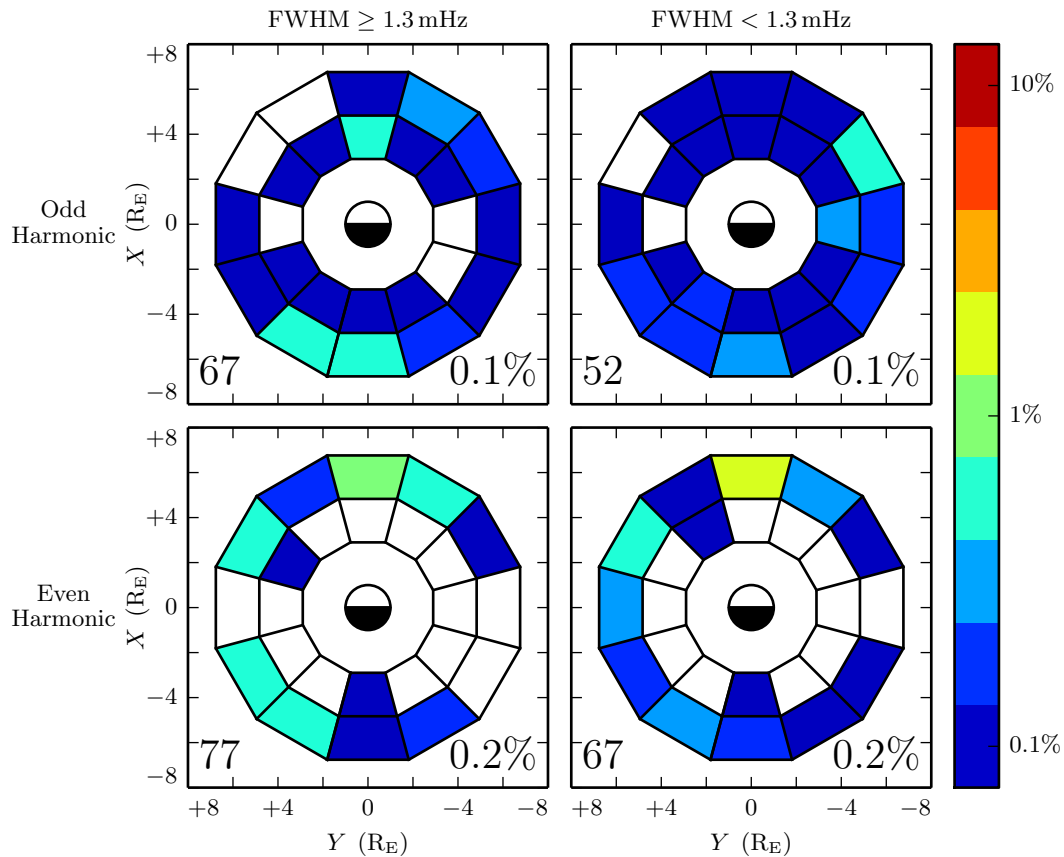


Figure 8.17: TODO: Looks about like Figure 8.16...

Storm Poloidal Pc4 by Spectral Width: $|Im\tilde{S}| \geq 0.01 \frac{mW}{m^2}$, Split at $L=5$

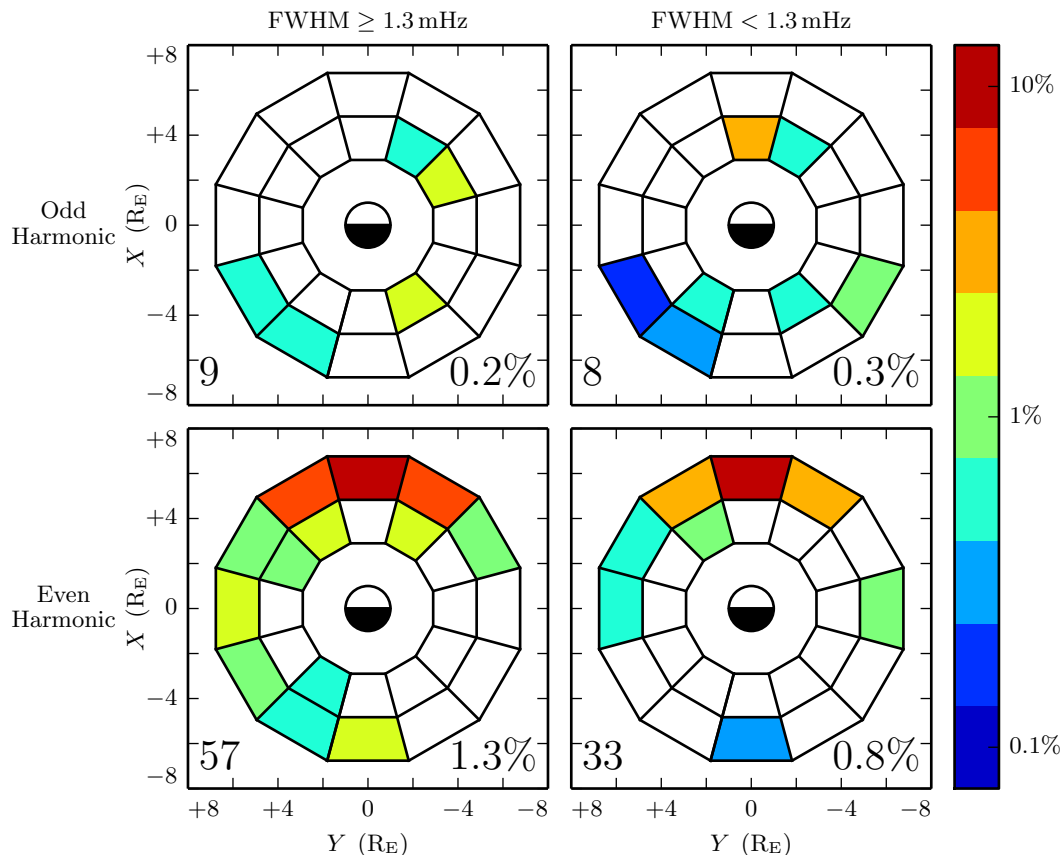


Figure 8.18: TODO: Even poloidal events skew toward broad/messy spectra during storm time, compared to the quiet time distribution of FWHM.

Toroidal Pc4 by Spectral Width: $|\text{Im}\tilde{S}| \geq 0.01 \frac{\text{mW}}{\text{m}^2}$, Split at L=5

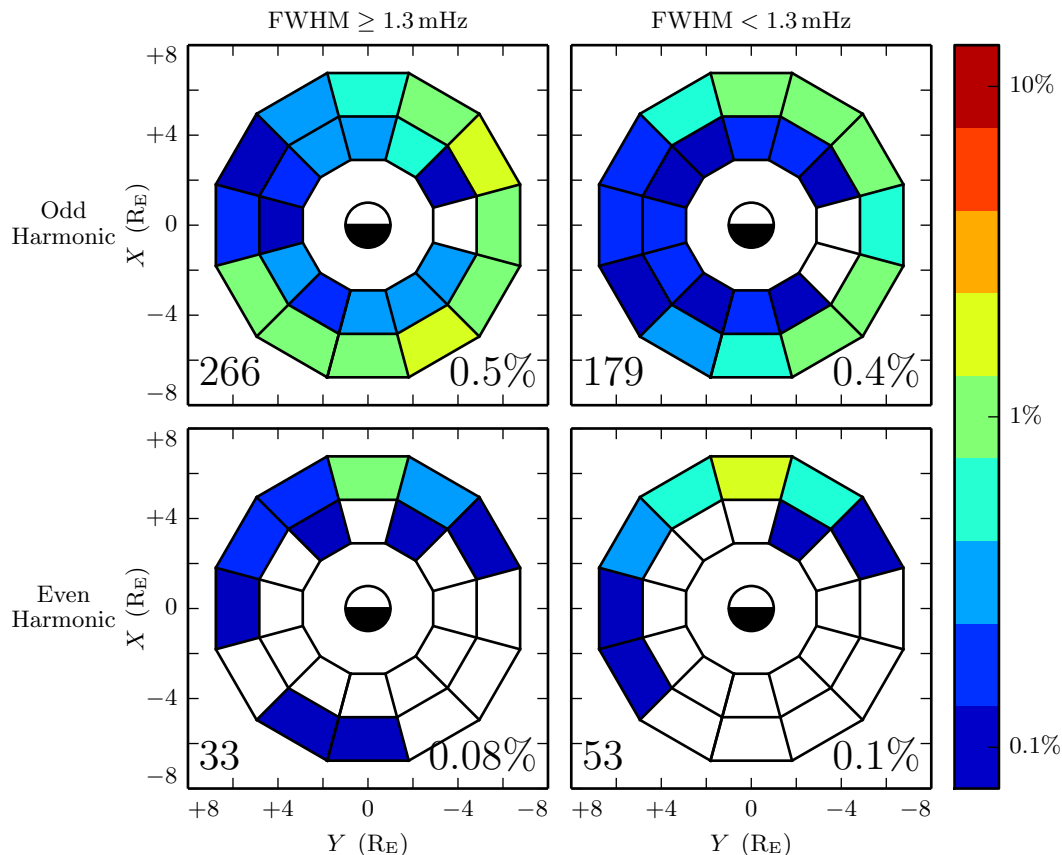


Figure 8.19: TODO: Odd toroidal modes are skewed overall toward broad/messy spectra.

Quiet Toroidal Pc4 by Spectral Width: $|\text{Im}\tilde{S}| \geq 0.01 \frac{\text{mW}}{\text{m}^2}$, Split at $L=5$

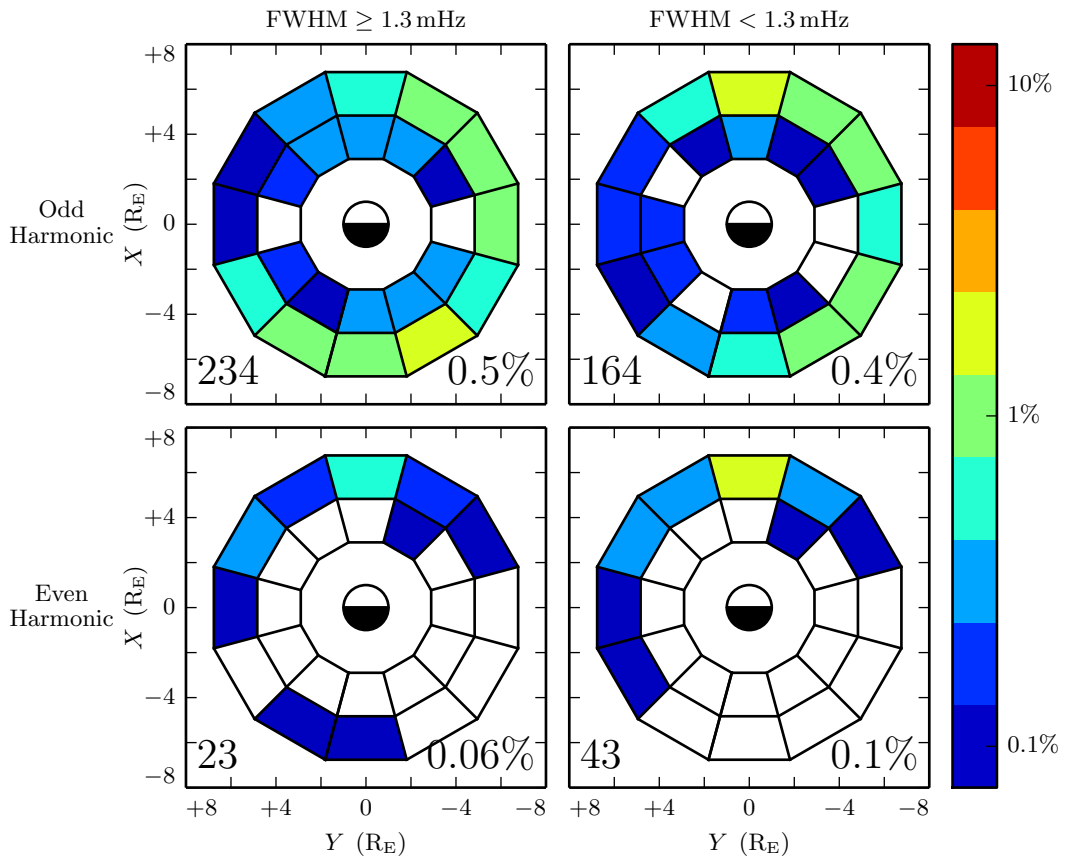


Figure 8.20: **TODO:** ...

Storm Toroidal Pc4 by Spectral Width: $|\text{Im}\tilde{S}| \geq 0.01 \frac{\text{mW}}{\text{m}^2}$, Split at $L=5$

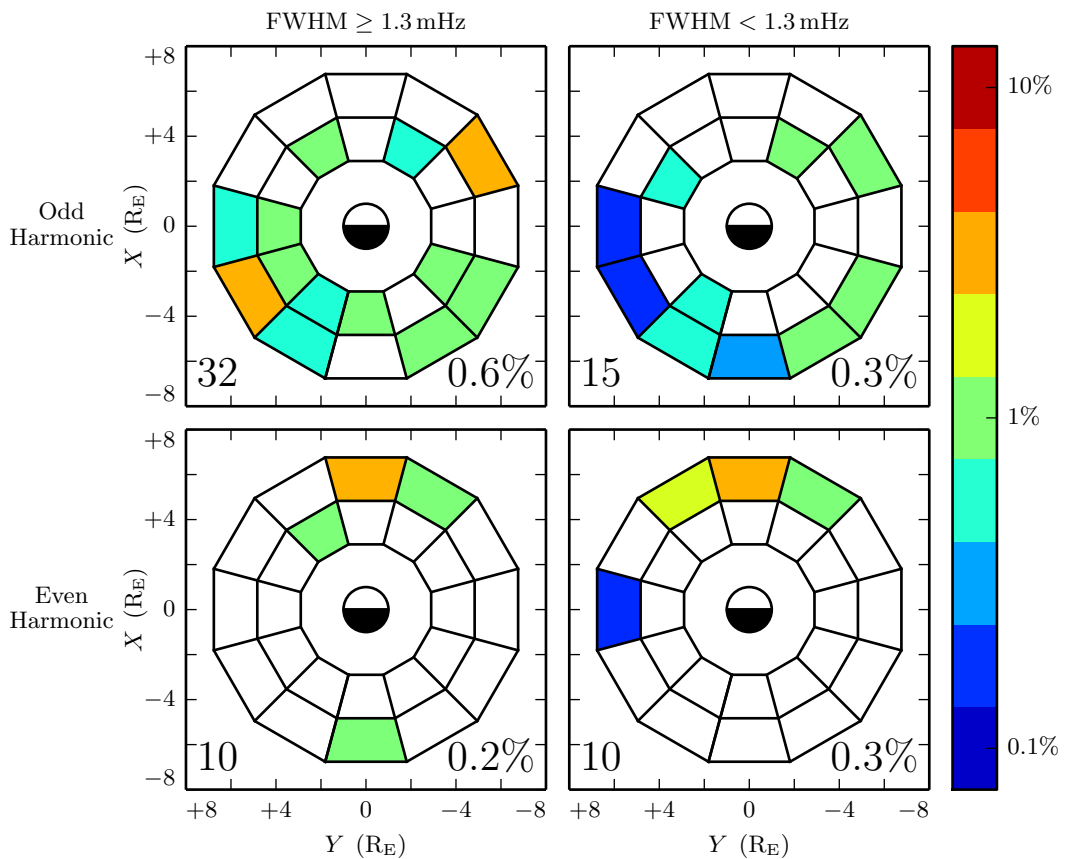


Figure 8.21: TODO: ...

8.7 Double-Triggering Events

The poloidal and toroidal triggers are checked for events independently. In about 10 % of cases, both trigger at the same time. In such cases, the poloidal and toroidal event almost always have the same parity.

Odd harmonics are comparably likely to trigger on both the poloidal and toroidal channels whether or not it's storm time. Even double modes are much more common during storm time than they are during quiet time.

Odd double-triggering events rarely happen twice in the same day — the 24 events in the top row of Figure 8.22 occur on \sim 20 different dates (and each of the three odd storm double events is on a different date).

Even double-triggering events often happen multiple times in the same day. The 36 calm-time double events are spread over 15 days; the 14 storm double events are spread over only 7 days.

Itaneous Poloidal + Toroidal Pc4 Occurrence Rate: $|\text{Im}\tilde{S}| \geq 0.01 \frac{\text{mW}}{\text{m}^2}$, Split at

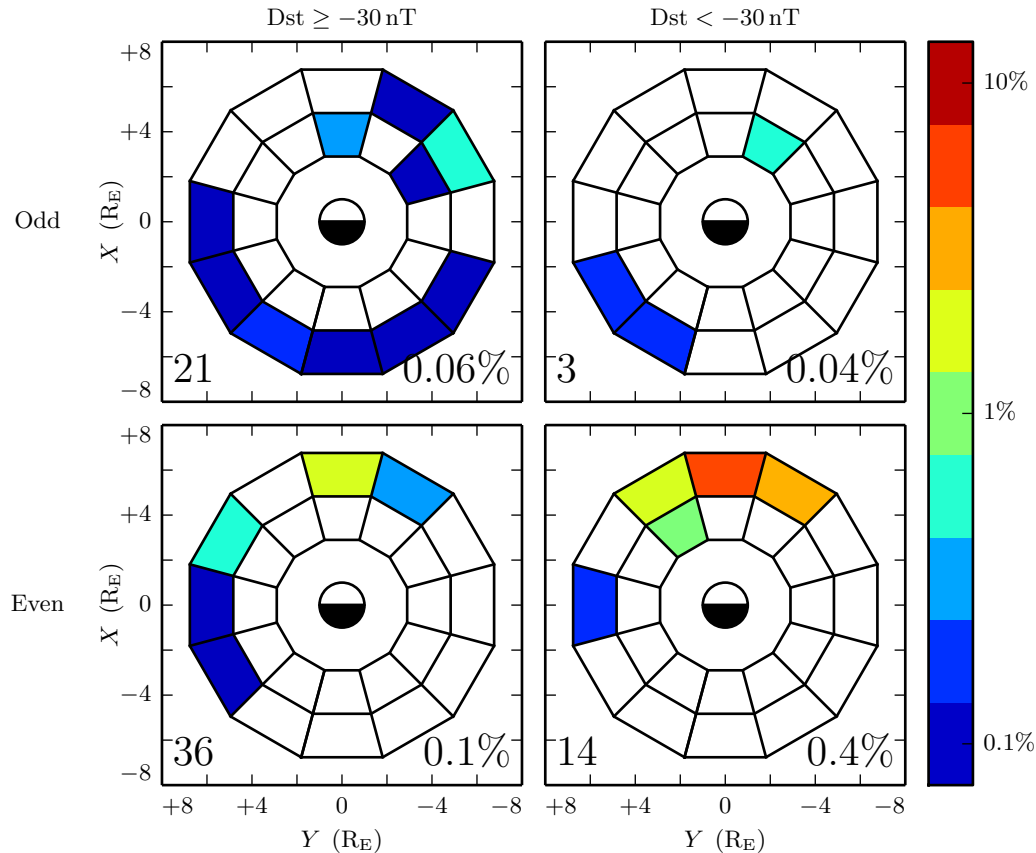


Figure 8.22: **TODO: ...**

8.8 Discussion

TODO: ...

Chapter 9

Conclusion

9.1 Summary of Results

TODO: Code development.

TODO: Numerical results.

TODO: Observational results.

9.2 Future Work

TODO: Code development.

Arbitrary deformation of grid. Get $\hat{e}_i = \frac{\partial}{\partial u^i} \underline{x}$, then $g_{ij} = \hat{e}_i \cdot \hat{e}_j$, then invert the metric tensor for contravariant components.

MPI. Some benchmarks with time to compute vs time to broadcast. This might make sense for inertial length scales.

Better ionospheric profiles. Distinction between the dawn and dusk flanks. Maybe even update the conductivity based on energy deposition — precipitation causes ionization!

IRI ionosphere model. Solar illumination effects.

TODO: Numerical work.

More complicated driving. Higher harmonics, non-sinusoidal waveforms. Maybe even drive based on events/Dst?

Look at runs with a plasmasphere further out. Can we get nicer resonance on the nightside? A larger plasmapause will cause L=5 to line up better with Pc4 frequencies.

TODO: Data analysis.

Look at distribution of these events with respect to the plasmapause, storm phase...

References

- [1] S.-I. Akasofu. The development of the auroral substorm. *Planetary and Space Science*, 12(4):273–282, 1964.
- [2] H. Alfvén. On the cosmogony of the solar system III. *Stockholms Observatoriums Annaler*, 14:9.1–9.29, 1946.
- [3] B. J. Anderson, M. J. Engebretson, S. P. Rounds, L. J. Zanetti, and T. A. Potemra. A statistical study of Pc 3-5 pulsations observed by the AMPTE/CCE magnetic fields experiment, 1. occurrence distributions. *J. Geophys. Res.*, 95(A7):10495, 1990.
- [4] V. Angelopoulos. The THEMIS mission. *Space Science Reviews*, 141(1-4):5–34, 2008.
- [5] K. Birkeland. Expédition norvégienne de 1899-1900 pour l'étude des aurores boréales. *Mat. Naturvidensk. Kl.*, KI(I), 1901.
- [6] J. P. Boris. A physically motivated solution of the Alfvén problem. *NRL Memorandum Report*, 2167, 1970.
- [7] A. Brekke, T. Feder, and S. Berger. Pc4 giant pulsations recorded in Tromsø, 1929-1985. *Journal of Atmospheric and Terrestrial Physics*, 49(10):1027–1032, 1987.
- [8] C. W. Carlson, R. F. Pfaff, and J. G. Watzin. The fast auroral Snapshot (FAST) mission. *Geophys. Res. Lett.*, 25(12):2013–2016, 1998.

- [9] A. A. Chan, M. Xia, and L. Chen. Anisotropic alfvén-balloonning modes in Earth's magnetosphere. *J. Geophys. Res. Space Physics*, 99(A9):17351–17366, 1994.
- [10] L. Chen and A. Hasegawa. A theory of long-period magnetic pulsations: 1. steady state excitation of field line resonance. *J. Geophys. Res.*, 79(7):1024–1032, 1974.
- [11] L. Chen and A. Hasegawa. Kinetic theory of geomagnetic pulsations: 1. internal excitations by energetic particles. *J. Geophys. Res.*, 96(A2):1503, 1991.
- [12] L. Chen, R. White, C. Cheng, F. Romanelli, J. Weiland, R. Hay, J. V. Dam, D. Barnes, M. Rosenbluth, and S. Tsai. Theory and simulation of fishbone-type instabilities in beam-heated tokamaks. Technical report, 1984.
- [13] C. Z. Cheng and Q. Qian. Theory of ballooning-mirror instabilities for anisotropic pressure plasmas in the magnetosphere. *J. Geophys. Res.*, 99(A6):11193, 1994.
- [14] G. Chisham and D. Orr. Statistical studies of giant pulsations (pgs): Harmonic mode. *Planetary and Space Science*, 39(7):999–1006, 1991.
- [15] W. D. Cummings, R. J. O'Sullivan, and P. J. Coleman. Standing Alfvén waves in the magnetosphere. *J. Geophys. Res.*, 74(3):778–793, 1969.
- [16] L. Dai. Collisionless magnetic reconnection via Alfvén eigenmodes. *Phys. Rev. Lett.*, 102(24), 2009.
- [17] L. Dai, K. Takahashi, R. Lysak, C. Wang, J. R. Wygant, C. Kletzing, J. Bonnell, C. A. Cattell, C. W. Smith, R. J. MacDowall, S. Thaller, A. Breneman, X. Tang, X. Tao, and L. Chen. Storm time occurrence and spatial distribution of Pc4 poloidal ULF waves in the inner magnetosphere: A Van Allen Probes statistical study. *J. Geophys. Res. Space Physics*, 120:4748–4762, 2015.
- [18] L. Dai, K. Takahashi, J. R. Wygant, L. Chen, J. Bonnell, C. A. Cattell, S. Thaller, C. Kletzing, C. W. Smith, R. J. MacDowall, D. N. Baker, J. B. Blake, J. Fennell, S. Claudepierre, H. O. Funsten, G. D. Reeves, and H. E. Spence. Excitation of poloidal standing Alfvén waves through drift resonance wave-particle interaction. *Geophys. Res. Lett.*, 40:4127–4132, 2013.

- [19] A. W. Degeling, R. Rankin, and Q.-G. Zong. Modeling radiation belt electron acceleration by ULF fast mode waves, launched by solar wind dynamic pressure fluctuations. *J. Geophys. Res. Space Physics*, 119(11):8916–8928, 2014.
- [20] W. D. D’haeseleer, W. N. G. H. J. D. Callen, and J. L. Shohet. *Flux Coordinates and Magnetic Field Structure*. Springer-Verlag, New York, 1991.
- [21] D. Q. Ding, R. E. Denton, M. K. Hudson, and R. L. Lysak. An MHD simulation study of the poloidal mode field line resonance in the Earth’s dipole magnetosphere. *J. Geophys. Res.*, 100:63–77, 1995.
- [22] J. W. Dungey. The attenuation of Alfvén waves. *J. Geophys. Res.*, 59(3):323–328, 1954.
- [23] J. W. Dungey. Interplanetary magnetic field and the auroral zones. *Phys. Rev. Lett.*, 6(2):47–48, 1961.
- [24] A. Einstein. Die grundlage der allgemeinen relativitätstheorie. *Ann. Phys.*, 354:769–822, 1916.
- [25] S. R. Elkington, M. K. Hudson, and A. A. Chan. Acceleration of relativistic electrons via drift-resonant interaction with toroidal-mode Pc-5 ULF oscillations. *Geophys. Res. Lett.*, 26(21):3273–3276, 1999.
- [26] M. J. Engebretson, D. L. Murr, K. N. Erickson, R. J. Strangeway, D. M. Klumpar, S. A. Fuselier, L. J. Zanetti, and T. A. Potemra. The spatial extent of radial magnetic pulsation events observed in the dayside near synchronous orbit. *J. Geophys. Res.*, 97(A9):13741, 1992.
- [27] P. T. I. Eriksson, L. G. Blomberg, A. D. M. Walker, and K.-H. Glassmeier. Poloidal ULF oscillations in the dayside magnetosphere: a Cluster study. *Ann. Geophys.*, 23(7):2679–2686, 2005.
- [28] S. Fujita and T. Tamao. Duct propagation of hydromagnetic waves in the upper ionosphere, 1, electromagnetic field disturbances in high latitudes associated with localized incidence of a shear Alfvén wave. *J. Geophys. Res.*, 93(A12):14665, 1988.

- [29] K.-H. Glassmeier. Magnetometer array observations of a giant pulsation event. *J. Geophys.*, 48:127–138, 1980.
- [30] K.-H. Glassmeier. On the influence of ionospheres with non-uniform conductivity distribution on hydromagnetic waves. *J. Geophys.*, 54(2):125–137, 1984.
- [31] K.-H. Glassmeier, S. Buchert, U. Motschmann, A. Korth, and A. Pedersen. Concerning the generation of geomagnetic giant pulsations by drift-bounce resonance ring current instabilities. *Ann. Geophysicae*, 17:338–350, 1999.
- [32] K.-H. Glassmeier, D. Klimushkin, C. Othmer, and P. Mager. ULF waves at mercury: Earth, the giants, and their little brother compared. *Advances in Space Research*, 33(11):1875–1883, 2004.
- [33] C. Goertz. Kinetic alfvén waves on auroral field lines. *Planetary and Space Science*, 32(11):1387–1392, 1984.
- [34] C. K. Goertz and R. W. Boswell. Magnetosphere-ionosphere coupling. *J. Geophys. Res.*, 84(A12):7239, 1979.
- [35] C. A. Green. Giant pulsations in the plasmasphere. *Planetary and Space Science*, 33(10):1155–1168, 1985.
- [36] J. L. Green and S. Boardsen. Duration and extent of the great auroral storm of 1859. *Advances in Space Research*, 38(2):130–135, 2006.
- [37] C. Greifinger and P. S. Greifinger. Theory of hydromagnetic propagation in the ionospheric waveguide. *J. Geophys. Res.*, 73(23):7473–7490, 1968.
- [38] B. C. Hall. *Lie Groups, Lie Algebras, and Representations*. Graduate Texts in Mathematics. Springer, New York, second edition, 2015.
- [39] Y. X. Hao, Q.-G. Zong, Y. F. Wang, X.-Z. Zhou, H. Zhang, S. Y. Fu, Z. Y. Pu, H. E. Spence, J. B. Blake, J. Bonnell, J. R. Wygant, and C. A. Kletzing. Interactions of energetic electrons with ULF waves triggered by interplanetary shock: Van allen probes observations in the magnetotail. *J. Geophys. Res. Space Physics*, 119(10):8262–8273, 2014.

- [40] L. Harang. *Pulsations in the terrestrial magnetic records at high latitude stations*. Grondahl, 1942.
- [41] O. Hillebrand, J. Muench, and R. L. McPherron. Ground-satellite correlative study of a giant pulsation event. *Journal of Geophysics Zeitschrift Geophysik*, 51:129–140, 1982.
- [42] W. J. Hughes. The effect of the atmosphere and ionosphere on long period magnetospheric micropulsations. *Planet. Space Sci.*, 22:1157–1172, 1974.
- [43] W. J. Hughes. Magnetospheric ULF waves: A tutorial with a historical perspective. In M. J. Engebretson, K. Takahashi, and M. Scholer, editors, *Solar Wind Sources of Magnetospheric Ultra-Low-Frequency Waves*, volume 81 of *Geophys. Monogr.*, pages 1–12. American Geophysical Union, Washington, DC, 1994.
- [44] W. J. Hughes and D. J. Southwood. The screening of micropulsation signals by the atmosphere and ionosphere. *J. Geophys. Res.*, 81(19):3234–3240, 1976.
- [45] W. J. Hughes, D. J. Southwood, B. Mauk, R. L. McPherron, and J. N. Barfield. Alfvén waves generated by an inverted plasma energy distribution. *Nature*, 275(5675):43–45, 1978.
- [46] J. A. Jacobs, Y. Kato, S. Matsushita, and V. A. Troitskaya. Classification of geomagnetic micropulsations. *J. Geophys. Res.*, 69(1):180–181, 1964.
- [47] T. Karlsson and G. T. Marklund. A statistical study of intense low-altitude electric fields observed by freja. *Geophys. Res. Lett.*, 23(9):1005–1008, 1996.
- [48] Y. Kato and T. Tsutomu. Hydromagnetic oscillations in a conducting medium with hall conduct-ivity under the uniform magnetic field. *Science reports of the Tohoku University. Ser. 5, Geophysics*, 7(3):147–164, 1956.
- [49] M. C. Kelley. *The Earth’s Ionosphere*. Academic Press, San Diego, second edition, 1989.
- [50] R. L. Kessel. Solar wind excitation of pc5 fluctuations in the magnetosphere and on the ground. *J. Geophys. Res.*, 113(A4), 2008.

- [51] D. Y. Klimushkin, P. N. Mager, and K.-H. Glassmeier. Toroidal and poloidal Alfvén waves with arbitrary azimuthal wavenumbers in a finite pressure plasma in the earth's magnetosphere. *Annales Geophysicae*, 22(1):267–287, 2004.
- [52] S. Kokubun. Observations of Pc pulsations in the magnetosphere: Satellite-ground correlation. *J. Geomagn. Geoelec*, 32(Supplement2):SII17–SII39, 1980.
- [53] S. Kokubun, K. N. Erickson, T. A. Fritz, and R. L. McPherron. Local time asymmetry of Pc 4-5 pulsations and associated particle modulations at synchronous orbit. *J. Geophys. Res.*, 94(A6):6607–6625, 1989.
- [54] D.-H. Lee and K. Kim. Compressional MHD waves in the magnetosphere: A new approach. *J. Geophys. Res.*, 104(A6):12379–12385, 1999.
- [55] A. S. Leonovich and V. A. Mazur. Structure of magnetosonic eigenoscillations of an axisymmetric magnetosphere. *J. Geophys. Res.*, 105(A12):27707–27715, 2000.
- [56] W. Liu, J. B. Cao, X. Li, T. E. Sarris, Q.-G. Zong, M. Hartinger, K. Takahashi, H. Zhang, Q. Q. Shi, and V. Angelopoulos. Poloidal ULF wave observed in the plasmasphere boundary layer. *J. Geophys. Res. Space Physics*, 118(7):4298–4307, 2013.
- [57] W. Liu, T. E. Sarris, X. Li, S. R. Elkington, R. Ergun, V. Angelopoulos, J. Bonnell, and K. H. Glassmeier. Electric and magnetic field observations of Pc4 and Pc5 pulsations in the inner magnetosphere: A statistical study. *J. Geophys. Res.*, 114(A12), 2009.
- [58] W. Liu, T. E. Sarris, X. Li, R. Ergun, V. Angelopoulos, J. Bonnell, and K. H. Glassmeier. Solar wind influence on Pc4 and Pc5 ULF wave activity in the inner magnetosphere. *J. Geophys. Res.*, 115(A12), 2010.
- [59] W. Liu, T. E. Sarris, X. Li, Q.-G. Zong, R. Ergun, V. Angelopoulos, and K. H. Glassmeier. Spatial structure and temporal evolution of a dayside poloidal ULF wave event. *Geophys. Res. Lett.*, 38(19), 2011.
- [60] R. L. Lysak. Magnetosphere-ionosphere coupling by Alfvén waves at midlatitudes. *J. Geophys. Res.*, 109, 2004.

- [61] R. L. Lysak and D. hun Lee. Response of the dipole magnetosphere to pressure pulses. *Geophys. Res. Lett.*, 19(9):937–940, 1992.
- [62] R. L. Lysak and Y. Song. A three-dimensional model of the propagation of Alfvén waves through the auroral ionosphere: first results. *Adv. Space Res.*, 28:813–822, 2001.
- [63] R. L. Lysak, C. L. Waters, and M. D. Sciffer. Modeling of the ionospheric Alfvén resonator in dipolar geometry. *J. Geophys. Res. Space Physics*, 118, 2013.
- [64] P. N. Mager and D. Y. Klimushkin. Giant pulsations as modes of a transverse Alfvénic resonator on the plasmapause. *Earth, Planets and Space*, 65(5):397–409, 2013.
- [65] I. R. Mann, E. A. Lee, S. G. Claudepierre, J. F. Fennell, A. Degeling, I. J. Rae, D. N. Baker, G. D. Reeves, H. E. Spence, L. G. Ozeke, R. Rankin, D. K. Milling, A. Kale, R. H. W. Friedel, and F. Honary. Discovery of the action of a geophysical synchrotron in the Earth’s Van Allen radiation belts. *Nature Communications*, 4, 2013.
- [66] I. R. Mann and A. N. Wright. Finite lifetimes of ideal poloidal Alfvén waves. *J. Geophys. Res.*, 100:23677–23686, 1995.
- [67] I. R. Mann, A. N. Wright, and A. W. Hood. Multiple-timescales analysis of ideal poloidal Alfvén waves. *J. Geophys. Res.*, 102(A2):2381–2390, 1997.
- [68] T. Maynard, N. Smith, S. Gonzalez, et al. Solar storm risk to the North American electric grid. 2013.
- [69] K. McGuire, R. Goldston, M. Bell, M. Bitter, K. Bol, K. Brau, D. Buchenauer, T. Crowley, S. Davis, F. Dylla, H. Eubank, H. Fishman, R. Fonck, B. Grek, R. Grimm, R. Hawryluk, H. Hsuan, R. Hulse, R. Izzo, R. Kaita, S. Kaye, H. Kugel, D. Johnson, J. Manickam, D. Manos, D. Mansfield, E. Mazzucato, R. McCann, D. McCune, D. Monticello, R. Motley, D. Mueller, K. Oasa, M. Okabayashi, K. Owens, W. Park, M. Reusch, N. Sauthoff, G. Schmidt, S. Sesnic, J. Strachan, C. Surko, R. Slusher, H. Takahashi, F. Tenney, P. Thomas, H. Towner, J. Valley,

- and R. White. Study of high-beta magnetohydrodynamic modes and fast-ion losses in PDX. *Phys. Rev. Lett.*, 50(12):891–895, 1983.
- [70] R. L. McPherron. The role of substorms in the generation of magnetic storms. *Washington DC American Geophysical Union Geophysical Monograph Series*, 98:131–147, 1997.
- [71] R. L. McPherron, G. K. Parks, D. S. Colburn, and M. D. Montgomery. Satellite studies of magnetospheric substorms on august 15, 1968: 2. solar wind and outer magnetosphere. *J. Geophys. Res.*, 78(16):3054–3061, 1973.
- [72] T. Motoba, K. Takahashi, J. V. Rodriguez, and C. T. Russell. Giant pulsations on the afternoonside: Geostationary satellite and ground observations. *J. Geophys. Res. Space Physics*, 120:8350–8367, 2015.
- [73] NASA. Coordinated data analysis (workshop) web.
- [74] NASA. Near miss: The solar superstorm of july 2012.
- [75] M. Nicolet. The collision frequency of electrons in the ionosphere. *Journal of Atmospheric and Terrestrial Physics*, 3(4):200–211, 1953.
- [76] L. G. Ozeke and I. R. Mann. Energization of radiation belt electrons by ring current ion driven ULF waves. *J. Geophys. Res.*, 113(A2), 2008.
- [77] E. M. Poulter, W. Allan, E. Nielsen, and K.-H. Glassmeier. Stare radar observations of a PG pulsation. *J. Geophys. Res.*, 88(A7):5668, 1983.
- [78] J. A. Proehl, W. Lotko, I. Kouznetsov, and S. D. Geimer. Ultralow-frequency magnetohydrodynamics in boundary-constrained geomagnetic flux coordinates. *J. Geophys. Res.*, 107(A9):1225, 2002.
- [79] H. R. Radoski. A note on oscillating field lines. *J. Geophys. Res.*, 72(1), 1967.
- [80] H. R. Radoski. A theory of latitude dependent geomagnetic micropulsations: The asymptotic fields. *J. Geophys. Res.*, 79, 1974.

- [81] R. Rankin, J. C. Samson, and V. T. Tikhonchuk. Parallel electric fields in dispersive shear alfvén waves in the dipolar magnetosphere. *Geophys. Res. Lett.*, 26(24):3601–3604, 1999.
- [82] B. Rolf. Giant micropulsations at abisko. *J. Geophys. Res.*, 36(1):9, 1931.
- [83] G. Rostoker, H.-L. Lam, and J. V. Olson. PC 4 giant pulsations in the morning sector. *J. Geophys. Res.*, 84(A9):5153, 1979.
- [84] J. C. Samson, L. L. Cogger, and Q. Pao. Observations of field line resonances, auroral arcs, and auroral vortex structures. *J. Geophys. Res.*, 101(A8):17373–17383, 1996.
- [85] H. J. Singer, W. J. Hughes, and C. T. Russell. Standing hydromagnetic waves observed by ISEE 1 and 2: Radial extent and harmonic. *J. Geophys. Res.*, 87(A5):3519, 1982.
- [86] D. J. Southwood. Some features of field line resonances in the magnetosphere. *Planetary and Space Science*, 22(3):483–491, 1974.
- [87] D. J. Southwood. A general approach to low-frequency instability in the ring current plasma. *J. Geophys. Res.*, 81(19):3340–3348, 1976.
- [88] J. Stratton and N. J. Fox. Radiation belt storm probes (RBSP) mission overview. In *2012 IEEE Aerospace Conference*. Institute of Electrical & Electronics Engineers (IEEE), 2012.
- [89] E. Sucksdorff. Giant pulsations recorded at sodankyl during 19141938. *Terrestrial Magnetism and Atmospheric Electricity*, 44(2):157–170, 1939.
- [90] K. Takahashi, J. Bonnell, K.-H. Glassmeier, V. Angelopoulos, H. J. Singer, P. J. Chi, R. E. Denton, Y. Nishimura, D.-H. Lee, M. Nosé, and W. Liu. Multipoint observation of fast mode waves trapped in the dayside plasmasphere. *J. Geophys. Res.*, 115(A12), 2010.
- [91] K. Takahashi, K.-H. Glassmeier, V. Angelopoulos, J. Bonnell, Y. Nishimura, H. J. Singer, and C. T. Russell. Multisatellite observations of a giant pulsation event. *J. Geophys. Res.*, 116:A11223, 2011.

- [92] K. Takahashi, M. D. Hartinger, V. Angelopoulos, K.-H. Glassmeier, and H. J. Singer. Multispacecraft observations of fundamental poloidal waves without ground magnetic signatures. *J. Geophys. Res. Space Physics*, 118:4319–4334, 2013.
- [93] K. Takahashi, R. W. McEntire, A. T. Y. Lui, and T. A. Potemra. Ion flux oscillations associated with a radially polarized transverse Pc 5 magnetic pulsation. *J. Geophys. Res.*, 95(A4):3717, 1990.
- [94] K. Takahashi, N. Sato, J. Warnecke, H. Lühr, H. E. Spence, and Y. Tonegawa. On the standing wave mode of giant pulsations. *J. Geophys. Res. Space Physics*, 97(A7):10717–10732, 1992.
- [95] B. J. Thompson and R. L. Lysak. Electron acceleration by inertial alfvén waves. *J. Geophys. Res.*, 101(A3):5359–5369, 1996.
- [96] S. M. Thompson and M. G. Kivelson. New evidence for the origin of giant pulsations. *J. Geophys. Res.*, 106(A10):21237–21253, 2001.
- [97] V. T. Tikhonchuk and R. Rankin. Electron kinetic effects in standing shear alfvén waves in the dipolar magnetosphere. *Physics of Plasmas*, 7(6):2630, 2000.
- [98] B. T. Tsurutani, W. D. Gonzalez, G. S. Lakhina, and S. Alex. The extreme magnetic storm of 12 september 1859. *Journal of Geophysical Research: Space Physics*, 108(A7), 2003. 1268.
- [99] A. Y. Ukhorskiy. Impact of toroidal ULF waves on the outer radiation belt electrons. *J. Geophys. Res.*, 110(A10), 2005.
- [100] J. Veldkamp. A giant geomagnetic pulsation. *Journal of Atmospheric and Terrestrial Physics*, 17(4):320–324, 1960.
- [101] J. A. Wanliss and K. M. Showalter. High-resolution global storm index: Dst versus sym-h. *Journal of Geophysical Research: Space Physics*, 111(A2):n/a–n/a, 2006. A02202.
- [102] C. L. Waters, R. L. Lysak, and M. D. Sciffer. On the coupling of fast and shear Alfvén wave modes by the ionospheric Hall conductance. *Earth Planets Space*, 65:385–396, 2013.

- [103] C. L. Waters and M. D. Sciffer. Field line resonant frequencies and ionospheric conductance: Results from a 2-d MHD model. *J. Geophys. Res.*, 113(A5), 2008.
- [104] D. M. Wright and T. K. Yeoman. High-latitude HF doppler observations of ULF waves: 2. waves with small spatial scale sizes. *Ann. Geophys.*, 17(7):868–876, 1999.
- [105] J. R. Wygant, A. Keiling, C. A. Cattell, R. L. Lysak, M. Temerin, F. S. Mozer, C. A. Kletzing, J. D. Scudder, V. Streitsov, W. Lotko, and C. T. Russell. Evidence for kinetic alfvn waves and parallel electron energization at 46 re altitudes in the plasma sheet boundary layer. *Journal of Geophysical Research: Space Physics*, 107(A8):SMP 24–1–SMP 24–15, 2002.
- [106] B. Yang, Q.-G. Zong, Y. F. Wang, S. Y. Fu, P. Song, H. S. Fu, A. Korth, T. Tian, and H. Reme. Cluster observations of simultaneous resonant interactions of ULF waves with energetic electrons and thermal ion species in the inner magnetosphere. *J. Geophys. Res.*, 115(A2), 2010.
- [107] K. Yee. Numerical solution of initial boundary value problems involving maxwell's equations in isotropic media. *IEEE Trans. Antennas Propagat.*, 14(3), 1966.
- [108] T. K. Yeoman and D. M. Wright. ULF waves with drift resonance and drift-bounce resonance energy sources as observed in artificially-induced HF radar backscatter. *Ann. Geophys.*, 19(2):159–170, 2001.
- [109] Q.-G. Zong, X.-Z. Zhou, X. Li, P. Song, S. Y. Fu, D. N. Baker, Z. Y. Pu, T. A. Fritz, P. Daly, A. Balogh, and H. Réme. Ultralow frequency modulation of energetic particles in the dayside magnetosphere. *Geophys. Res. Lett.*, 34(12), 2007.
- [110] Q.-G. Zong, X.-Z. Zhou, Y. F. Wang, X. Li, P. Song, D. N. Baker, T. A. Fritz, P. W. Daly, M. Dunlop, and A. Pedersen. Energetic electron response to ULF waves induced by interplanetary shocks in the outer radiation belt. *J. Geophys. Res.*, 114(A10), 2009.